COUPLING A LAND-SURFACE MODEL TO LARGE-EDDY SIMULATION TO STUDY THE NOCTURNAL BOUNDARY LAYER

by

Nick Shingleton

A thesis submitted to the faculty of
The University of Utah
in partial fulfillment of the requirements for the degree of

Master of Science

Department of Mechanical Engineering

The University of Utah

May 2010

Copyright © Nick Shingleton 2010

All Rights Reserved

THE UNIVERSITY OF UTAH GRADUATE SCHOOL

SUPERVISORY COMMITTEE APPROVAL

of a thesis submitted by

Nick Shingleton

This thesis has been read by each member of the following supervisory committee and by majority vote has been found to be satisfactory.

	Chair: Rob Stoll
	Eric Pardyjak
	Meredith Metzger

THE UNIVERSITY OF UTAH GRADUATE SCHOOL

FINAL READING APPROVAL

To the Graduate Council of the University of Utah:

I have read the thesis of Nick Shingleton in its final form and have found that (1) its format, citations, and bibliographic style are consistent and acceptable; (2) its illustrative materials including figures, tables, and charts are in place; and (3) the final manuscript is satisfactory to the Supervisory Committee and is ready for submission to The Graduate School.

Date

Rob Stoll
Chair, Supervisory Committee

Approved for the Major Department

Tim Ameel
Chair/Dean

Approved for the Graduate Council

Charles Wight
Dean of The Graduate School

ABSTRACT

Negatively buoyant forces in the stable boundary layer (SBL) damp turbulent motions, resulting in decreased transport of momentum, heat and water vapor. During high levels of stratification this can cause intermittent turbulence, gravity waves and weak turbulent fluxes. In some cases, decoupling between the atmospheric boundary layer (ABL) and land-atmosphere fluxes can occur. Accurately reproducing these phenomena requires detailed treatment of the physical processes that govern the two-way dynamic interaction between surface properties and the ABL. Increasingly, large-eddy simulation (LES) is used to study land-atmosphere interactions in the SBL. In these studies, the dominant treatment of surface boundary conditions is to specify a known state or flux. This research uses LES that is fully coupled to a land-surface model (LSM) to investigate the SBL. The LSM explicitly solves for the transport of heat and water in a one-dimensional column of the upper soil. Coupling to the atmosphere is achieved through a surface budget, which partitions the available radiative forcing into ground heat flux and sensible and latent heat fluxes. Turbulent boundary layer profiles and surface fluxes are compared to field data and results from simulations of the GABLS3 LES intercomparison case.

For my wife, Naomi, and my parents.

CONTENTS

LIST OF FIGURES

LIST OF TABLES

ACKNOWLEDGEMENTS

Foremost, I would like to thank my research advisor Rob Stoll for his guidance and support thoughout the process of research and thesis writing. His enthusiasm, knowledge and accessibility helped make for a smooth research progression. I would also like to thank Eric Pardyjak for introducing me to environmental fluid dynamics and for his council and encouragement.

I thank the GEWEX and GABLS3 scientists (especially Sukanta Basu, Bert Holtslag and Fred Bosveld) for collecting and processing the data for the Cabauw meteorological site and specifically GABLS3, without which this research would not have been possible.

Lastly, thanks to the University of Utah High Performance Computing Center (CHPC) for the computational time allocated to the project. Without it I could not have completed the numerical simulations.

CHAPTER 1

INTRODUCTION

Studying the atmospheric boundary layer (ABL) is important for the basic fact that each of us spends a majority of our lifetime within it. Influence of the ABL is most evident through the local temperature, humidity, and other weather phenomena. The hydrological cycle of moisture transport occurs within the ABL, effecting crop growth and food supply. Furthermore, pollutant transport is increasingly important for quality of life, with the expansion of population, urbanization and energy consumption. The driving mechanism behind these, and many other ABL phenomena, are the interactions between the land surface and the atmosphere.

Various methods are used to study the atmosphere, including theoretical, experimental and computational. Numerical simulations of the atmosphere are commonly used for predictive purposes of weather and global climate change, which are strongly effected by the transport of momentum, heat and mass within the ABL. The accuracy of models used for weather and global climate change need improvement due to the highly parameterized solution methods for turbulence and other ABL physics. Large-eddy simulation (LES) provides a solution method that more accurately represents turbulent flow. For this reason, LES can be used to examine the validity of specific parameterizations and provide insight to possible improvements.

LES is a useful tool for research purposes, however for it to become a reliable method for general engineering and environmental science it requires improvements in the sub-grid scale (SGS) model, chemical interactions and other complex phenomena. In LES, prevalent treatment of the surface boundary condition (BC) is to specify the flux or the state (i.e. temperature and moisture). This oversimplifies

the physics of the evolving surface fluxes, which respond to the changing radiation, atmosphere and soil state. This research has implemented a land-surface model (LSM) within LES to capture the evolving surface physics and the effect on the atmosphere. This is the first such study of a stable boundary layer (SBL) using LES coupled to a LSM. The coupled LSM-LES was applied to the third Global Energy and Water Cycle Experiment (GEWEX) ABL study (GABLS3) intercomparison LES case to simulate the SBL. Resulting surface fluxes and average profiles are compared to tower measurements and simulations using the original GABLS3 LES BCs based on 0.25 m air temperature and specific humidity.

1.1 Background

Features of the ABL, for example the spatial distribution of temperature, humidity and turbulence intensity, are highly dependent upon land-atmosphere interactions. Temporal changes in the ABL are forced by surface fluxes of momentum, heat and moisture [90]. LES is a useful tool for studying these land-atmosphere interactions and the resulting ABL structure. However, previous LES studies of the ABL have largely simplified the surface BC and little focus has been devoted to realistic diurnal variation of the ABL. The most common method of dealing with the surface has been to specify the surface state or flux at the boundary [2, 81, 82, 12, 49, 87, 89, 88, 10, 9, 11, 7, 79]. Prescribing the surface state only provides one-way land-atmosphere interaction, while specifying the flux completely decouples the surface forcing from the atmosphere [71]. Implementing these BCs results in an idealized flow. Furthermore, without detailed measurements, specifying the surface state or flux does not capture the proper temporal evolution nor the energy partition between sensible and latent heat flux. Most LES studies put little emphasis on improving BCs, but focus on validation and improvement of the subgrid scale (SGS) model. This is usually done because simplified surface BCs ease analysis and comparison of LES results.

The simplest BCs are applied in LES of strictly neutral flows where temperature and buoyancy effects are neglected. In this case, the surface treatment is only relevant for momentum drag. Quasi-steady neutral ABL simulations are useful

for testing and comparison of different SGS modeling schemes or for general turbulence studies [42, 75, 66, 57, 22, 87, 86]. Information about ABL transport of heat and mass is not provided. In LES cases that do include temperature and buoyancy effects, the most prevalent BC treatment is to prescribe the surface state [12, 10, 9, 11, 81, 82, 89, 88, 51]. For stably stratified flow this is usually achieved by defining a constant surface cooling rate so that the prescribed surface temperature changes linearly [12, 10, 9, 88, 51]. Studies of this type attempt to reach a quasi-steady state, characterized by a temperature profile changing at a constant rate throughout the ABL, while all other mean and turbulence properties are constant [51]. Businger and Arya [26] proposed that this could only occur at high latitudes, due to the short period of inertial oscillation. The first LES intercomparison GABLS [12], loosely based on BASE (Beaufort Sea Arctic Stratus Experiment) observations, was of this type. The simulation was initialized as a mixed layer with a prescribed surface cooling rate of 0.25 K/hr applied for 9 hours. This moderately stable case ($\delta/L \approx 2$) compared 11 LES models for a range of resolutions. Comparisons showed that a grid length of 6.25 m achieved reasonably accurate results relative to high resolution simulations and a grid length of 3.125 m or less is ideal for a moderately stable regime. The high resolution results agreed well with local scaling theory of Nieuwstadt and indicated that the spread between models was mainly due to differences in surface fluxes [69]. Stoll and Porté-Agel [88] simulated the same GABLS case, independent of the intercomparison, using the scale-dependent Lagrangian dynamic SGS model and comparing to the plane averaged and locally averaged model. The Lagrangian averaged model compared to theory and reproduced important ABL features, such as a low-level jet and positive potential temperature curvature, better than the other averaging schemes.

More realistic LES BCs that evolve in time corresponding to the diurnal cycle have only recently been attempted [11, 24, 36, 44]. Basu et al. [11] achieved temporal evolution by specifying the scalar state at a level between the surface and first LES node based on screen level measurements at 1.2 m. This is a similar BC approach used in the current GABLS3 LES case. The simulation was based on observations from the Wangara study in Australia and captured a full 24 hour

diurnal cycle [33]. This study applied the locally averaged scale-dependent dynamic SGS model and was able to accurately reproduce evolution of velocity, temperature, and turbulent kinetic energy profiles and surface fluxes. The simulations developed a nocturnal low-level jet that compared well with observations. Only a few LES studies have captured the diurnal evolution during a stable time period [53, 11] using a prescribed state or flux from measurements, others have focused on simpler convective periods [24, 36, 44].

A small number of studies have coupled a LSM to LES for the surface BC, both of which have been applied to convective periods [71, 44]. Patton et al. [71] simulated free convection with the only external forcing through a constant incoming radiation of 700 W/m^2. This LSM-LES case did not model the diurnal cycle, but ran until the turbulence reached a quasi-steady state. The soil initialization was based on measurements from the Southern Great Plains 1997 experiment [46]. Multiple simulations were performed with different length patches of abrupt changes in soil moisture content. Results showed that ABL structure was strongly dependent upon heterogeneity and patch scale. At certain scales of surface heterogeneity the total turbulent kinetic energy was increased by about 20% compared to homogeneous simulations. Huang et al. [44] implemented a coupled LSM-LES model that evolved in time and captured a daytime diurnal cycle from 0600-1800 hours local time on July 1st. The simulation, based on observations from the soil moisture-atmosphere coupling experiment (SMACEX) [54], compared well to measurements for the convective period.

Although the application of a LSM to LES is rare, it is common practice to couple a LSM to the atmosphere in mesoscale and general circulation models [35, 84, 23, 58, 59, 60, 63, 62, 47, 5, 70, 64]. These LSMs have mostly been used for research purposes due to the initial conditions needed for the model and the increased computational expense [84]. McCumber and Pielke [62, 63] coupled a bare soil iterative LSM with a simple mesoscale model and tested the sensitivity of different initializations. The LSM enforced a surface energy budget linked to a 1-dimensional soil heat and moisture transport model. Results showed that heat fluxes at the surface were much more sensitive to the soil moisture content

initialization than to albedo or soil type. Additionally, the surface heat fluxes are more than an order of magnitude more sensitive to the initial soil moisture profile than to the soil temperature profile.

More complex surface models have been developed that parameterize evapotranspiration [84, 35, 41, 5, 37, 80, 28]. Smirnova et al. [84] tested multiple types of soil models comparing a force restore, a multi-level implicit bare soil model, and a soil-vegetation model. Simulations were compared to data from a dry case, based on data from the Great Plains Turbulence Field Program conducted in O'Neill, Nebraska [55]; and a moist case initialized from observations of the First International Field Experiment (FIFE) of Manhattan, Kansas [15]. It was found that both of the more sophisticated models performed better than the force restore model in each case. The soil-vegetation model only offered slightly improved results over the bare soil model in the moist case. However, the evapotranspiration parameterization was very important when the soil moisture was close to the wilting point, performing much better than both bare soil models.

1.2 Fundamentals of Large-Eddy Simulation

Numerical solutions of turbulent flow is categorized into three general methodologies: direct numerical simulation (DNS), LES and Reynolds-averaged Navier-Stokes (RANS). RANS only provides an ensemble average solution and models all unsteady effects, with a benefit of relatively low computational expense [74]. On the other side of the spectrum, DNS solves for all relevant scales of turbulent motion with no model component. Within the ABL, turbulence is generated at scales on the order of the BL height ($\sim$100 m - 3 km). Turbulent energy then cascades down to smaller scales until it is dissipated into heat by viscosity, at scales on the order of 1 mm [74]. This implies that in order to resolve all the scales of motion in DNS of the ABL, between 10^{15} to 10^{21} grid points are required [94]. In the past 30 years, grid resolutions for numerical simulations of the ABL have very closely followed Moore's law, which states that computing power doubles every 18 months [67]. Voller and Porté-Agel [94] have shown that if this law continues to hold, DNS of the ABL will not be possible until approximately years 2040-2070 for 3-dimensional

domains of 100^3 m - 10^3 km.

LES provides a compromise between the accuracy of DNS and numerical efficiency of RANS, by resolving only the largest scales of fluid motion. The smallest turbulent scales, assumed to be universal, are modeled. The remainder of this chapter will focus on LES and describe the solution methods applicable to the current research.

1.2.1 Governing Equations

The complete governing equations of conservation of mass, momentum and scalar concentration (heat, humidity, etc), specific to the ABL, are shown in equations 1.1-1.3.

$$\frac{\partial u_j}{\partial x_j} = 0 \tag{1.1}$$

$$\frac{\partial u_i}{\partial t} + u_j \frac{\partial u_i}{\partial x_j} = -\frac{1}{\rho}\frac{\partial p}{\partial x_i} + \nu \frac{\partial^2 u_i}{\partial x_j^2} - \delta_{i3} g - \epsilon_{ij3} f_c u_j \tag{1.2}$$

$$\frac{\partial C}{\partial t} + u_j \frac{\partial C}{\partial x_j} = \nu_C \frac{\partial^2 C}{\partial x_j^2} \tag{1.3}$$

Where $f_c = 2\omega \sin\phi$ is the Coriolis parameter, at a latitude of ϕ and with an angular velocity of the earth $\omega = 2\pi/24h = 7.27{\times}10^{-5}\ s^{-1}$. Additionally, g is gravity, ν is the dynamic viscosity and C is a scalar. The equations are written in Cartesian tensor form and assume the use of a tangential coordinate system with u, v and w aligned with east, north and the vertical, respectively.

In LES, a few assumptions are applied to the momentum equation to ease numerical implementation. Buoyancy effects in the momentum equation are accounted for with the Boussinesq approximation so that vertical density perturbations are treated as potential temperature perturbations about hydrostatic equilibrium [90].

$$\frac{\partial \overline{p}}{\partial z} = -\overline{\rho} g \tag{1.4}$$

$$\frac{\rho'}{\overline{\rho}} = -\frac{\theta_v'}{\overline{\theta_v}} \tag{1.5}$$

Where for any variable (A), a prime (A') represents the fluctuation about the mean ($\overline{A}$), represented by the overbar. Horizontal pressure gradients are substituted with the definition of the geostrophic wind by

$$\frac{1}{\rho}\frac{\partial p}{\partial x} = f_c V_g \text{ and} \tag{1.6}$$

$$-\frac{1}{\rho}\frac{\partial p}{\partial y} = f_c U_g \tag{1.7}$$

After substitution (for more details see Stull [90] pp. 75-86), the momentum equation becomes

$$\frac{\partial u_i}{\partial t} + u_j\frac{\partial u_i}{\partial x_j} = \nu\frac{\partial^2 u_i}{\partial x_j^2} - \delta_{i3}g\frac{\theta_v'}{\overline{\theta_v}} - \frac{1}{\overline{\rho}}\frac{\partial p'}{\partial x_i} - \epsilon_{ij3}f_c\left(U_{g_j} - u_j\right), \tag{1.8}$$

where $U_{g_j} = (U_g, V_g, 0)$.

The idea behind LES is that the smallest scales of motion are universal and can be modeled. Only large scales of motion that are dependent on BCs must be explicitly resolved. In practice this is done by filtering the governing equations of fluid flow with a low pass filter. A general filter can be applied to a given variable so that the instantaneous value can be represented by the sum of the filtered ($\tilde{u}_i$) component and sub-filter (u_i'') component as [78]

$$u_i = \tilde{u}_i + u_i''. \tag{1.9}$$

Spatial low pass filtering is applied at a characteristic length $\Delta_f \geq \Delta_g$, where Δ_g is the numerical grid spacing.

The filter operation is applied to each variable of the governing equations 1.1, 1.3 and 1.8. After rearranging terms and applying filtering rules, the filtered governing equations solved in LES for mass, momentum and scalars become

$$\frac{\partial \tilde{u}_j}{\partial x_j} = 0 \tag{1.10}$$

$$\frac{\partial \tilde{u}_i}{\partial t} + \frac{\partial \tilde{u}_i \tilde{u}_j}{\partial x_j} = -\delta_{i3} g \frac{\tilde{\theta}'_v}{\tilde{\overline{\theta}}_v} - \frac{\partial \tilde{p}'}{\partial x_i} - \epsilon_{ij3} f_c \left(U_{g_j} - \tilde{u}_j \right) - \frac{\partial \tau_{ij}}{\partial x_j} \tag{1.11}$$

$$\frac{\partial \tilde{C}}{\partial t} + \tilde{u}_j \frac{\partial \tilde{C}}{\partial x_j} = -\frac{\partial q_{C,i}}{\partial x_i}. \tag{1.12}$$

The sub-grid scale (SGS) stress τ_{ij}, given by 1.13, accounts for the effects of the unresolved motions on the flow.

$$\tau_{ij} = \widetilde{u_i u_j} - \tilde{u}_i \tilde{u}_j \tag{1.13}$$

Similarly, in the conservation of scalar concentration equation $q_{C,i} = \widetilde{u_i C_j} - \tilde{u}_i \tilde{C}_j$ is the SGS flux. In 1.11 and 1.12, viscous dissipation and molecular diffusion have been neglected due to the high Reynolds number of the ABL [90]. The SGS stress and flux are unknown and must be modeled with a SGS model.

1.2.2 Subgrid Scale Model

The current research applies the scale-dependent Lagrangian dynamic model [86]. The SGS terms must be formulated based on the resolved components of the flow. Many SGS models parameterize the deviatoric portion of the stress using an eddy viscosity model and the SGS flux using an eddy diffusivity model as

$$\tau_{ij} - \frac{1}{3}\delta_{ij}\tau_{kk} = -2\nu_T \tilde{S}_{ij} \quad \text{and} \tag{1.14}$$

$$q_{C,i} = -D_T \frac{\partial \tilde{C}}{\partial x_i}. \tag{1.15}$$

Where $\tilde{S}_{ij} = 1/2(\partial \tilde{u}_i/\partial x_j + \partial \tilde{u}_j/\partial x_i)$ is the resolved strain rate tensor, ν_T is the eddy viscosity and D_T is the eddy diffusivity. If C is temperature (θ) $D_T = \nu_T Pr_{sgs}^{-1}$, where Pr_{sgs} is the SGS Prandtl number [88], otherwise an analogous representation is used replacing the SGS Prandtl number with the SGS Schmidt number.

A common method of modeling the eddy viscosity is the Smagorinsky mixing length approximation [83]. The Smagorinsky model specifies the viscosity as

$\nu_T = (\Delta_f C_S)^2 |\tilde{S}|$, which results in a SGS stress and flux of

$$\tau_{ij} - \frac{1}{3}\delta_{ij}\tau_{kk} = -2(\Delta_f C_S)^2 |\tilde{S}|\tilde{S}_{ij} \quad \text{and} \tag{1.16}$$

$$q_{C,i} = -\Delta_f^2 C_S^2 Pr_{sgs}^{-1} |\tilde{S}| \frac{\partial \tilde{C}}{\partial x_i}. \tag{1.17}$$

C_S is the Smagorinsky coefficient and $|\tilde{S}| = (2\tilde{S}_{ij}\tilde{S}_{ij})^{1/2}$ is the magnitude of the resolved strain rate tensor.

The SGS Prandtl number and Smagorinsky coefficient must be specified in order to close the equations. The original Smagorinsky SGS model parameterized these coefficients as constant values based on idealized assumptions of isotropic turbulence [56]. In the ABL, anisotropic regions are common and constant parameterizations provide poor results [88]. Current methods dynamically compute model coefficients based on the resolved flow field.

The scale-dependent Lagrangian dynamic SGS model used in this research has been validated in various studies of quasi-steady neutral flow and stable flow [87, 86, 88]. Specifically, Stoll and Porté-Agel [86] simulated a neutral homogeneous ABL with uniform aerodynamic surface roughness and constant uniform flux of a passive scalar. The model produced mean profiles of velocity and scalar concentration that agree with similarity theory within the surface layer. Normalized velocity spectra plotted against normalized wavenumber displayed the expected scaling and collapse within the production and inertial subrange. The normalized scalar concentration spectra also shows an inertial subrange.

CHAPTER 2

LAND-SURFACE MODEL AND NUMERICAL METHODS

The dynamics of the ABL are largely driven by interactions with the surface and the resulting fluxes of momentum, heat and moisture. In LES, the link between the land and the overlying atmosphere is established through the surface BC. The most common treatment of the surface BC in LES is to specify the state (i.e. temperature, moisture) or the flux either as a constant or as a function of time. In computing sensible and latent heat fluxes, the two are treated as being completely independent from one another. In reality, the temperature and moisture of the surface evolves in time and the fluxes are dependent upon one another and the available radiative forcing. Recently, LES surface BCs based on LSMs have been proposed [71, 44]. These BCs attempt to predict the diurnal evolution of surface state variables in a more physically realistic manner. This type of BC is common in mesoscale models, however it has not seen widespread use in LES and has yet to be deployed in studies of the SBL. This section describes the LSM that has been implemented within LES to capture a more physically realistic diurnal evolution of the surface properties and land-atmosphere fluxes. The model uses a surface energy budget and mass budget linked to a one-dimensional vertical soil model applied at each horizontal LES grid point.

2.1 The Surface Budgets

In general, the surface of the earth is heterogeneous and 3-dimensional. Horizontal gradients exist that result in horizontal fluxes and complex phenomena. In this model, the problem is simplified by treating the surface ideally. The land surface is assumed to be relatively smooth, horizontal, and have homogeneous properties

within each grid cell. This simplification allows for only vertical land-atmosphere fluxes to be considered [4], which is a good assumption for LES where horizontal grid sizes are on the order of 10 m.

Conservation of energy is applied at the infinitely thin interface between the atmosphere and the ground. The resulting energy balance (equation 2.1) is driven by the net radiation flux (R_N), causing the soil heat flux (Q_G), sensible heat flux (Q_S), and latent heat flux (Q_L) to respond to the available energy at any given time and at each individual surface grid point.

$$R_N + Q_G + Q_S + Q_L = 0 \tag{2.1}$$

Conservation of mass (equation 2.2) is also applied at the surface, resulting in a balance between precipitation (P), soil moisture flux (W_G), and evaporation (E).

$$P = W_G + E \tag{2.2}$$

Precipitation is not included in the current simulations and can therefore be neglected in the surface mass budget resulting in a balance between soil moisture flux and evaporation. The energy balance and mass balance are tied together by the assumption that all of the moisture evaporated requires the same amount of energy to be transformed into a gas, in other words, the latent heat is proportional to evaporation through the latent heat of vaporization, λ_e,

$$Q_L = \lambda_e E.$$

Knowledge of the exact physics and small scale transport is unavailable between the surface and first LES level. As a result, a specific sub-grid scale model is required that relates the surface flux to the surface state and resolved velocity and scalar field at the first LES level. In numerical atmospheric models, including LES, it is common to use the log-linear law from Monin-Obukhov similarity theory to parameterize this flux [75, 14]. Monin-Obukhov theory is valid in the surface layer (approximately the bottom 10% of the ABL) where the fluxes are assumed to be constant. The resulting turbulent scalar fluxes, in kinematic units, are given by equations 2.3 and 2.4, respectively for temperature and moisture. The friction

velocity, u_{*s}, is related to the shear stress at the surface and also computed by the log-linear law as shown in equation 2.5.

$$q_{\theta,s} = u_{*s}\theta_* = \frac{\kappa u_{*s}(\tilde{\theta} - \theta_s)}{ln(\frac{z}{z_t}) + \Psi_H(\frac{z}{L}) - \Psi_H(\frac{z_t}{L})} \tag{2.3}$$

$$q_{q,s} = u_{*s}q_* = \frac{\kappa u_{*s}(\tilde{q} - q_s)}{ln(\frac{z}{z_t}) + \Psi_H(\frac{z}{L}) - \Psi_H(\frac{z_t}{L})} \tag{2.4}$$

$$\sqrt{\tau_s} = u_{*s} = \frac{\kappa \tilde{U}}{ln(\frac{z}{z_o}) + \Psi_M(\frac{z}{L}) - \Psi_M(\frac{z_o}{L})} \tag{2.5}$$

In 2.3-2.5, $\kappa = 0.4$ is the von Karman constant, θ_* and q_* are temperature and moisture scales defined by the respective turbulent flux divided by the friction velocity. Additionally, z is the height of the first LES level where the atmosphere has a filtered wind speed, $\tilde{U} = \sqrt{\tilde{u}^2 + \tilde{v}^2}$, temperature, $\tilde{\theta}$, and moisture content, $\tilde{q}$. By definition, z_o is the height that the velocity profile crosses zero, and similarly z_t is the height that the temperature (moisture) profile reaches the surface temperature, θ_s (moisture, q_s). Both z_o and z_t are determined empirically by extrapolated atmospheric measurements. There is no reason to expect the heat roughness to take the same value as the momentum roughness, since the physical mechanism of transfer is not the same, however moisture and heat are assumed to be equal [38, 14, 25]. The surface roughness, z_o, represents the momentum drag by elements obstructing the flow of wind. The heat roughness, z_t, represents the height above the surface where turbulent mixing begins to dominate diffusive scalar transport. Based on measurements, generally z_t is orders of magnitude smaller than z_o. From the perspective of LES, the sensible heat flux ($q_{\theta,s}$) and evaporation ($q_{q,s}$) close the filtered governing equation of conservation of scalar concentration for heat and moisture (equation 1.12) at the surface. Similarly, τ, provides the SGS stress (equation 1.13) at the surface and closes the LES momentum equation (1.11).

The general form of the log-linear law (equations 2.3-2.5) is derived from similarity theory and is modified with the empirical stability correction terms (Ψ_M and Ψ_H) formulated as a function of the Monin-Obukhov length, L. The Monin-Obukhov length is a scaling parameter, commonly related to the degree of atmo-

spheric stability and is defined as [4]

$$L = -\frac{\overline{\theta_v} u_{*s}^3}{\kappa g (\overline{w'\theta'_v})_s}. \tag{2.6}$$

Where $(\overline{w'\theta'_v})_s$ is the average sensible heat flux obtained from equation 2.3. The log-linear law is derived and the stability corrections are formulated based on average values over a homogeneous surface [38], however in LES applications the log law is applied locally and instantaneously at each horizontal node [1, 61, 88]. The use of the log law in this manner is questionable and applied for lack of a better method. The stability corrections take a different form under stable and unstable conditions and are formulated as

$$\Psi_M = \begin{cases} 2\ln\left[\frac{(1+x)}{2}\right] + \ln\left[\frac{(1+x^2)}{2}\right] - 2\tan^{-1} x + \frac{\pi}{2} & z/L < 0 \\ -\beta_1 \frac{z}{L} & z/L > 0 \\ 0 & z/L = 0. \end{cases} \tag{2.7}$$

$$\Psi_H = \begin{cases} 2\ln\left[\frac{1+y}{2}\right] & z/L < 0 \\ -\beta_1 \frac{z}{L} & z/L > 0 \\ 0 & z/L = 0. \end{cases} \tag{2.8}$$

Where $x = (1 - \gamma_1 \frac{z}{L})^{1/4}$ and $y = (1 - \gamma_2 \frac{z}{L})^{1/2}$ and $\gamma_1 \approx \gamma_2 \approx 16$ and $\beta_1 \approx 5$ are empirical constants [38].

The vertical scalar fluxes from the surface (2.3-2.4) are converted to the proper dynamic units ($\frac{W}{m^2}$) of equation 2.1 by the scaling of equations 2.9 and 2.10, respectively for temperature and moisture [38].

$$Q_S = \rho_{air} c_p u_{*s} \theta_* \tag{2.9}$$

$$Q_L = \rho_{air} \lambda_e u_{*s} q_* \tag{2.10}$$

2.2 Radiation

The net radiation can be decomposed by source, into four components. During the day, the main contribution is the incoming solar short wave radiation ($R_{S\downarrow}$), a

portion of which is reflected from the surface ($R_{S\uparrow}$).

$$R_N = R_{S\downarrow} + R_{S\uparrow} + R_{L\downarrow} + R_{L\uparrow} \tag{2.11}$$

Long wave radiation emitted by the atmosphere ($R_{L\downarrow}$) and surface ($R_{L\uparrow}$) contribute a small portion of the total daytime radiation, conversely at nighttime they are the only radiation component.

The solar radiation is modeled using the method presented by Stull [90] and summarized here based on the geometrical relationship between a point on the earth and the relative location of the sun. The elevation angle (Φ) of the sun with respect to a flat surface is given as a function of the latitude (ϕ), longitude (λ_L), time (t_{UTC}) in Coordinated Universal Time (UTC) hours and solar declination angle (δ_s) as

$$\sin\Phi = \sin\phi\sin\delta_s - \cos\phi\cos\delta_s\cos\left[\frac{\pi\cdot t_{UTC}}{12} - \lambda_L\right]. \tag{2.12}$$

The solar declination angle (2.13) is the angle of the sun above the equatorial plane computed by the day of the year (d), the Tropic of Cancer latitude (0.409 radians), the day of the summer solstice (173), and the average number of days per year (365.25).

$$\delta_s = 0.409\cos\left[\frac{2\pi\cdot(d-173)}{365.25}\right] \tag{2.13}$$

This study focuses on clear sky conditions, as a result, the portion of solar radiation that reaches the surface is given by the transmissivity of the atmosphere as

$$T_r = 0.6 + 0.2\sin\Phi. \tag{2.14}$$

The solar irradiance (S) at the top of the atmosphere is treated as a constant

of -1370 $\frac{W}{m^2}$. The radiation is attenuated by the atmosphere through scattering, absorption and reflection. The effective thickness of the atmosphere being penetrated and the resulting attenuation increase with decreasing elevation angle (Φ). The steradians subtended by the sun that are intersected by the earths surface also decrease with the elevation angle, so that the solar irradiance at the surface is approximated by

$$R_{S\downarrow} = \begin{cases} S \cdot T_r \cdot \sin\Phi & \sin\Phi \geq 0 \\ 0 & \sin\Phi < 0. \end{cases} \tag{2.15}$$

A portion of the solar radiation is reflected from the surface. The surface bulk reflectivity is parameterized by the albedo (α), so that the shortwave radiation away from the surface is given by $R_{S\uparrow} = -\alpha R_{S\downarrow}$. The albedo depends on the surface cover, wetness, and elevation angle of the sun and is generally determined by measurements. When only surface cover is known, the total albedo can be parameterized as a function of soil wetness (α_m) and solar elevation angle (α_s) by [45]

$$\alpha = \alpha_m + \alpha_s. \tag{2.16}$$

Albedo dependence on wetness decreases with increasing moisture as

$$\alpha_m = \begin{cases} \alpha_1(1-\Delta) & \Delta \leq 0.5 \\ \alpha_2 & \Delta > 0.5, \end{cases} \tag{2.17}$$

where α_1 and α_2 are albedo limits from measurements and $\Delta = \frac{\eta}{\eta_{sat}}$. Where η is the soil volumetric moisture content and η_{sat} is the soil porosity. Albedo increases with decreasing solar elevation angle as

$$\alpha_s = 0.01\left[\exp\left(c\left(\frac{\pi}{2} - \Phi\right)^{1.5}\right) - 1\right] \tag{2.18}$$

where c=0.003286 [45].

The longwave radiation emitted from the surface is parameterized using the Stefan-Boltzmann law as

$$R_{L\uparrow} = \epsilon \sigma_{SB} T_s^4. \tag{2.19}$$

Where $\sigma_{SB} = 5.67 \times 10^{-8} \frac{W}{m^2 K^4}$ is the Stefan-Boltzmann constant. The infrared emissivity, ϵ, depends on surface type and generally ranges between 0.9-0.99. Table A.1 in the Appendix contains representative values of shortwave albedo and longwave emissivity for a range of surface types.

The longwave radiation emitted by the atmosphere, $R_{L\downarrow}$, is the most physically complex term of the net radiation flux (2.11) at the surface. Each fluid parcel within the atmosphere emits a spectrum of radiation based on the fluid composition (i.e. dry air, water vapor, carbon dioxide, etc.). The radiation emitted by a parcel is continuously attenuated by each parcel in the path through absorption, which also depends on the parcel composition. The complexity is increased further by the associated radiative cooling and heating that occurs through radiation emission and absorption, respectively. In atmospheric models, each discrete grid can be treated as a fluid parcel with the average composition and temperature determined by the solution at each time. The complex 3-dimensional radiative interactions between fluid parcels can be simplified by averaging composition and temperature horizontally and only solving the vertical flux divergence equations [31, 65].

There are various approaches of modeling the atmospheric longwave radiation, each with a different level of complexity. While increased complexity usually implies increased accuracy, there is also the trade off of increased computational expense. The most complex method is the line-by-line radiative transfer model (LBLRTM). This method computes absorption and emission as a function of wavelength using spectral-line information [90]. A less complex method, although still very detailed, is the rapid radiative transfer model (RRTM), that divides the longwave emission and absorption into a series of spectral bands for each compound [65]. If a broad-band RRTM type model is desired, the Community Atmosphere Model (CAM) from the National Center of Atmospheric Research (NCAR) employs a

sophisticated version, the Column Radiation Model (CRM) [34]. The CRM can be obtained as a stand alone version to be applied to any atmospheric model. The flux-emissivity method treats each atmospheric layer with a single absorption and emissivity that is the average over all wavelengths. The flux-emissivity is obtained from look up tables or parameterizations [90]. The simplest method of parameterizing the longwave radiation at the surface is to specify it, either based on measurements or approximations from the literature. This method may be the best option for many applications due to the greatly reduced computational expense. This research specifies the value from measurements for this reason. However, in order to accurately reproduce an evening transition period, one of the more complex methods may be required (such as the LBLRTM or RRTM), due to the importance of radiative cooling near the surface in the formation of a SBL [91, 92].

2.3 Soil Model

To close the surface budget system of equations (2.1 and 2.2), formulations for the soil heat flux (Q_G) and moisture flux (W_G) near the surface are needed. This is done by implementing a soil model and linking it to the surface budget. It can be assumed that the vertical gradients are much larger than those in the horizontal, so that only heat transfer and moisture transport in the vertical direction are important [84]. As a result, the heat transfer of the soil can be modeled by solving the vertical one-dimensional heat equation (2.20) at each horizontal LES grid location.

$$\begin{aligned} \rho_S c_S \frac{\partial T}{\partial t} &= \frac{\partial}{\partial z}\left(k \frac{\partial T}{\partial z}\right) \\ &= \frac{\partial Q_G}{\partial z} \end{aligned} \tag{2.20}$$

The thermal conductivity, k, soil density, ρ_S, and soil specific heat, c_S, are each functions of soil type and moisture content. Soil parameters have been grouped into 11 USDA (United States Department of Agriculture) textural classes of soil, as presented by Clapp and Hornberger [32] and reproduced in Table 2.1.

Table 2.1. Soil Parameters for 11 USDA Textural Classes and Peat from Clapp and Hornberger [32] and dry volumetric heat capacity from Pielke [73].

Soil Texture	# of Soils	$\eta_{sat}\ \frac{cm^3}{cm^3}$	$\psi_{sat}\ cm$	$K_{\eta_{sat}}\ \frac{cm}{s}$	b	$\rho_i c_i\ \frac{J}{cm^3\,^\circ C}$
Sand	13	0.395	-12.1	0.0176	4.05	1.47
Loamy sand	30	0.410	-9.0	0.01563	4.38	1.41
Sandy loam	204	0.435	-21.8	0.00341	4.90	1.34
Silt loam	384	0.485	-78.6	0.00072	5.30	1.27
Loam	125	0.451	-47.8	0.00070	5.39	1.21
Sandy clay loam	80	0.420	-29.9	0.00063	7.12	1.18
Silty clay loam	147	0.477	-35.6	0.00017	7.75	1.32
Clay loam	262	0.476	-63.0	0.00025	8.52	1.23
Sandy clay	19	0.426	-15.3	0.00022	10.4	1.18
Silty clay	441	0.492	-49.0	0.00010	10.4	1.15
Clay	140	0.482	-40.5	0.00013	11.4	1.09
Peat	-	0.863	-35.6	0.0008	7.75	0.84

The number of soils in Table 2.1 is the number that were found to fit into each soil texture classification, the volumetric heat capacity is for the dry soil, and each of the other values are empirical moisture parameters. The thermal conductivity of the soil varies widely with moisture content. McCumber [62] formulated the variation empirically using data from Al Nakshabandi and Kohnke [68] as

$$k = \begin{cases} 418.46 \exp(-P_f - 2.7) & P_f \leq 5.1 \\ 0.172 & P_f > 5.1 \end{cases} \tag{2.21}$$

in units of $\frac{J}{m\,s\,^\circ C}$ with

$$P_f = \log_{10}\left(\psi_{sat}\left(\frac{\eta_{sat}}{\eta}\right)^b\right) \tag{2.22}$$

where ψ_{sat} is the saturated moisture potential, η is the fractional volumetric moisture content and η_{sat} is the saturated moisture content or the soil porosity in $\frac{m^3}{m^3}$. Values of ψ_{sat}, η_{sat}, b and $K_{\eta_{sat}}$ are determined empirically for the soil texture classifications of Table 2.1, where $K_{\eta_{sat}}$ is the hydraulic conductivity at saturation. The volumetric heat capacity is computed as a weighted contribution of the dry

soil and the liquid water [62] by

$$\rho_S c_S = (1-\eta)\rho_i c_i + \eta \rho_w c_w. \tag{2.23}$$

Where the heat capacity of air within the soil is neglected, since it is much smaller than the other two components.

The porous transport of water in the vertical one-dimensional soil column at each horizontal point is modeled using the equation developed by Richards [76] and first implemented by Philip and de Vries [72]

$$\begin{aligned} \rho_w \frac{\partial \eta}{\partial t} &= \frac{\partial}{\partial z}\left(D_\eta \rho_w \frac{\partial \eta}{\partial z} \right) + \frac{\partial K_\eta \rho_w}{\partial z} \\ &= \frac{\partial W_G}{\partial z} \end{aligned} \tag{2.24}$$

Where K_η is the hydraulic conductivity and accounts for the gravitational drainage in the viscous soil. The diffusive conductivity, D_η, is defined as

$$D_\eta = K_\eta \frac{\partial \psi}{\partial \eta}. \tag{2.25}$$

Using equation 2.25, the soil moisture flux from equation 2.24 can be written as

$$W_G = \rho_w K_\eta \frac{\partial (\psi + z)}{\partial z}. \tag{2.26}$$

In equations 2.25 and 2.24, ψ is the moisture potential and represents the potential energy required to extract water against capillary and adhesive forces in the soil [73]. Clapp and Hornberger [32] empirically related K_η, D_η, and ψ to the moisture content and saturation values of Table 2.1 resulting in equations 2.27 - 2.29, respectively.

$$K_\eta = K_{\eta_{sat}} \left(\frac{\eta}{\eta_{sat}} \right)^{2b+3} \tag{2.27}$$

$$D_\eta = -\frac{bK_{\eta_{sat}}\psi_{sat}}{\eta} \left(\frac{\eta}{\eta_{sat}} \right)^{b+3} \tag{2.28}$$

$$\psi = \psi_{sat} \left(\frac{\eta_{sat}}{\eta} \right)^{b} \tag{2.29}$$

The above equations and parameterizations provide a complete methodology for solving for the soil moisture transport of equation 2.24 and determining the soil moisture content, η, at each soil level. However, to determine the evaporation from equation 2.4, the specific humidity at the surface, q_s, is required since the moisture transfer between the soil and the atmosphere is in the vapor phase. The surface specific humidity can be computed based on the moisture content, η_s, temperature, T_s, and pressure, P_s at the surface. First the saturation vapor pressure (mbar) can be computed from the surface temperature using Tetens approximation as [90]

$$e_{sat} = 6.1078 \exp \left[17.269 \frac{T_s - 273.16}{T_s - 35.86} \right]. \tag{2.30}$$

From the saturation vapor pressure and the pressure at the surface the saturation specific humidity for the given surface temperature is

$$q_{sat} = 0.622 \left[\frac{e_{sat}}{P_s - 0.378 e_{sat}} \right]. \tag{2.31}$$

The saturation specific humidity corresponds to a relative humidity of 100% and would occur if the air contained as much water vapor as it could hold for a given temperature and pressure. The actual surface specific humidity is computed as a fraction of the saturated value using the relative humidity from

$$q_s = h q_{sat}. \tag{2.32}$$

Where the relative humidity, h, can be computed from the surface temperature and the surface moisture potential, ψ, which is a measure of wetness (equation 2.29) [72].

$$h = \exp\left[-\frac{g\psi_s}{R_v T_s}\right] \tag{2.33}$$

2.4 LSM Numerical Implementation

Explicit in the theory of the surface energy budget (equation 2.1) is the assumption that the surface fluxes will sum to zero. Although, in general the summation of the net radiation, soil heat flux, sensible heat flux, and latent heat flux will not equate to zero. Instead the result will equate to a nonzero value, SEB. Substitution of each of the net radiation terms and the surface fluxes into the surface energy budget yields

$$\begin{aligned} \text{SEB} &= R_N + Q_G + Q_S + Q_L & (2.34)\\ &= (1-\alpha)R_{S\downarrow} + R_{L\downarrow} + \epsilon\sigma_{SB}T_s^4 + k\frac{\partial T_s}{\partial z} + \rho_{air}c_p u_{*s}\theta_* + \rho_{air}\lambda_e u_{*s}q_*. & (2.35) \end{aligned}$$

Physically, the net radiation is the forcing term in the surface energy budget and each of the other fluxes respond. The surface temperature determines the partitioning of the available energy between the soil heat flux, and the turbulent fluxes. This is because many of the terms are dependent on the surface temperature and the SEB will approach a balance only for a surface temperature that is near the appropriate value [73]. For clarification, the functional dependence of each surface budget term will be discussed prior to the solution methodology. The longwave radiation emitted by the surface is strongly dependent on the surface temperature, being proportion to T_s^4. The soil heat flux is proportional to the vertical temperature gradient at the surface. After discretization of the gradient, the soil temperature at the second level can be treated as a constant at each time so that the soil heat flux is linearly dependent on surface temperature. The state of the atmosphere (velocity, temperature, and humidity) is also treated to be constant with respect to the surface energy budget at each time.

The sensible and latent heat flux are dependent on the surface temperature through multiple terms. The sensible heat flux depends most directly on surface temperature through the linear difference with the atmospheric temperature (equation 2.3). The strongest dependence of latent heat flux on surface temperature is through the conversion of soil moisture content (η) to specific humidity (equations 2.30-2.33). The sensible and latent heat flux also have a weak dependence on surface temperature through the stability correction (Ψ_H) as a function of the Obukhov length (equation 2.6) and less directly through u_{*s} and its stability correction (Ψ_M). This results in the sensible heat flux having a recursive dependence upon itself.

It is evident that the shortwave and atmospheric longwave radiation do not immediately depend on the surface temperature. The atmospheric longwave radiation is vaguely influenced through positive feedback as an increase in surface temperature will increase the atmospheric temperature and humidity through the sensible heat flux and evaporation. In turn, the increased temperature and moisture will cause an increase in the longwave radiation emitted by the atmosphere. The shortwave radiation is impacted to a lesser extent by the surface temperature, still through a feedback mechanism. As the solar radiation reaching the ground may be effected by the atmospheric transmissivity, which depends on the humidity and temperature. For that reason, the incoming solar and atmospheric radiation are constants at each time with respect to the surface energy budget.

From the above discussion, it should be clear that for a given time both the surface energy budget and moisture budget are functions of surface temperature and moisture content. While many of the other terms vary in time, they are treated as constant with respect to the surface budgets. Therefore, the problem is to determine the surface temperature and moisture content that will result in balanced budgets at each time. The resulting turbulent fluxes are the physically realistic ones that should close the atmospheric governing equations at the surface.

Simultaneous convergence of the surface moisture balance and energy balance to proper surface moisture content and temperature is a difficult and computationally extensive process [62]. To accomplish convergence for each of the balances, they are treated separately. First, it is assumed that the surface soil moisture content is

constant (using the value from the last time) while converging to the proper surface temperature that forces the surface energy balance to approach zero. The diagram of Figures 2.1-2.3 show the flowchart of the LSM algorithm. Since the surface energy budget is now being treated solely as a function of temperature (equation 2.36), the root of the surface energy budget must be found.

$$\mathrm{SEB}\,(T_s) = R_{L\uparrow} + Q_G(T_s) + Q_S(T_s) + Constants \tag{2.36}$$

In practice this is accomplished by approximating the slope of the surface energy budget near zero as

$$\mathrm{SEB}'\,(T_s^n) = \frac{\mathrm{SEB}\,(T_s^n) - 0}{T_s^n - T_s^{n+1}}. \tag{2.37}$$

Rearranging equation 2.37, an improved estimate for the surface temperature is obtained from the Newton-Raphson formula [29].

$$T_s^{n+1} = T_s^n + \frac{\mathrm{SEB}}{\mathrm{SEB}'} \tag{2.38}$$

Numerical differentiation of the surface energy budget is noisy and not conducive to convergence. By assuming that u_{*s}, Ψ_H, and Ψ_M are not functions of temperature, the derivative of the surface energy budget can be obtained analytically [58] to be

$$\mathrm{SEB}' = 4\epsilon\sigma_{SB}T_s^3 + \frac{k}{\Delta z} + \frac{\kappa u_{*s}}{ln(\frac{z}{z_t}) + \Psi_H(\frac{z}{L}) - \Psi_H(\frac{z_t}{L})}. \tag{2.39}$$

The Newton-Raphson technique is applied until the change in surface temperature, ΔT_s, is less than 0.001% of T_s. Once a temperature is obtained that satisfies the surface energy budget, the sensible heat flux is recomputed. If the change in flux is too large, the stability parameters (Ψ_H and Ψ_M terms) and turbulent fluxes are recomputed using the new surface temperature. This secondary iterative process is continued until the change in sensible heat flux is small, chosen such

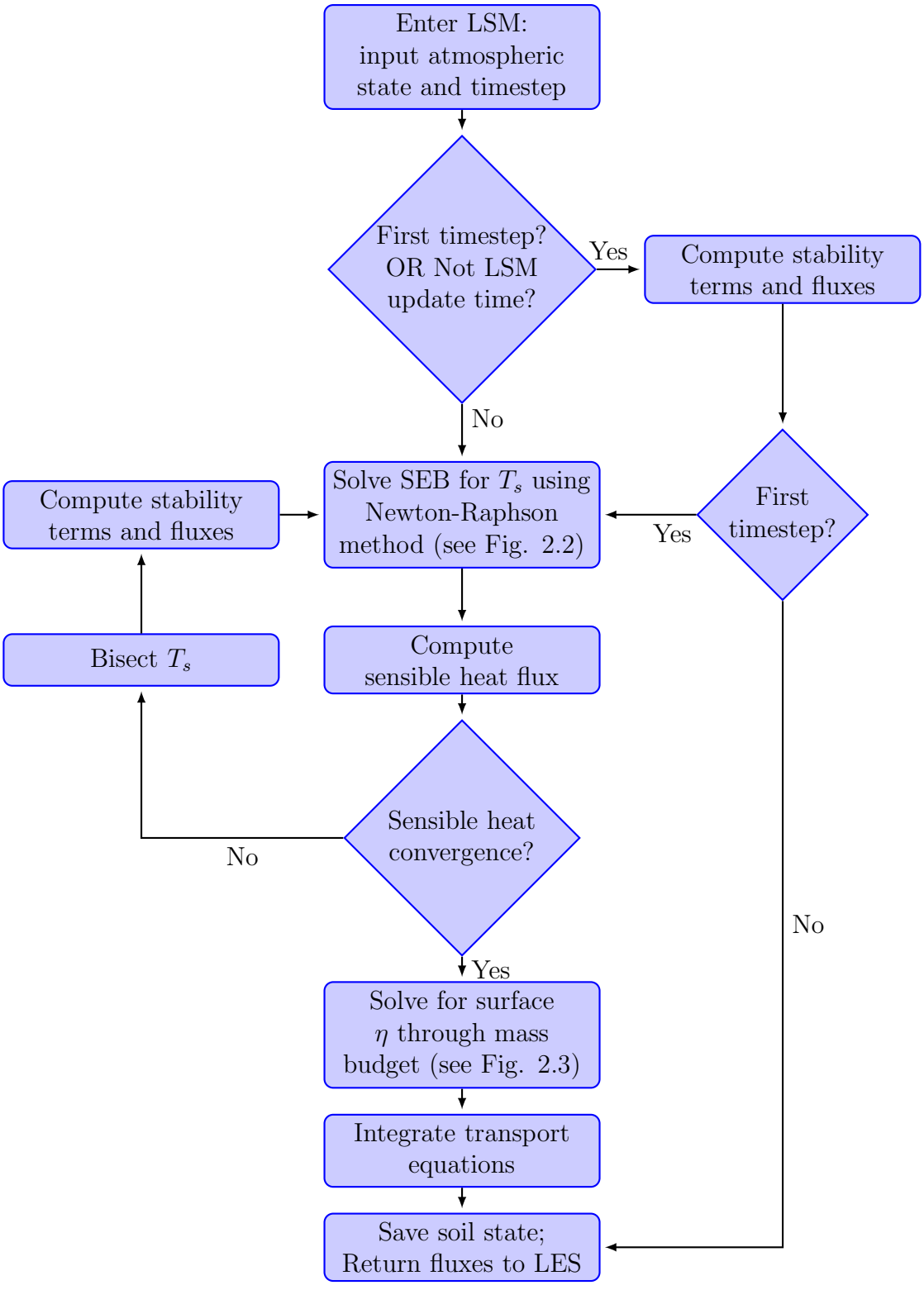

Figure 2.1. Flowchart of land-surface model solution.

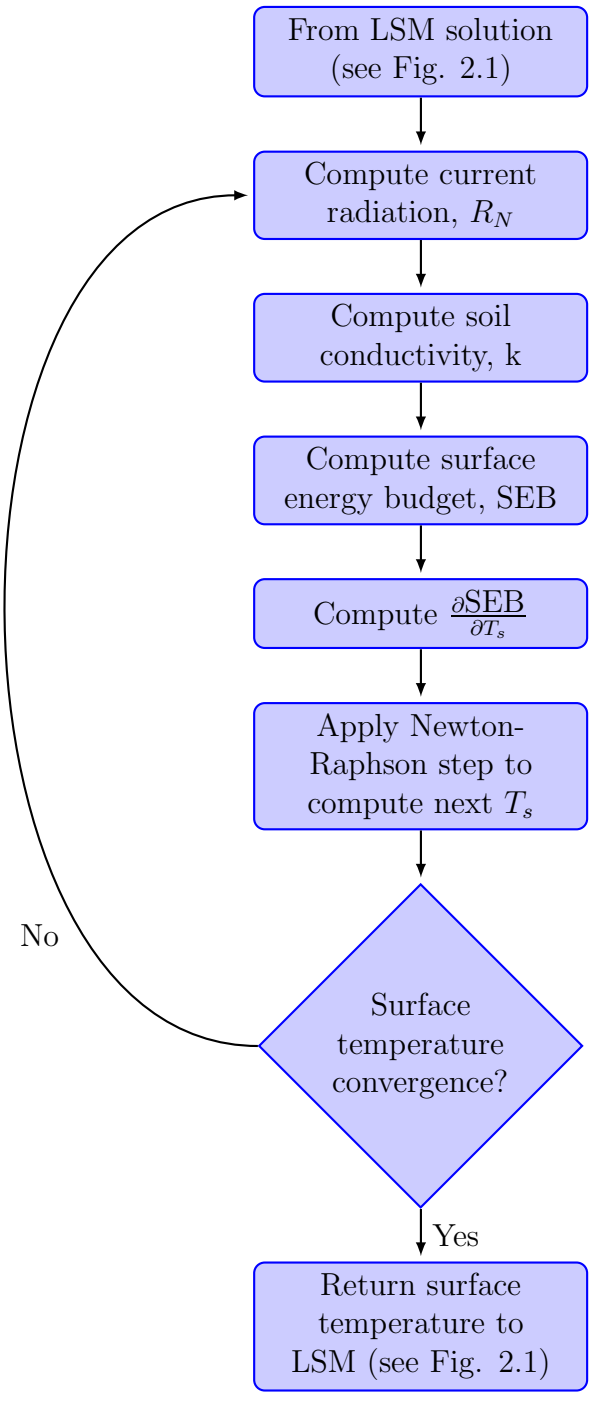

Figure 2.2. Flowchart of surface energy budget Newton-Raphson solution.

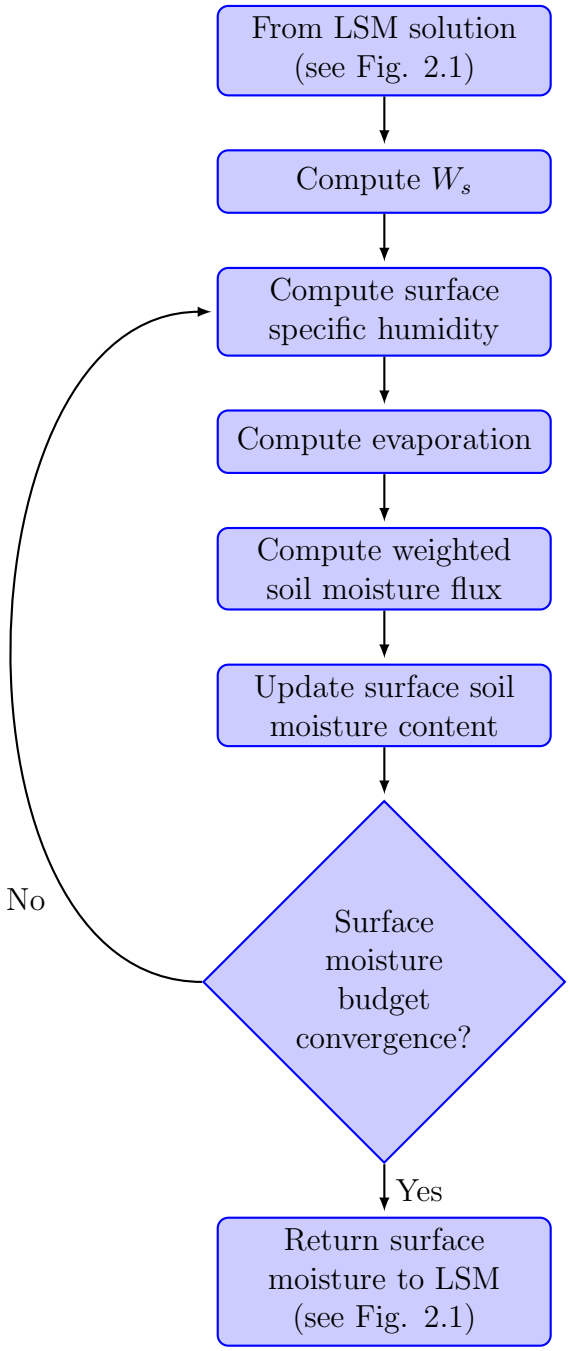

Figure 2.3. Flowchart of surface moisture budget iterative solution.

that $\Delta(u_{*s}\theta_*) < 1\text{x}10^{-5}$. Therefore, the Newton-Raphson iterative convergence to a valid surface temperature is nested within the outer convergence to a sensible heat flux. Convergence is improved by bisecting the surface temperature within the outer iteration, after the sensible heat convergence test, this reduces oscillations in the sensible heat flux.

Next, the surface temperature is treated as a constant in the surface moisture balance while converging upon the surface soil moisture content that results in a balance between the soil moisture flux and evaporation. First, the soil moisture flux at the surface is computed from

$$W_s = D_\eta \rho_w \frac{\partial \eta}{\partial z} + K_\eta \rho_w. \tag{2.40}$$

During each iteration, equations 2.30-2.33 are used to update the specific humidity at the surface, which is then used to recompute the evaporation. A new soil moisture flux near the surface is computed from a weighted average of the last value and the new evaporation as

$$W_s^{n+1} = \delta_m W_s^n + (1 - \delta_m)\rho_{air} u_* q_* \qquad 0 \leq \delta_m \leq 1. \tag{2.41}$$

McCumber [63] found 2.41 to improve the convergence of the surface moisture balance, with $\delta_m > 0.5$ leading to faster convergence and for dryer soils δ_m strongly skewed toward one. The appropriate surface soil moisture content from the new soil moisture flux is computed from 2.26. In finite difference form this gives the surface moisture potential as

$$\psi_s = \psi_{s-1} + \Delta z_s \left[\frac{W_s}{\rho_w K_\eta} - 1 \right]. \tag{2.42}$$

The result of 2.42 is used to obtain the surface moisture content through equation 2.29. Using the new surface moisture content, the turbulent moisture flux and the soil moisture flux are recomputed from 2.4 and 2.41, respectively. This is

repeated until the moisture fluxes converge by the criteria [40]

$$\left| \frac{\rho_{air} u_{*s} q_* - W_s}{\rho_{air} u_{*s} q_*} \right| < 0.001. \tag{2.43}$$

Once the surface values are obtained, the sub-surface soil state is updated by integrating the heat transfer equation (2.20) and moisture transport equation (2.24) in time. A fully implicit Crank-Nicholson scheme is applied to the heat diffusion equation. This scheme is second order accurate and stable for all time intervals [29]. In order to improve the stability of the moisture transport equation, the hydraulic conductivity is linearized by

$$K'_\eta(\eta^n) = \frac{K_{\eta_{sat}}}{\eta_{sat}} \left(\frac{\eta^n}{\eta_{sat}} \right)^{2b+2}. \tag{2.44}$$

This allows the moisture transport equation to also be solved using a fully implicit scheme [84]. The finite difference formulations for 2.20 and 2.24 are written as

$$\begin{aligned} \frac{T_i^{n+1} - T_i^n}{\Delta t} &= \frac{1}{2(z_{i+\frac{1}{2}} - z_{i-\frac{1}{2}})} \left(k_{i-\frac{1}{2}} \frac{T_{i-1}^{n+1} - T_i^{n+1}}{z_i - z_{i-1}} - k_{i-\frac{1}{2}} \frac{T_i^{n+1} - T_{i+1}^{n+1}}{z_{i+1} - z_i} \right) \\ &\quad + \frac{1}{2(z_{i+\frac{1}{2}} - z_{i-\frac{1}{2}})} \left(k_{i-\frac{1}{2}} \frac{T_{i-1}^{n} - T_i^{n}}{z_i - z_{i-1}} - k_{i-\frac{1}{2}} \frac{T_i^{n} - T_{i+1}^{n}}{z_{i+1} - z_i} \right) \end{aligned} \tag{2.45}$$

$$\begin{aligned} \frac{\eta_i^{n+1} - \eta_i^n}{\Delta t} &= \frac{1}{z_{i+\frac{1}{2}} - z_{i-\frac{1}{2}}} \left(D_{\eta_{i-\frac{1}{2}}} \frac{\eta_{i-1}^{n+1} - \eta_i^{n+1}}{z_i - z_{i-1}} - D_{\eta_{i-\frac{1}{2}}} \frac{\eta_i^{n+1} - \eta_{i+1}^{n+1}}{z_{i+1} - z_i} \right) \\ &\quad + \frac{1}{z_{i+\frac{1}{2}} - z_{i-\frac{1}{2}}} \left(K'_{\eta_{i+1}} \eta_{i+1}^{n+1} - K'_{\eta_{i-1}} \eta_{i-1}^{n+1} \right) \end{aligned} \tag{2.46}$$

The Neumann BC is enforced at the bottom of the soil by setting the flux to zero for both scalar transport equations. The soil is linked to the surface budget equations through the Dirichlet BC of a specified surface state applied in the integration of 2.45 and 2.46.

With the LES domain discretized on the order of meters, the atmosphere solution is incremented at time steps on the order of fractions of a second. It was

found that the surface budget and corresponding fluxes only need updating on the order of minutes, reducing the computational expense of the land-surface model by a factor of hundreds compared to computing the LSM at every LES time step.

This completes the land-surface model, after which, the fluxes of 2.3-2.5 are passed to the LES solution to close the filtered governing equations at the surface. The soil temperature and moisture state is stored to be used at the next time, given updated atmosphere conditions and current radiative forcing. The LSM surface fluxes, as described above, are more physically realistic than the common LES alternative of specifying surface states or fluxes. The LSM should more accurately reproduce the diurnal variation and the coupling between sensible and latent fluxes. Additionally, the LSM provides temporal and spatial predictions of soil state.

CHAPTER 3

EXPERIMENTAL DETAILS

Chapter 2 described in detail the LSM applied for this LES research. The model includes many parameterizations and simplifications for complex physical phenomena. The goal of the LSM is to improve the physical representation of the land-atmosphere interactions and provide time evolving surface fluxes so that the ABL can be accurately predicted. The best way to analyze the simulation results is to compare to theory and field measurements. However, accurately simulating the ABL to match observations requires detailed field measurements for initialization and forcing that are not commonly available. For example, to initialize the simulation the atmospheric conditions should be based on observations. Additionally, large scale motions that are greater than the LES domain, such as advection and geostrophic forcing, must be input and will vary with time and height. The LSM BC requires that the surface and sub-surface must be suitable to meet the assumptions of the LSM, namely, a relatively horizontal surface composed of soil and at most a simple vegetation cover (to be neglected). The LSM also requires added initialization inputs, including vertical profiles of soil states (moisture content and temperature) and soil composition. Specifically, measurements of soil moisture profiles and soil surface temperature values are prone to error [20]. For these reasons, it is not trivial to compare the coupled LSM-LES results with experimental field data for validation and comparison.

In 2008-2009, a LES intercomparison study of the SBL was undertaken under the auspices of the Global Energy and Water Cycle Experiment (GEWEX). The third GEWEX ABL study (GABLS3) LES intercomparison case is based on a baroclinic, moderately SBL observed at a mid-latitude location over Cabauw, The Netherlands on July 1st, 2006. The goal of the GABLS3 intercomparison was to

study the physics of the SBL using LES and evaluate SGS models in moderately stratified flow conditions [8]. The GABLS3 case was chosen for this research for multiple reasons, including the availability of detailed atmospheric forcing and LSM input parameters. An additional benefit is the relatively simple and homogeneous surrounding terrain. Section 3.1 will describe important aspects of the Cabauw meteorology site and sensors and corresponding data applicable to GABLS3. Details of the GABLS3 LES and the specified input parameters will be laid out in section 3.2, followed by the additional inputs required for the LSM-LES study conducted for this research.

3.1 The Meteorological Site

The Cabauw experimental site for atmospheric research (CESAR) is located in the middle of the Netherlands (51°58'13" N 4°55'34" E) as shown in the map of Figure 3.1. The site includes a 213 m tower (shown in Figure 3.2) located about a kilometer from the Lek river (a distributary of the Rhine) that has been in continuous operation since 1986. The surrounding terrain is flat and largely composed of meadows separated by narrow ditches with scattered tree canopies, roadways and villages. The meadows have short grass, used for grazing and hay production. Particularly, at the CESAR measurement field, the surface has thick grass that is kept at about 8 cm by frequent mowing. Approximately a few hundred meters in all directions surrounding the tower there are no large obstructions to the flow. In the dominate southwest wind direction the upwind flow is unrestricted for about 2 km [13]. Figure 3.3 shows photographs of the terrain surrounding the Cabauw site viewed from three different directions from the top of the 213 m tower. These images show that the surrounding area is relatively homogeneous and flat. This type of domain is important for this LES case, which does not model specific impediments to the flow and only treats momentum drag through an average roughness at each node. Additionally, the surface type is essential for the LSM implementation that regards each node as homogeneous and flat.

Within the CESAR the ditches are parallel and spaced an average of 40 m apart. The water level is controlled to remain at about 40 cm below the surface to

keep the deep soil constantly saturated. According to Beljaars, et al. [13] the water table height depends on the vicinity of the nearest ditch and the recent weather conditions. After ample rain it can be very near the surface, but can recede to around 75 cm after an extended dry period.

3.1.1 Instrumentation and Data

The CESAR is an excellent choice to base a numerical experiment on, not only due to the regional characteristics, but also because of the extensive array of instruments that continually record data. The site is one of the best instrumented meteorological measurement sites in the world [19].

Profiles of wind speed, wind direction, temperature and humidity are available along the tower at 10, 20, 40, 80, 140 and 200 m. At the time of GABLS3, the Cabauw site was equipped with Royal Netherlands Meteorological Institute (KNMI) cup-anemometers for measuring wind speed and KNMI wind vanes for wind direction. At each of the four highest levels (40, 80, 140 and 200 m), wind direction measurements were taken on three booms facing three different directions to avoid flow obstruction from the tower and main building. In 10 minute time periods the most appropriate reading was chosen based on the wind direction. Wind speed is measured on two of the booms (Southwest and North). At the two lower levels (10 and 20 m), the wind speed and direction were measured on two separate masts South and North of the main building. Air and dew point temperature were measured at the same heights, in addition to 1.5 m. The highest four measurements were taken from the southeast boom of the tower and the lowest three from the south mast. Air temperature was measured using a PT-500 and dew point temperature was obtained with a Vaisala HMP243 [20].

Turbulent surface fluxes of momentum and sensible and latent heat were obtained using the eddy correlation method from data obtained at a height of 5 m, approximately 200 m south of the main tower. The turbulence data was collected at 10 Hz with a Kaijo-Denki TR60-A sonic anemometer (velocity and temperature) and a LICOR 7500 open path H_2O/CO_2 sensor (humidity). Fluxes were averaged over a ten minute period.

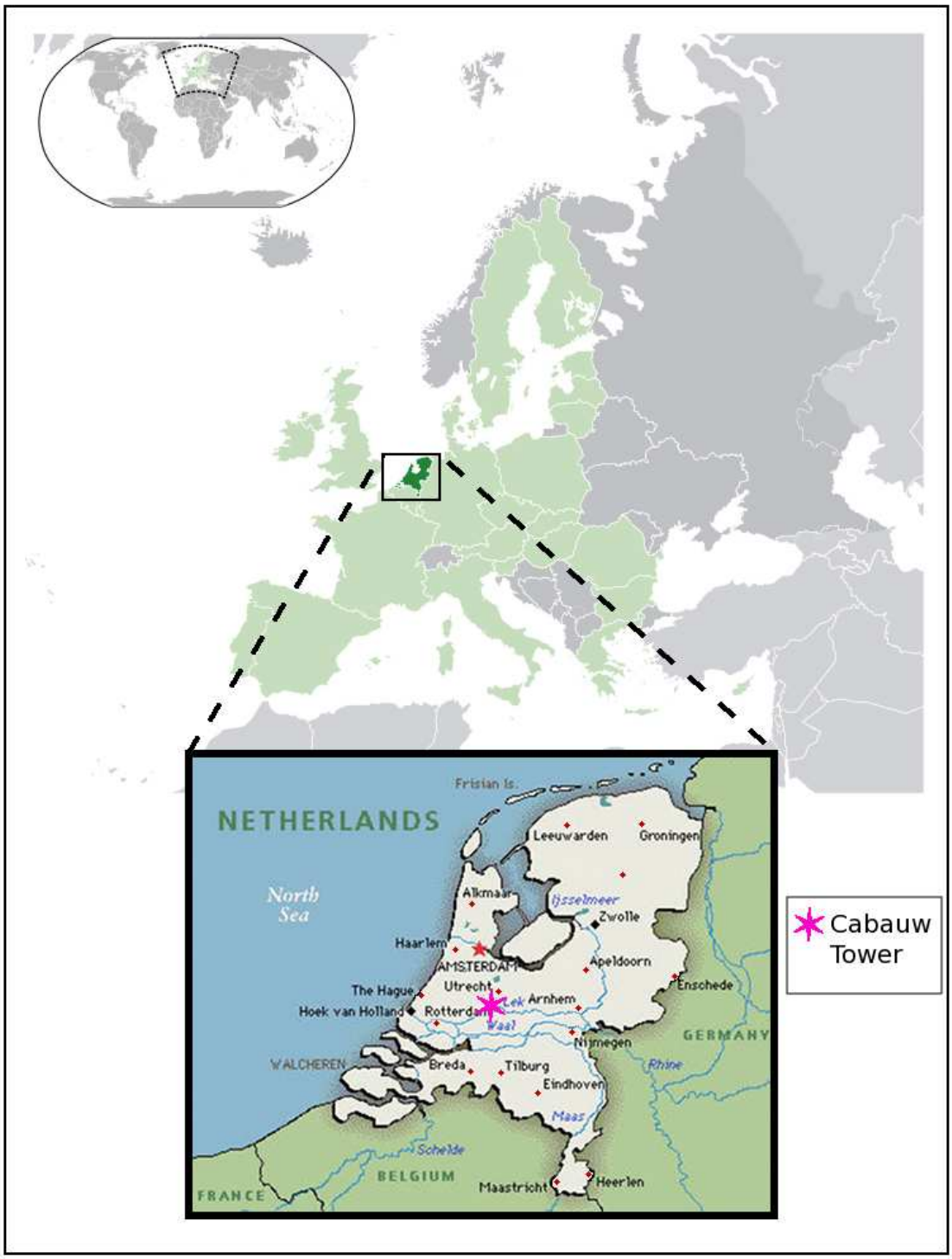

Figure 3.1. Location of the GABLS3 meteorological site in Cabauw, The Netherlands (51°58'13" N 4°55'34" E) [95, 3].

Figure 3.2. The Cabauw Experiment Site for Atmospheric Research (CESAR) used for the GABLS3 intercomparison study, showing the 213 m mast and radiation sensors (image courtesy of the BALTEX Office [93]).

Figure 3.3. Photographs of the terrain surrounding the Cabauw site viewed from different directions from the top of the 213 m tower (Fig. 3.2). Depicted to show the scale of heterogeneity and roughness (images courtesy of the BALTEX Office [93]).

There was a bare soil region approximately 50 m south of the tower where the soil heat flux is measured using six TNO-Delft WS31S soil heat flux plates. Three sets of plates were arranged in an equilateral triangle, separated by 2 m, and buried at depths of 0.05 and 0.10 m. Fourier decomposition was used to obtain the average soil heat flux at the surface [20]. Soil temperatures were measured at another bare soil region, 100 m south of the tower. KNMI nickel wired needles were buried at depths of 0.5, 2, 4, 6, 8, 12, 20, 30 and 50 cm.

The soil moisture content was also measured at the soil region 100 m south of the tower using three TDR CS615 sensors buried at depths of 4, 8 and 20 cm. The water table was measured at 5 positions along an east-west line 100 m south of the tower. Keller 26W/8369 pressure sensors were placed in a 4.82 cm diameter tube that extends 1.5 m below the soil surface.

Each component of the net radiation was measured in the field south of the tower at a height of 1.5 m. Two Kipp Zonen CM11 pyranometers measured the short wave radiation. The downward facing sensor was on a 1 m boom and both of the porting structures were painted black to get a well defined radiation condition. Also placed on 1 m booms were two Eppley pyrgeometers for measuring longwave radiation. Each of the sensors were ventilated to avoid dew formation and the longwave sensors had thermistors for temperature compensation. In addition to each of the components, net radiation was measured using a Schulze LXG055 net radiometer on a 0.8 m boom and a height of 1.5 m. The sensor measured the total upward and downward radiation separately [20].

In addition to the sensors and data that are useful for the current study, the CESAR has many other sensors such as gas analyzers for CO_2 concentration and a ceilometer for cloud structure detection. A complete list of the CESAR instrumentation is available in Table 3.1, modified from Boers [17, 77].

3.2 LES-LSM Numerical Experiment Details

3.2.1 GABLS3 LES

It can be difficult to extract from observations the proper information needed for LES. Conveniently, those managing the GABLS3 have completed this task for the

LES intercomparison study. Details of the initial conditions, forcing parameters and BCs were provided by Basu et al. [7] to ensure each model (from various groups) were run the same with the only difference being the numerical code and SGS treatment. The simulations in this research used pseudo-spectral solution methods and the scale-dependent Lagrangian dynamic SGS model [86]. In the intercomparison study each group chose which SGS model to apply, usually the one that would be expected to perform the best.

An 800 m^3 domain was specified with a baseline simulation of 128^3 points (6.25 m resolution). For this research, additional resolutions of 192^3 and 256^3 were run for resolution sensitivity testing. A gravity wave damping layer was applied above 600 m to limit gravity wave reflection at the top of the domain. The vertical velocity was set to zero at the surface and the top of the domain and free slip was enforced for the upper BC. An upper inversion was set to 0.0029 K/m. For the lower BC, near the surface, Monin-Obukhov similarity was applied (equations 2.3-2.5) using a surface roughness length (z_o) of 0.15 m, a von Karman constant (κ) of 0.4 and

Table 3.1. List of instruments routinely operated at CESAR (modified from Boers et al. [17, 16]).

Remote Sensors	**Tower (in situ)**	**Ground (in situ)**
Wind profiler	SJAC	Rain Gauges
Ceilometer	LAS-X	Disdrometer
IR-radiometer	FSSP-95	TDR
3 GHz Radar	Nephelometer	Radiosondes
35 GHz Radar	Sonic Anemometer	Brewer Spectrophotometer (O_3)
Backscatter Lidar	Gas Analyzer (CO_2)	Optical Particle Counter
GPS Receiver	Aethalometer	Sun Photometer
Microwave Radiometer	Humidograph	Total Sky Imager
UV Radiometer	Wind Vane & Cup Anememeter	BSRN
Scintillometer	Temperature Sensor	Soil Heat Flux
Pyranometer		Soil Temperature
Pygeometer		PM2.5 & PM10
		NO_x, O_3, SO_2
		Water Content & Table

stability corrections of

$$\Psi_M = \Psi_H = \Psi_Q = \frac{5z}{L} \tag{3.1}$$

for stable conditions. To avoid a land-surface model, the sensible and latent heat flux were computed using prescribed 0.25 m air temperature and humidity. Values were provided hourly, as available in the Appendix Table B.1, and linearly interpolated in time. This results in the Monin-Obukhov similarity formulation becoming

$$u_{*s}\theta_* = \frac{\kappa u_{*s}(\theta - \theta_{0.25})}{ln(\frac{z}{0.25}) + \Psi_H(\frac{z}{L}) - \Psi_H(\frac{0.25}{L})}, \tag{3.2}$$

where a value of z_t is not needed. Periodicity was enforced for the horizontal BCs.

Initial atmospheric profiles of velocity, potential temperature and specific humidity (reproduced in Appendix Tables B.2-B.3) were provided based on measurements at the LES start time. In order to initialize turbulence, an initial random perturbation with a Gaussian distribution was applied to the lowest 200 m of the atmospheric velocity components (u and v) and potential temperature. Each distribution was specified to have a zero mean and a variance of

$$0.2\left(1 - \frac{z}{200}\right)^2 \tag{3.3}$$

applied to the velocity components and 0.1 variance applied to the potential temperature.

The surface geostrophic wind was linearly interpolated in time from discrete values given in Table B.4 of the Appendix. At each time, the geostrophic wind was linearly interpolated between the surface values and values of U_{geo}=-2.0 m/s and V_{geo}=2.0 m/s at 2000 m. Large scale advection of each of the atmospheric variables is added in as a force, with the rate of change given as a function of time

in Tables B.5-B.7 in the Appendix. The listed values are constant from 200-800 m and linearly interpolated to zero at the surface.

3.2.2 LSM

Initial conditions and other parameterizations for the LSM were not provided for GABLS3. The simplified lower BC, based on measured values, made this information unnecessary. The LSM inputs for this study have been collected from two sources, the repository of measurements for the CESAR and documentation on the project for intercomparison of land surface parameterization schemes (PILPS) [30]. Each atmospheric column lies above a unique column of soil that was discretized using a stretched vertical grid with nodes at 0.0, 0.005, 0.01, 0.02, 0.04, 0.06, 0.08, 0.12, 0.20, 0.30, 0.50, 1.0, 2.0 m below the surface. For PILPS the vertical soil composition was described as in Table 3.2. The soil characteristics were obtained

Table 3.2. Cabauw vertical soil composition (modified from [13]).

Depth (cm)	**Soil Characterization**
0-3	turf zone
3-18	35-50% clay, 8-12% organic matter, high root density
18-60	45-55% clay, 1-3% organic matter, low root density
60-75	mixture of clay and peat
75-700	peat

from Jager et al. (1976) by inspection of the soil profile in a 120 cm deep profile pit and analysis of laboratory samples [13]. In this study the turf and roots are neglected and the organic matter is treated as peat. At each height, the properties of the soil (η_{sat}, ψ_{sat}, $K_{\eta_{sat}}$, b and $\rho_i c_i$) are weighted from the values in Table 2.1. At depths between 60-75 cm. the mixture is defined as 50% clay and 50% peat, although the ratio is not specified in Table 3.2.

The soil moisture content (η) and soil temperature profiles were initialized based on measurements from the CESAR and are included in Table C.1. The initialization of the deepest levels of the soil are less important, since on the time scales of LES there is little change in these levels. The levels of the soil that are lower than the

measured values of 20 cm for the moisture content and 50 cm for the temperature are approximated using the suspected trend. The soil moisture content increases with depth and soil temperature cools with increasing depth.

At the surface, the albedo depends on the soil moisture content as parameterized in equation 2.16- 2.18 with $\alpha_1 = 0.33$ and $\alpha_2 = 0.13$ given for PILPS [13]. The solar radiation is computed for the time of day and the Cabauw location at a latitude of 51°58'13" north and longitude of 4°55'34" east. The simulation is started at 0000 hours UTC 2 July 2006 and run for 9 physical hours. To avoid errors and increased computational expense from an atmospheric longwave radiation model, the net longwave radiation was set as a constant -0.04 K m/s from measurements at the Cabauw site during the July night. The surface latent heat flux is related to evaporation (equation 2.1) by the latent heat of vaporization, $\lambda_e = 2450\frac{kJ}{kg}$, ignoring the weak dependence on temperature.

With the application of the LSM, the first atmosphere level is connected to the surface through Monin-Obukhov similarity (equations 2.3-2.5). For the sensible and latent heat flux, the heat roughness length (z_t=0.0015 m) given for the GABLS3 single column model (SCM) intercomparison study [18] is adopted. Based on measurements from the Cabauw site, Beljaars [14] suggests that z_t could range between 0.015 m and 1.5×10^{-6} m and may depend on z_o in the direction of the upstream wind. Physical interpretation explaining why z_t would vary is more difficult than for z_o and is beyond the scope this paper. However, using a constant value for either is an over simplification.

CHAPTER 4

EVOLUTION OF SURFACE FLUXES, BOUNDARY LAYER FEATURES AND SPATIAL STATISTICS

4.1 Time Series of Surface Fluxes and Boundary Layer Characterizations

Within the context of LES the purpose of the LSM is to predict surface fluxes that close the atmospheric governing equations at the land surface interface. Analysis of the surface fluxes is the most direct method of determining the accuracy of the LSM and differences between the LSM and other BC formulations. Figure 4.1 shows the horizontally averaged value of each term in the surface energy budget as a function of time. The stars are measured values from the CESAR and the curves are results from the coupled LSM-LES. The net radiation forces the surface energy budget and limits the total available energy. Therefore, accurate prediction of the net radiation is important to ensure the proper amount of energy is available for partitioning to each of the other flux terms. The predicted net radiation matches the measured value very well. At night the only contribution to the net radiation is the longwave radiation emitted by the surface and the atmosphere. This net longwave radiation was specified in the LSM from observations and, as a result, is expected to match well during the night (see section 3.2.2). During the sunrise, around 0400 hours the observed net radiation transitions gradually due to the diffuse solar radiation. The modeled incoming solar radiation from equation 2.15 has a piecewise on-off formulation and does not account for diffuse radiation so that a discrete point of non differentiability is expected at sunrise. The daytime net radiation matches well, although it diverges from measurements as the morning progresses. This

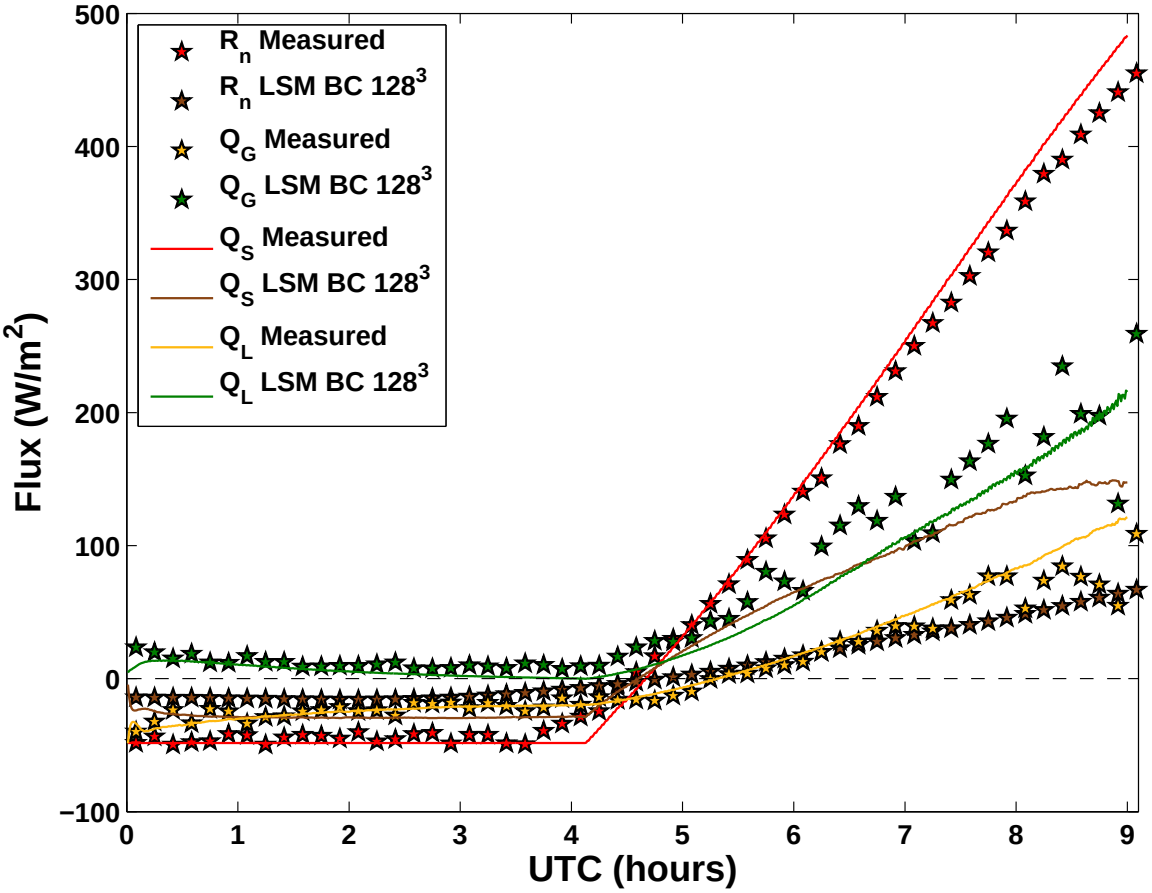

Figure 4.1. Each term of the surface energy budget from measurements and horizontally averaged LSM-LES predicted values for 2 July 2006.

divergence could be a result of an inaccurate albedo parameterization, incoming short wave radiation or a combination of both.

Another term of the surface energy budget is the soil heat flux. The predicted LSM value follows the same trend as observations, however the magnitude is over predicted for nearly the entire simulation. There are many possible explanations for this. One is a poor model in for the soil conductivity as a function of moisture content (equation 2.21). Although the modeled soil heat flux deviates from the observations, each of the turbulent heat fluxes (latent and sensible) still match measured values well (discussed below). This implies that the total sum of the surface energy budget does not match between the observations and the LSM. The LSM surface energy budget is forced to sum to zero at each time. It follows that the measured surface energy budget does not sum to zero. An imbalance in the observed surface energy budget is a known problem in micrometeorology [48, 19, 13]. Furthermore, the imbalance at the CESAR has been documented to increase with decreasing wind speed during stable conditions [21].

Time series of the turbulent heat fluxes are shown separately in Figure 4.2 along with LES predicted values from the GABLS3 BC. The GABLS3 fluxes were computed from prescribed 0.25 m temperature and moisture based on measured values as described in section 3.2.1. In addition, the relative errors of the sensible and latent heat flux for the LSM BC and GABLS3 BC are shown in Figure 4.3. Shortly after sunrise where the observed sensible heat flux is very close to zero the meaningless relative error is not included. The sensible and latent heat from both BCs have a period of adjustment during the first 15-30 minutes of the simulation. After the adjustment period, the LSM sensible heat flux lies between the spread of the observations until 0800 hours, after this time the measurements divert from the trend. The original GABLS3 LES was able to capture the change, which suggests that the inaccurate LSM sensible heat flux during the last hour is due to a feature captured by measurements in the GABLS3 BC, but not by the LSM BC.

The spread in measured values of the turbulent heat fluxes range up to 45% of the magnitude. Therefore, it can be concluded that prediction errors within this range are within the accuracy of the measurements and can be considered a

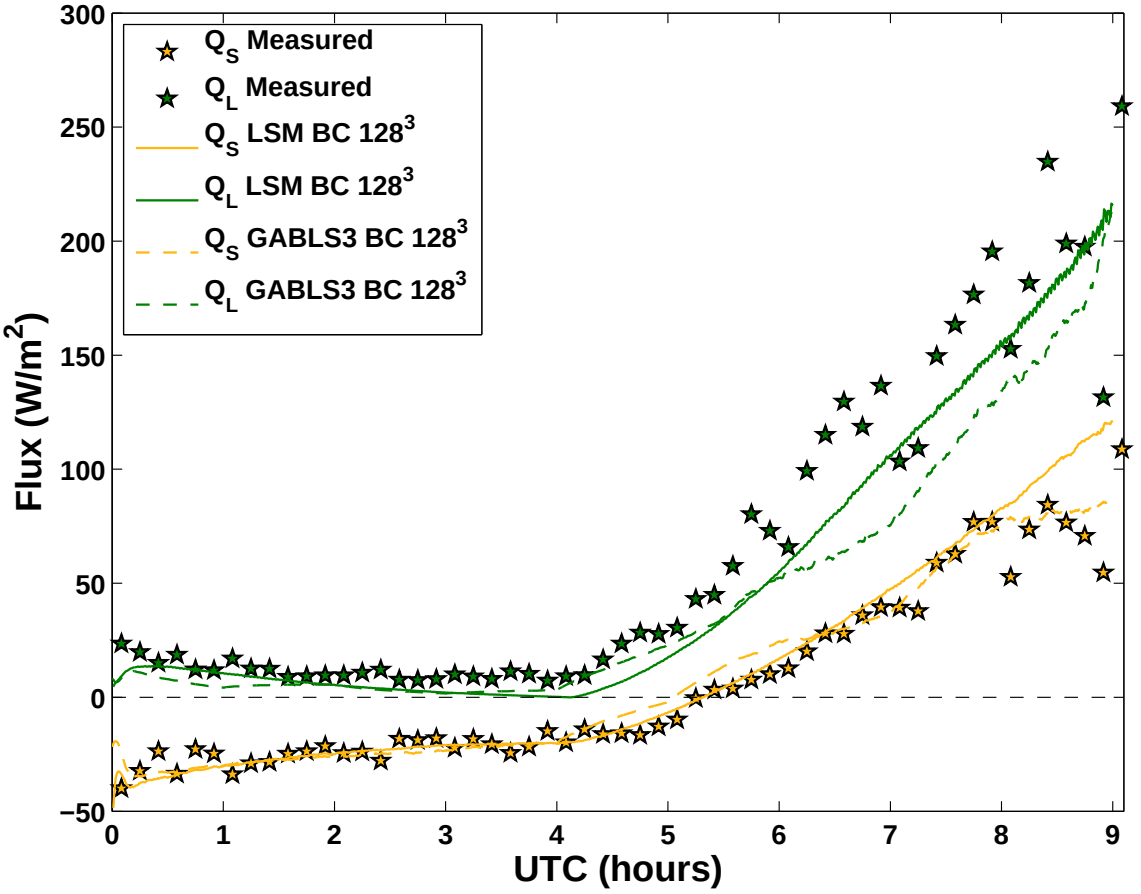

Figure 4.2. Sensible and latent heat flux from measurements and horizontally averaged predicted values from the LSM-LES and GABLS3 LES for 2 July 2006.

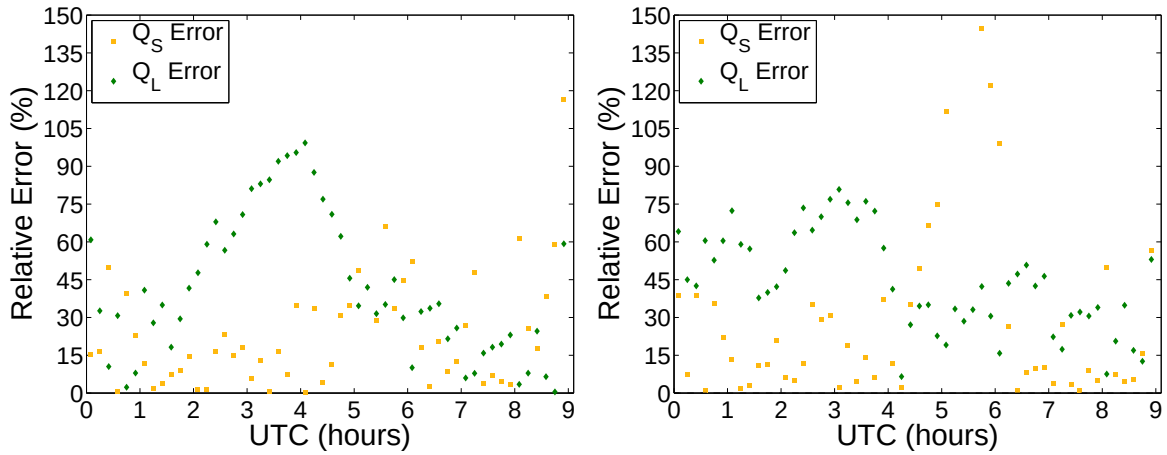

Figure 4.3. Sensible and latent heat flux relative errors for the LSM-LES (left) and the GABLS3 LES (right).

good prediction. During a large portion of the simulation, the predicted heat fluxes exhibit relative errors less than 45%. For example, the LSM predicted sensible heat flux from the start of the simulation until 0500 hours results in a low relative error, less than 45%. The error in sensible heat flux is larger near the transition, around 0530 hours. Although this is strongly dependent on the very small values of measured flux, the error between the two BC can be compared. From 0530-0600 hours, the LSM sensible heat flux relative error ranges from 30-70%, while the GABLS3 relative error ranges between 100-145%. During the last hour of the simulation, the LSM BC produces the largest relative error growing from 30% to 115% just before 0900 hours. The predicted net radiation also has the largest relative error at the end of the simulation.

After the initial adjustment period, the LSM latent heat flux compares well to the observations for the first two hours with relative errors of less than 45%. Afterward, the evaporation decreases too rapidly during the night. This results in relative errors approaching 100% as the LSM evaporation approaches zero around 0400 hours. In comparison, the GABLS3 latent heat flux is under predicted from the start of the simulation until 0400 hours with relative error ranging between 45-80%. Although the value is under predicted, the rate of decrease of the GABLS3 BC latent heat flux matches the measured rate closer than the LSM. The GABLS3 latent heat flux continues to be under predicted for the entire simulation. After sunrise, the LSM latent heat flux increases and follows the trend of the measured latent heat flux as the surface temperature increases. The LSM latent heat flux remains under predicted for the remainder of the simulation, yet the relative error decreases to less than 30%. From 0600-0900 hours, the LSM latent heat flux compares noticeably better than the GABLS3 latent heat flux. Additionally, the GABLS3 heat fluxes contain an unrealistic piecewise artifact from the BCs that were linearly interpolated from hourly values, whereas the LSM fluxes are smooth from continuously adjusting conditions.

The GABLS3 LES BC neglects any consideration of the surface by specifying the state of the atmosphere at a height between the surface and the first LES level. In comparison, the LSM predicts the surface state at each horizontal node and

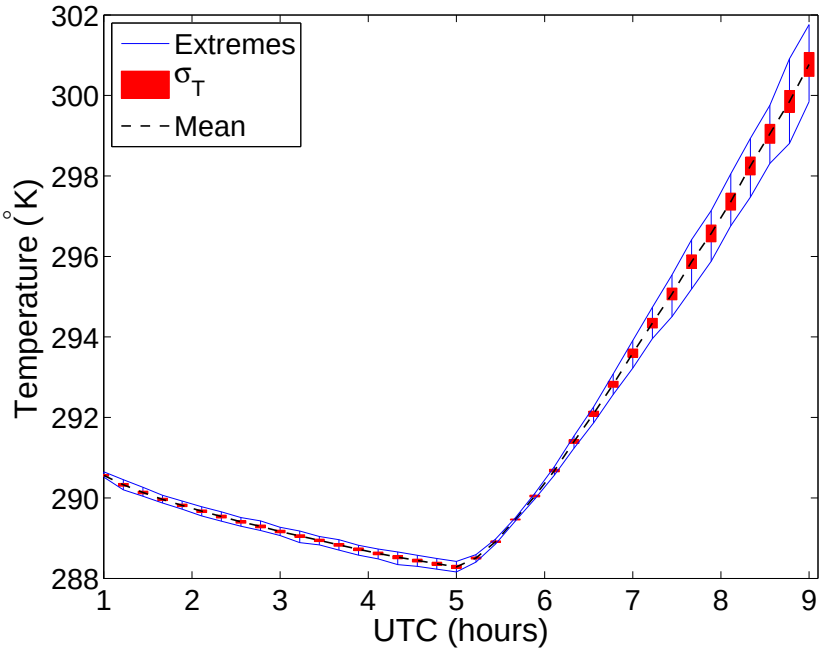

Figure 4.4. LSM predicted surface temperature statistics: mean (dashed black), extremes (solid blue) and standard deviation (red bar).

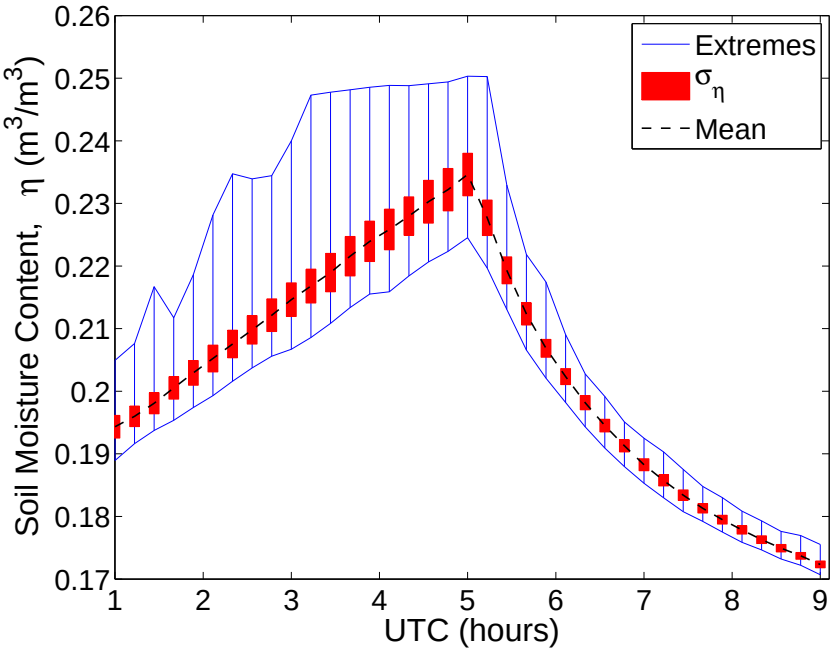

Figure 4.5. LSM predicted surface soil moisture content statistics: mean (dashed black), extremes (solid blue) and standard deviation (red bar).

at every time step, providing additional state information. Figures 4.4 and 4.5 depict the temporal evolution of statistics of surface temperature and surface soil moisture content, respectively, as predicted by the LSM. The blue curves show the extreme states, the black dotted curve shows the mean state, and the vertical red bar shows the standard deviation about the mean. All statistics are computed from instantaneous surface states starting at 0100 hours. The spread between extreme values of the surface temperature increases with time as the surface cools from 0100-0500 hours. The soil states are initialized with zero spatial variance, therefore, the variance in the surface temperature must adjust until it reaches an equilibrium with the turbulence in the atmosphere. As the surface warms (0500-0900 hours), the spread between extreme values and the standard deviation is correlated to the magnitude of the sensible heat flux. This also indicates that the variance in the surface temperature is correlated to the turbulent structure and stability of the atmosphere. The atmospheric variances further support this trend and are discussed below (section 4.3). The correlation between the surface and atmospheric variances implies that the surface flux variance follows the same trend. The surface soil moisture content exhibits an increase in the spread between extreme values and standard deviation during the stable period. During the convective period the spread between extreme values and the standard deviation of the surface soil moisture content decreases as the surface dries. This is probably due to the soil moisture content approaching the wilting point.

Figure 4.6 displays the evolution (from 0100-0900 hours) of the LSM-LES predicted and measured soil temperatures at depths of 0, 2, 4, 8 and 12 cm. The predicted temperatures follow the same trend as the measured values. However, the rate of change in temperature, at each level, is greatly over predicted for the entire simulation. The soil cools too rapidly during the night and warms too fast following sunrise. At 0100 hours, the near surface temperatures already deviate greatly from measurements. This is most likely due to the lack of a vegetation model to account for the effects of the grass surface cover. The grass acts to insulate the soil by providing a canopy layer of humid air that stores heat. This changes the effective surface temperature that would interact with the simulated

velocity, temperature and moisture fields through the similarity theory formulation given by equations 2.3-2.5 [41]. The larger difference in predicted near surface soil temperature explains the over predicted soil heat flux.

The friction velocities, u_*, from simulations with each of the BCs and from measurements are shown in Figure 4.7. The trend of the predicted friction velocity from both BCs matches the measured trend until the last hour, where the predicted value sharply increases and the measured friction velocity decreases. This is the same hour that the LSM sensible heat flux diverges from observations. During the first two hours of the simulation the friction velocity is over predicted, but from 0200-0800 hours the predicted values fall within the range of the measured spread. Friction velocity differences between the two BC methods are small and correlated to differences in the sensible heat flux, due to the dependence on the sensible heat flux through the stability correction. Discrepancies between observations and the models are due to the over simplified formulation of the friction velocity (equation 2.5) and the constant roughness (z_o) that fails to capture the complete physics. The GABLS3 roughness has been specified as a constant (0.15 m) that results in the correct average momentum flux for the CESAR. For the Cabauw site the local roughness (for short grass) is closer to 1-3 cm and the average effective roughness varies, between 0.01-0.20 m [14], based on wind speed and direction.

4.1.1 Boundary Layer Stability

As the night progresses and the surface cools, negatively buoyant forces strengthen and increasingly damp turbulent motions. As a result, the BL height decreases. The BL height (δ), computed by linearly extrapolating ($\delta = h_{0.90}/0.9$) from the height ($h_{0.90}$) where the shear stress is 10% of the surface stress [12, 51, 10], evolves as shown in Figure 4.8. The BL height decreases continuously from around 240 m to a minimum of about 100 m at 0530 hours from the nighttime stable conditions. The bulk stability is quantified by the nondimensional scaling parameter, $\zeta = \delta/L$, depicted in Figure 4.9. Before sunrise the bulk stability doesn't change significantly, remaining moderately stable with $\zeta \approx 5$ [43]. The LSM-LES net radiation begins heating the surface shortly after 0430 hours. It takes approximately 30 min for

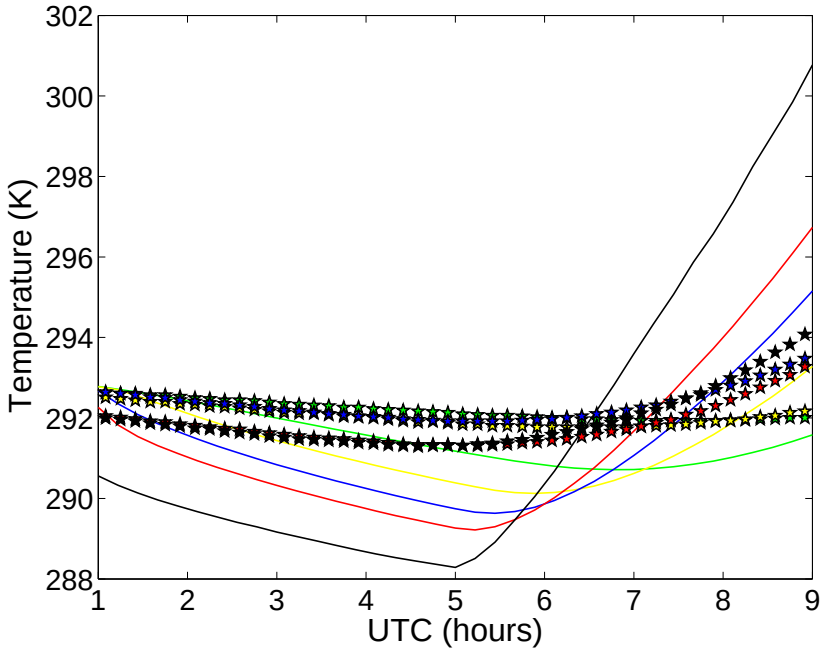

Figure 4.6. LSM predicted (-) and measured (stars) soil temperature time series at depths of 0 cm (black), 2 cm (red), 4 cm (blue), 8 cm (yellow), 12 cm (green).

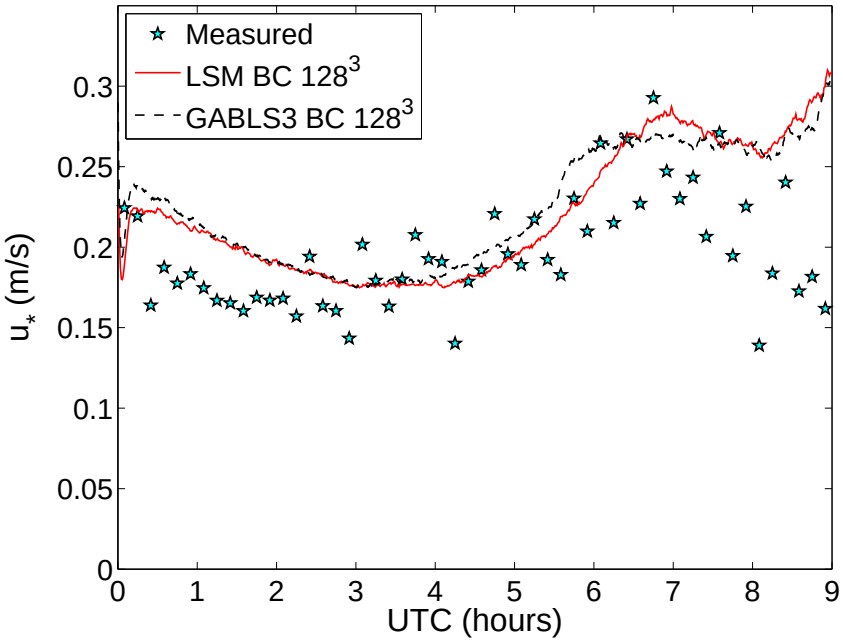

Figure 4.7. Friction velocity, u_* (m/s), from measurements and horizontally averaged predicted values from the LSM-LES, and GABLS3 LES for 2 July 2006.

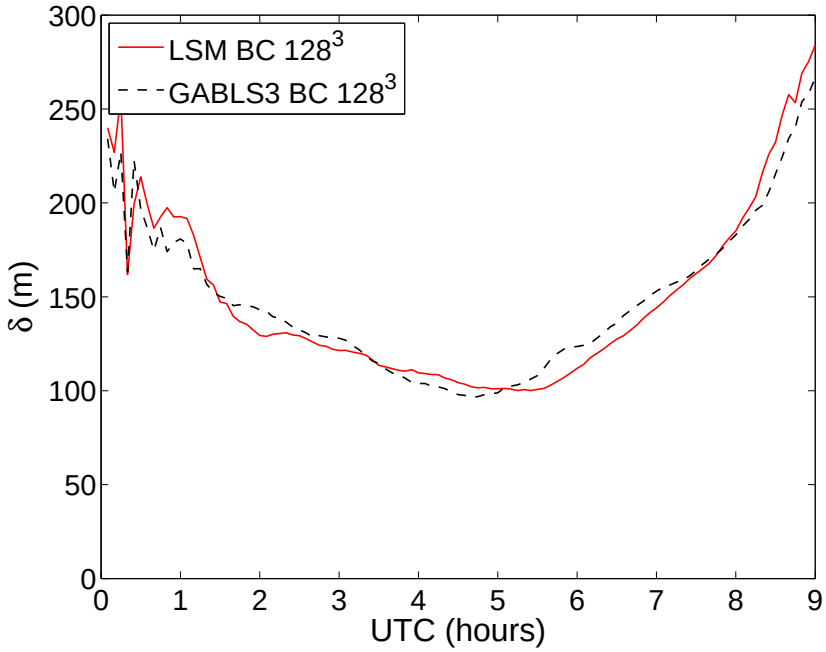

Figure 4.8. Temporal variation of the boundary layer height, δ (m), from the LSM-LES and GABLS3 LES.

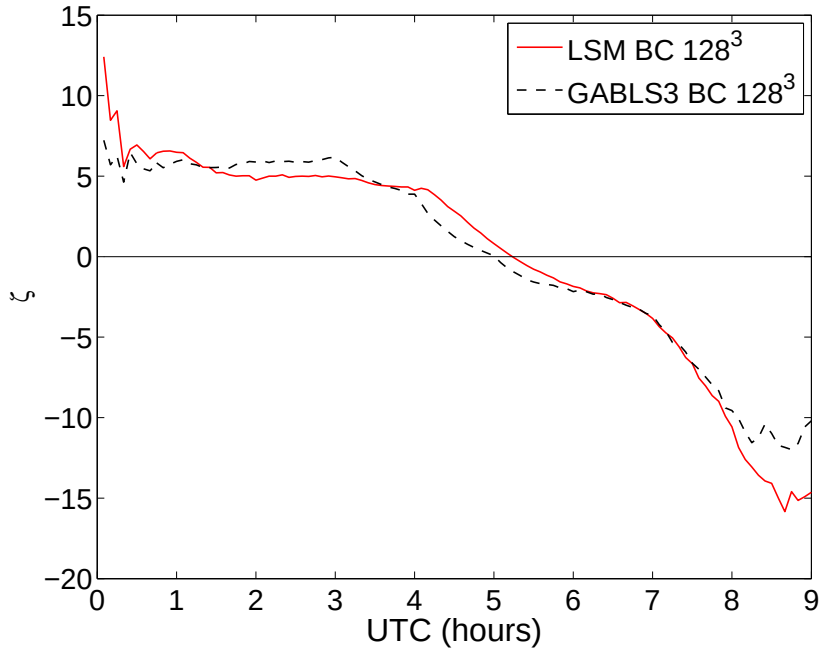

Figure 4.9. Temporal variation of the nondimensional bulk stability parameter, $\zeta = \delta/L$, from the LSM-LES and the GABLS3 LES.

the surface temperature to warm to the air temperature, causing the sensible heat flux to approach zero and the stability to approach neutral ($\zeta \approx 0$). During this time the BL continues to shrink. As the surface temperature surpasses the air temperature the sensible heat flux becomes positive and the BL transitions to unstable and convective. Growth of the BL due to increasing turbulence and positive buoyancy begins at around 0530 hours. This shows a delay of approximately 30 min in the propagation of the positive surface flux up to the BL height. For the remainder of the simulation, the convective BL continues to develop up to 275 m and become increasingly unstable as the surface is heated throughout the morning. The GABLS3 LES produces the same trends only the times and magnitudes are slightly different, corresponding to the differences in sensible heat flux.

4.2 Structure of the Atmospheric

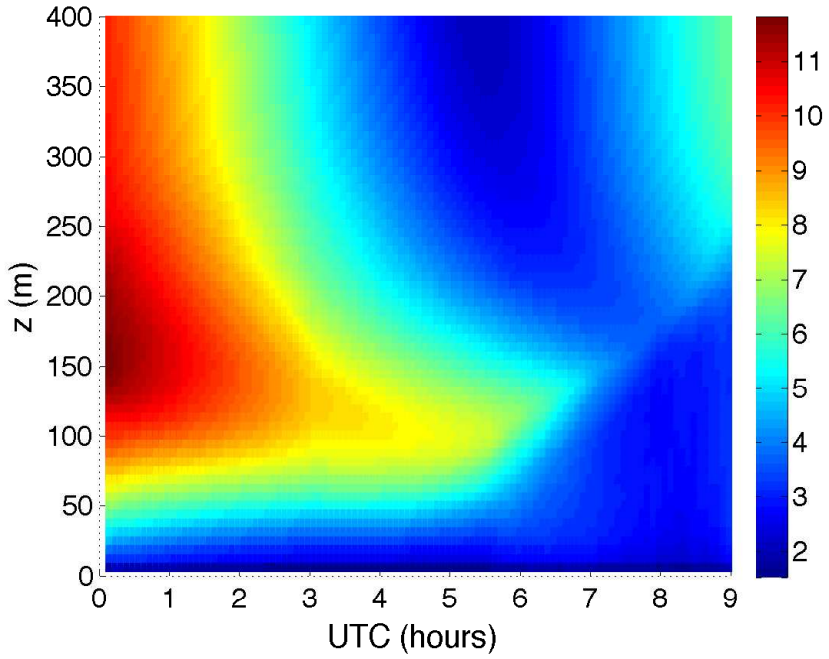

Figure 4.10. Resolved wind speed (horizontally averaged), $\tilde{U}$ (m/s), as a function of time and height from the LSM-LES results.

Boundary Layer

The surface fluxes interact with the atmosphere driving the mean flow and turbulent fluctuations. Figure 4.10 shows the horizontally averaged wind speed as a function of time and height from the LSM-LES. At time zero the wind speed is initialized based on measurements that include a low-level jet with supergeostrophic wind speed. The low-level jet becomes more pronounced as the simulation progresses, until 0500-0600 hours when it begins to erode. Surface heating leads to increased positive buoyancy and vertical turbulence causing increased momentum drag. This slows the flow and completely destroys the low-level jet by 0800 hours. The formation of a low-level jet in LES of the SBL has been observed in previous studies [51, 89, 88, 10, 12, 11]. A low-level jet can form from many possible causes, most of which are at scales much larger than the LES domain, including baroclinicity associated with sloping terrain and weather fronts [52]. The low-level jet in this simulation is due to inertial oscillations induced by the Coriolis force. As the stability increases and vertical turbulence is damped the friction between fluid layers is reduced. The flow becomes decoupled from the surface fluxes and accelerates to supergeostrophic speeds. If the stable conditions persist for long enough the flow would oscillate about the geostrophic value with a period of approximately 15.25 hours based on the Cabauw sites latitude and neglecting frictional damping [90]. The morning transition to a convective BL (CBL) occurs before oscillations are observed in the simulation.

Figures 4.11, 4.12, 4.13 and 4.14 show the u and v velocity components, respectively. The vertical profiles discussed in this section display results from the lowest 400 m of the domain that are averaged horizontally and over the last 10 min of each hour. Each plot contains profiles of the LSM-LES results, the GABLS3 results and measured tower observations at 2, 10, 20, 40, 80, 140, and 200 m. From inspection of the profiles, it can be seen that during the stable periods (until 0500 hours) the results from the LES with different BCs are essentially the same. The simulations capture the trend and shape of the low-level jet with a slight under prediction of the jets magnitude. In the lowest 50 m, there is an acceleration after 0200 hours that is not captured by the simulations. This results in wind speeds

lower than the observations. At 0650-0700 hours a shallow unstable internal BL is clearly developing. However, it does not evolve rapidly enough to match the observed BL height at 0750-0800 hours, at which time the measured velocities are well mixed up to 200 m. The trend of each velocity component matches observations well, except the last 3 hours when the v velocity magnitude is under predicted by 1 m/s. By 0850-0900 hours the u velocity component is over predicted. The GABLS3 BC provides the same over prediction, even though the sensible heat flux matches measurements well, during the last hour. This indicates that the incorrect u velocity may not be a result of the surface BC, but a result of an incorrect large scale advection input [6]. This also explains the divergence of the friction velocity from observations during the last hour. The largest difference between surface BC velocity predictions occurs at 0550-0600 hours, due to the faster transition of the GABLS3 BC sensible heat flux from 0400-0600 hours. Thus, earlier development of convective conditions results in an earlier erosion of the low-level jet and a slower velocity. Although the LSM more accurately predicts the sensible heat flux during this period, the GABLS3 BC better matches the velocity.

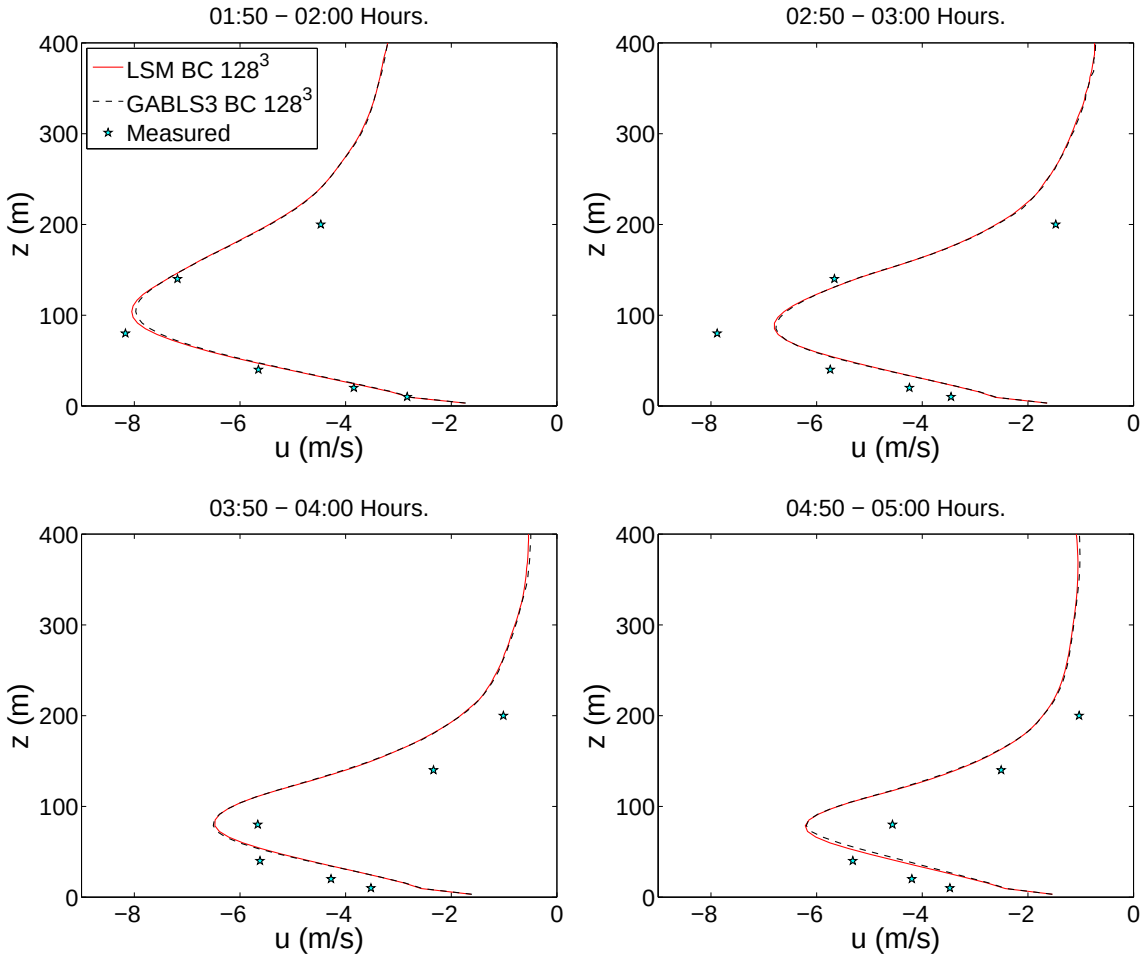

Figure 4.11. Resolved velocity profiles of $\tilde{u}$ (m/s) averaged over last 10 minutes of each hour from 0100-0500 hours, showing LSM-LES, GABLS3 LES and measurements.

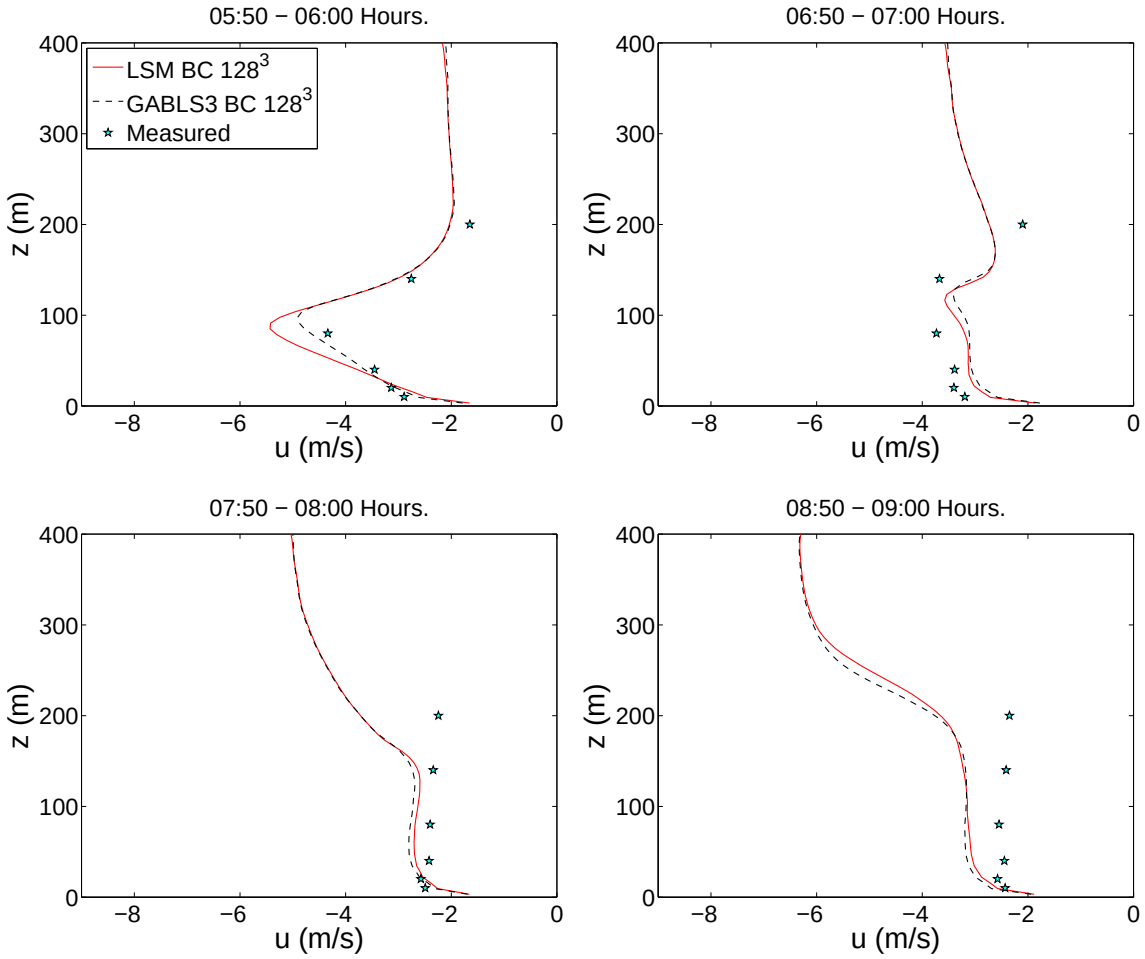

Figure 4.12. Resolved velocity profiles of $\tilde{u}$ (m/s) averaged over last 10 minutes of each hour from 0500-0900 hours, showing LSM-LES, GABLS3 LES and measurements.

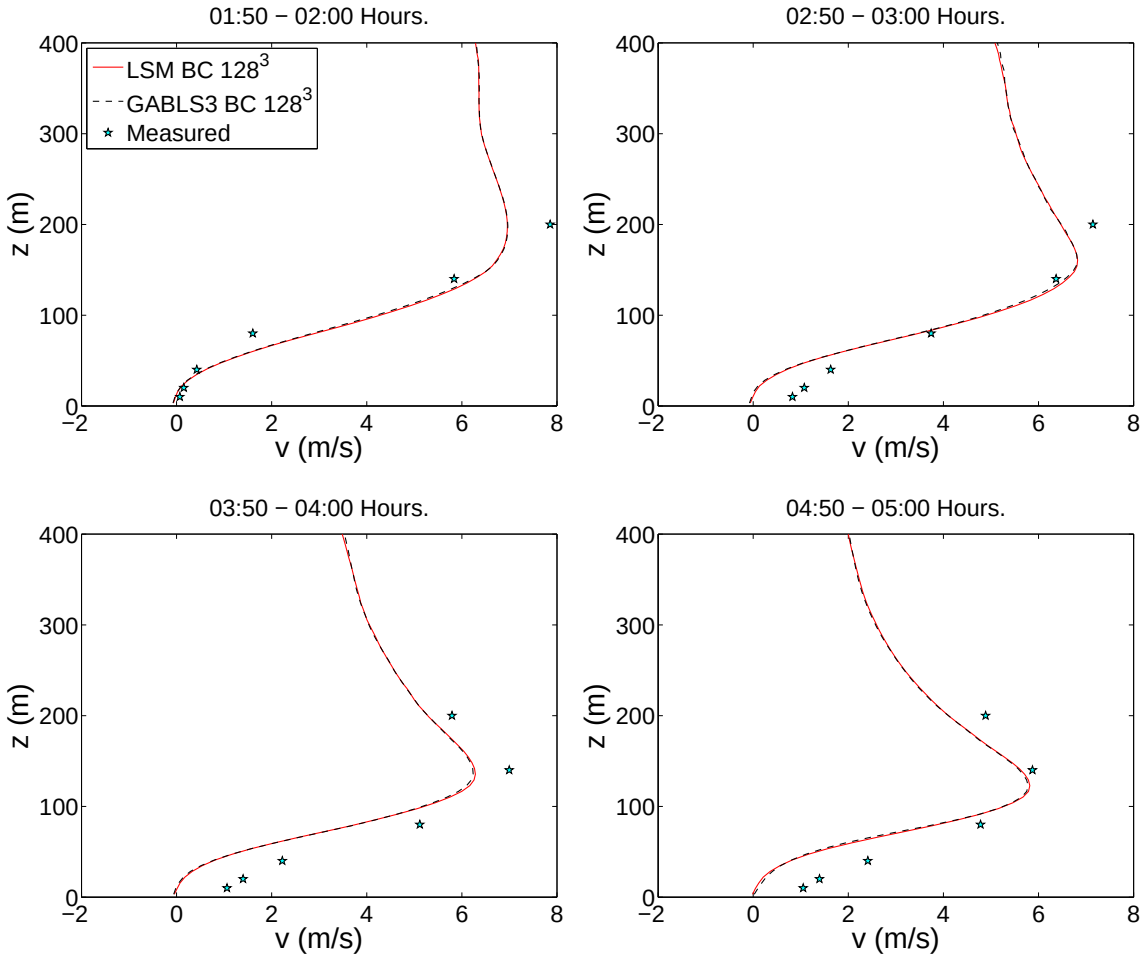

Figure 4.13. Resolved velocity profiles of $\tilde{v}$ (m/s) averaged over last 10 minutes of each hour from 0100-0500 hours, showing LSM-LES, GABLS3 LES and measurements.

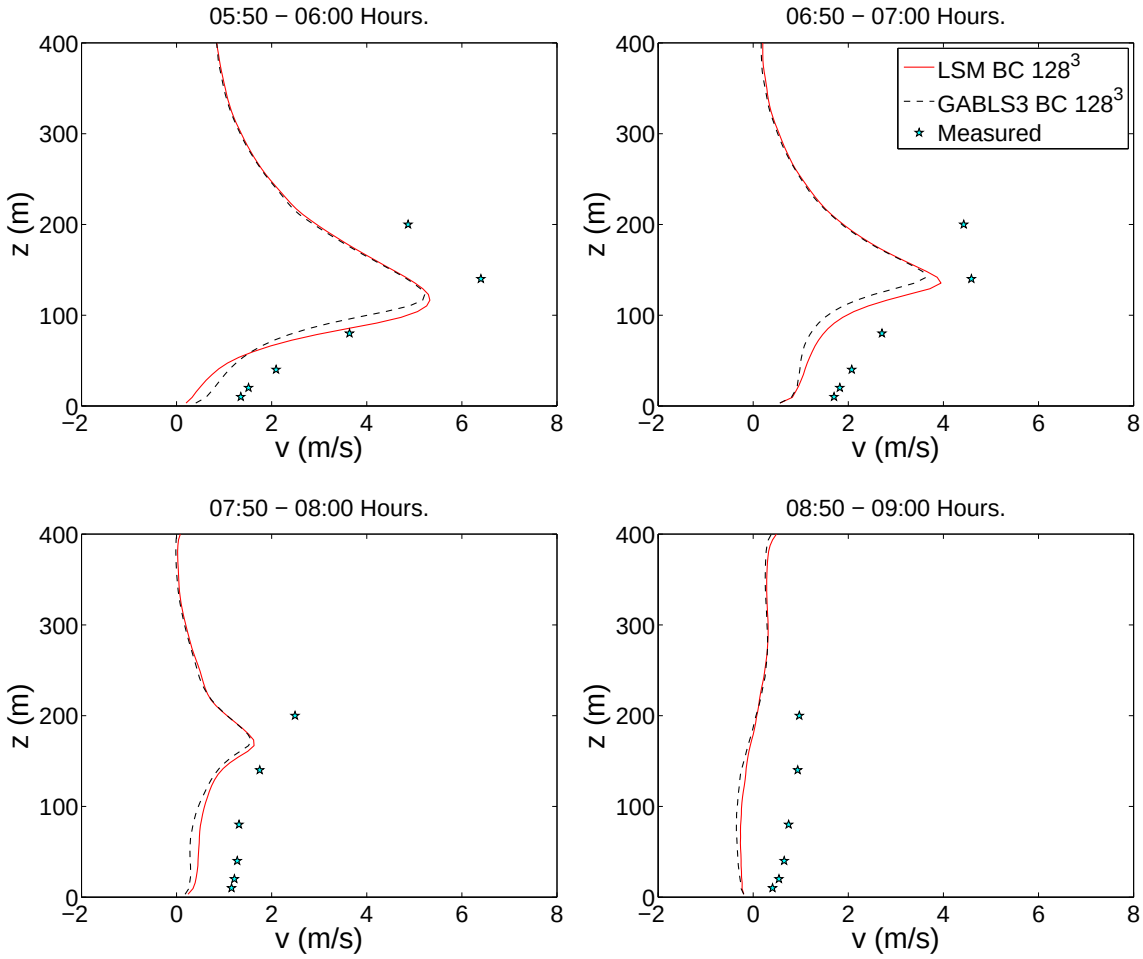

Figure 4.14. Resolved velocity profiles of $\tilde{v}$ (m/s) averaged over last 10 minutes of each hour from 0500-0900 hours, showing LSM-LES, GABLS3 LES and measurements.

Potential temperature and specific humidity from the LSM-LES are shown in Figures 4.15 and 4.16 respectively, as functions of time and height (up to 400 m). Significantly above the BL (250-300 m) a residual layer is apparent from the well mixed state of the scalars. The ABL cools as the surface cools from the start of the simulation to 0530 hours. This corresponds to the period with negative sensible heat flux in Figure 4.2. The increased stratification is displayed by the compression of the temperature layers, up until 0600 hours. Afterward, formation of the unstable CBL is depicted by the well mixed region between the surface and the BL top. The temperature and humidity rapidly increase due to the large positive surface fluxes induced by radiative surface heating.

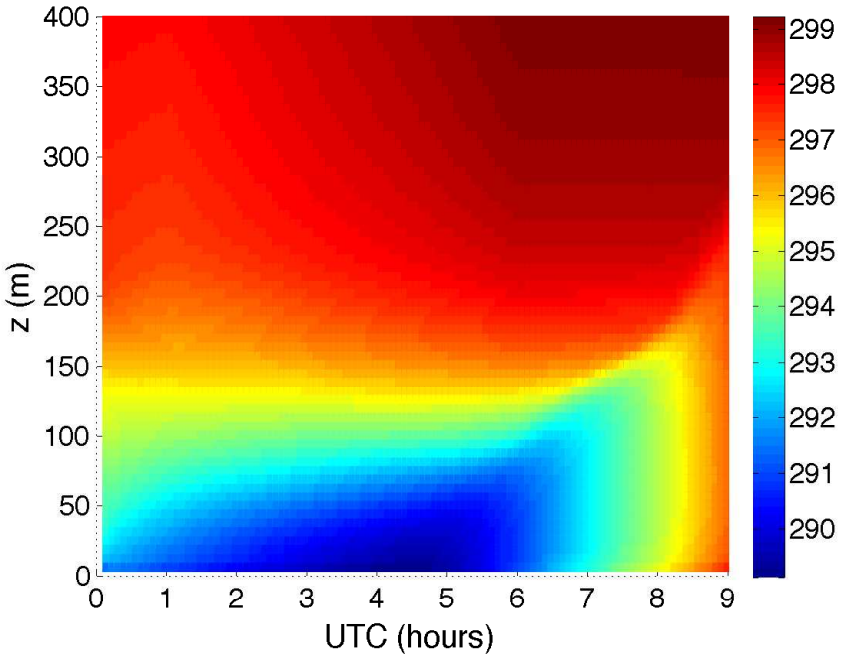

Figure 4.15. Horizontally averaged potential temperature, $\tilde{\theta}$ (K), as a function of time and height (up to 400 m) from the LSM-LES results

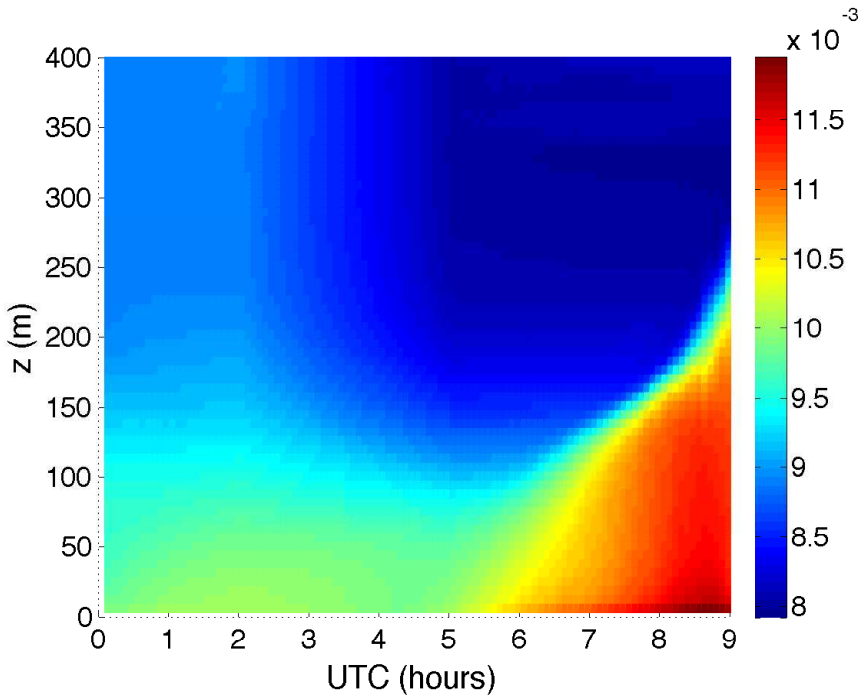

Figure 4.16. Horizontally averaged specific humidity, $\tilde{q}$ (kg/kg), as a function of time and height (up to 400 m) from the LSM-LES results

Figures 4.17, 4.18, 4.19 and 4.20 show profiles of potential temperature and specific humidity, respectively, with measured values at 2, 10, 20, 40, 80, 140, and 200 m. The general trends of the scalars agree with the measurements. Prior to 0400 hours the temperature profiles between the two LESs only differ slightly. During the stable period, differences from the BCs are more apparent in the humidity profiles. The LSM predicts a higher humidity in the lower BL prior to 0400 hours, due to the higher evaporation during the first 2 hours. By 0450-0500 hours, the GABLS3 BL is more humid than the LSM due to higher evaporation rates during the previous 3 hours. At later times, the difference in ABL humidity between BC methods is

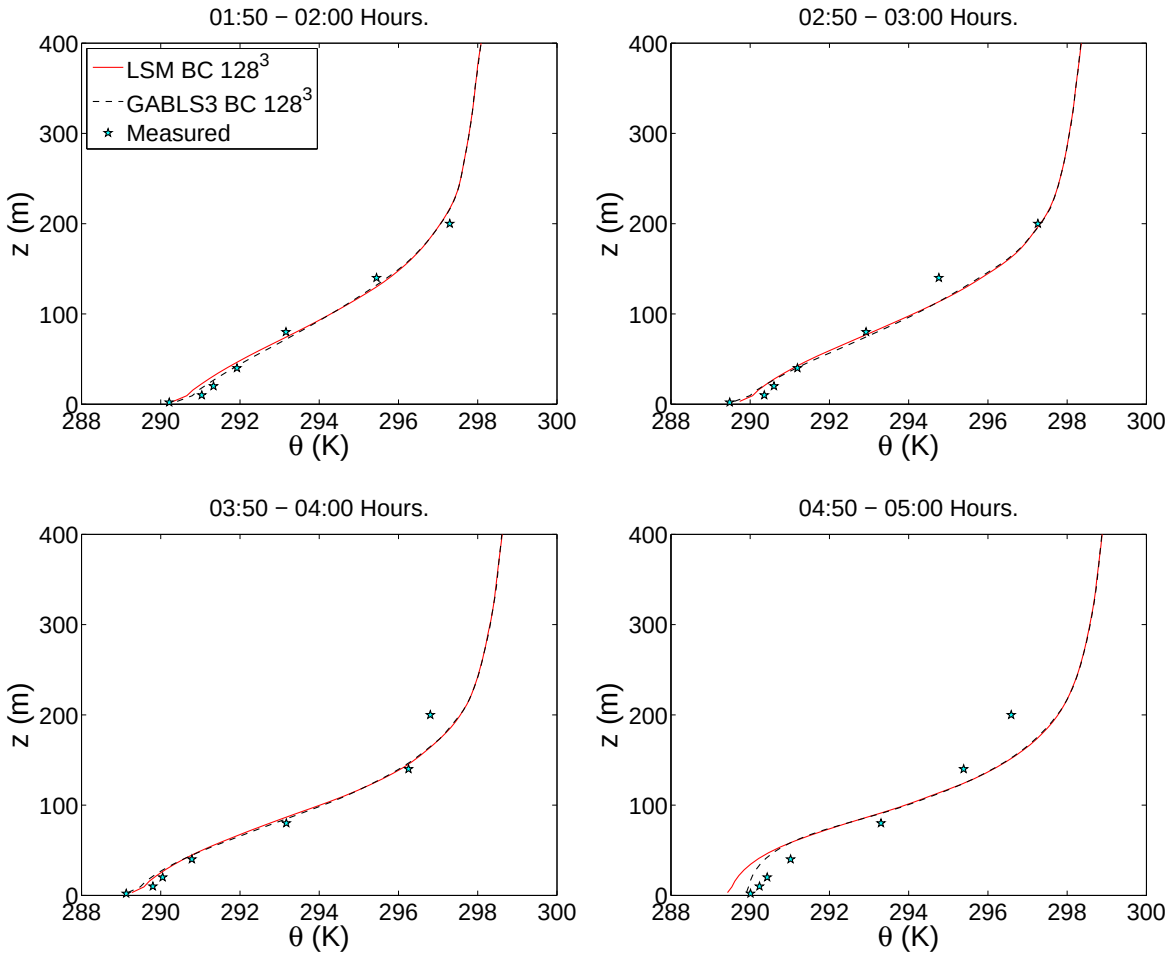

Figure 4.17. Resolved potential temperature, $\tilde{\theta}$ (K), profiles averaged over last 10 minutes of each hour from 0100-0500 hours, showing LSM-LES, GABLS3 LES and measurements.

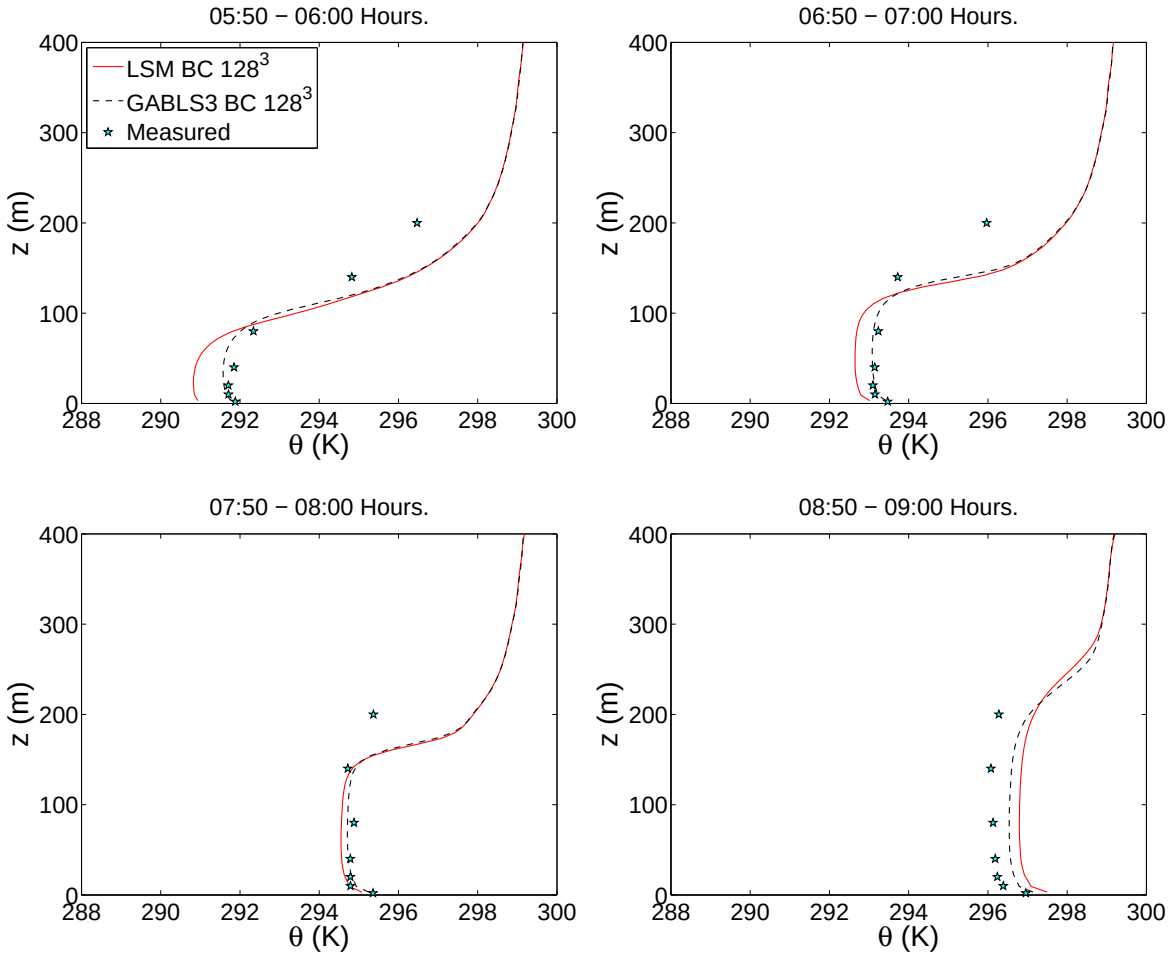

Figure 4.18. Resolved potential temperature, $\tilde{\theta}$ (K), profiles averaged over last 10 minutes of each hour from 0500-0900 hours, showing LSM-LES, GABLS3 LES and measurements.

also correlated to the history of the predicted evaporation. For example, the LSM predicts a more humid ABL at 0650-0700 hours due to a higher evaporation rate from 0600-0700 hours. The potential temperature profiles can be correlated to the sensible heat flux in the same manner. At 0750-0800 hours, the temperature and humidity also suggest that the BL height is not evolving as fast as indicated by the tower data, similar to the velocity profiles.

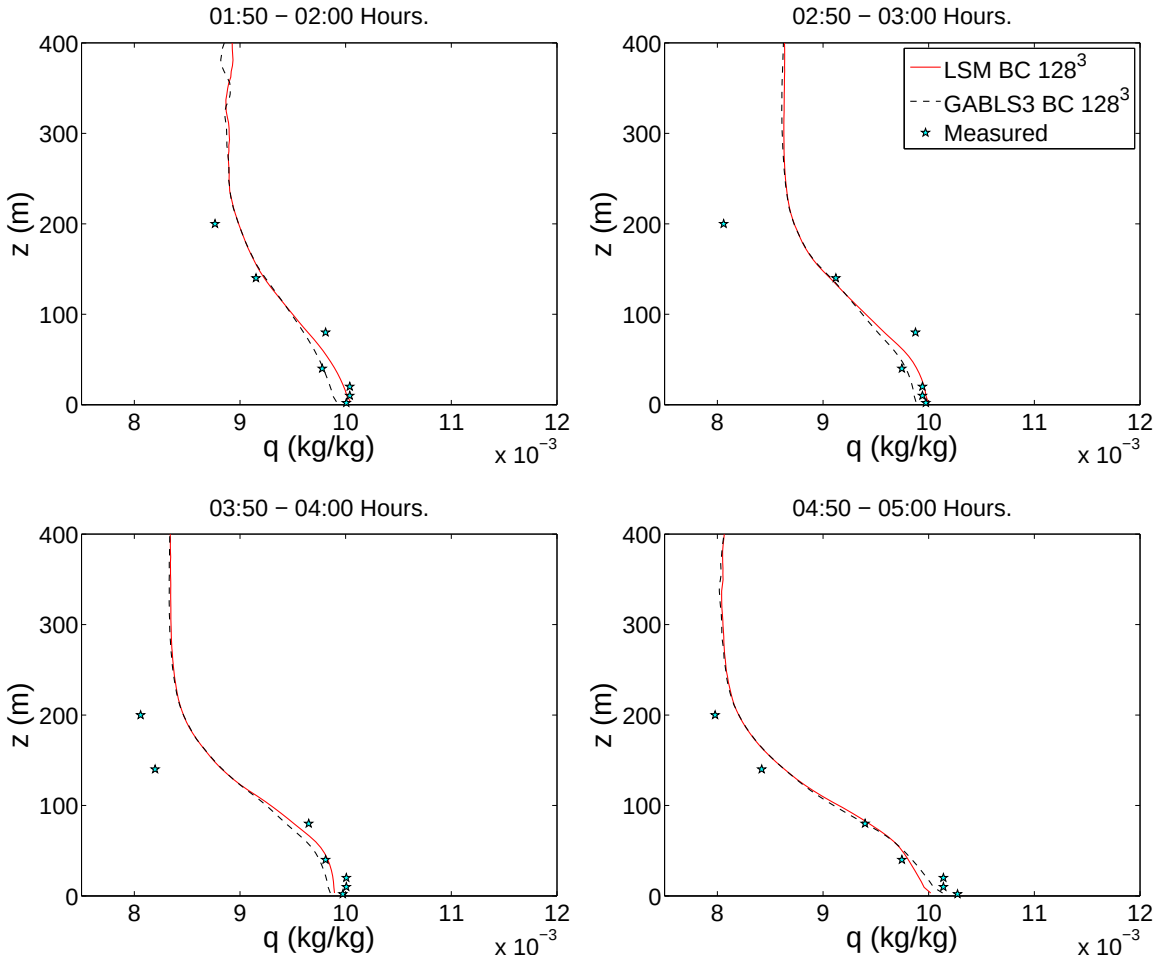

Figure 4.19. Resolved specific humidity, $\tilde{q}$ (kg/kg), averaged over last 10 minutes of each hour from 0100-0500 hours, showing LSM-LES, GABLS3 LES and measurements.

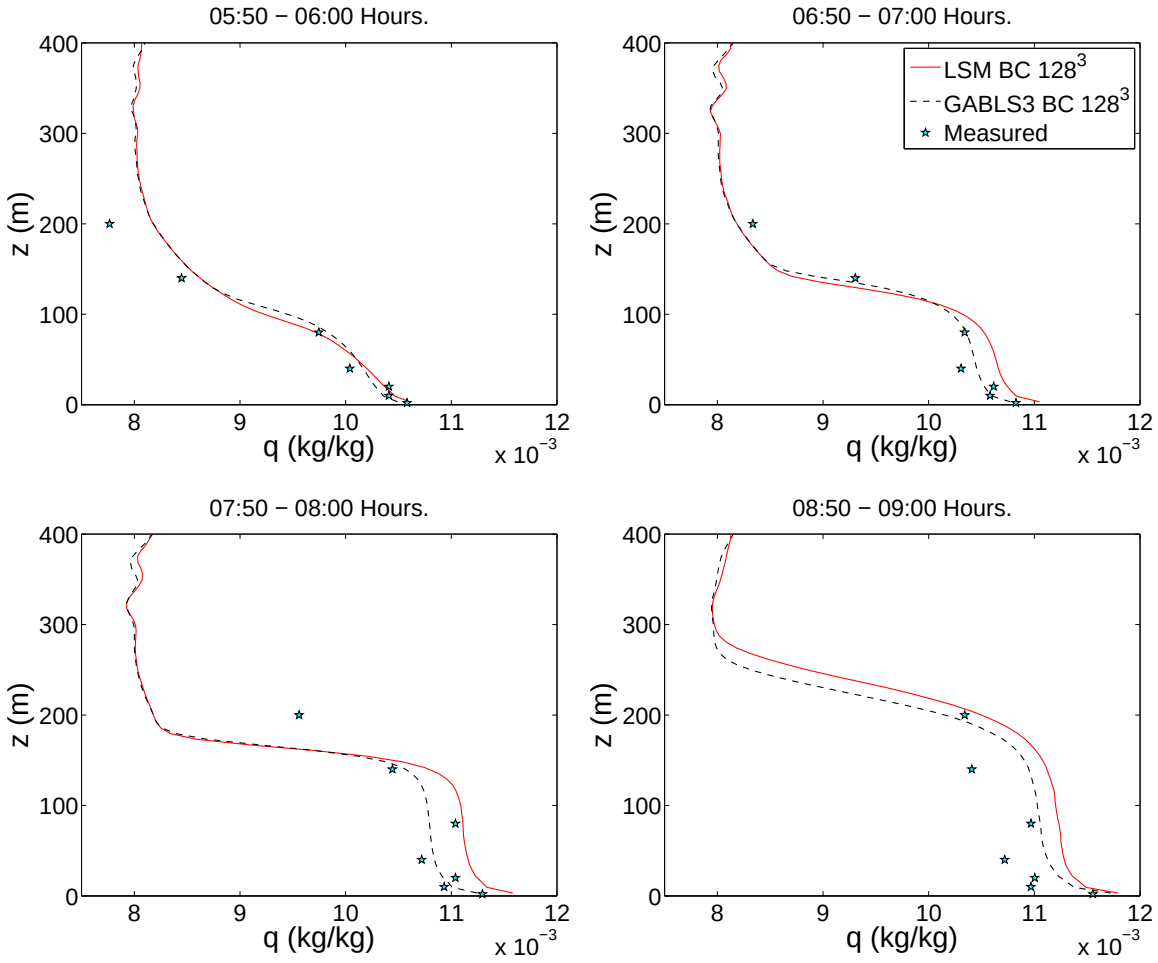

Figure 4.20. Resolved specific humidity, $\tilde{q}$ (kg/kg), averaged over last 10 minutes of each hour from 0500-0900 hours, showing LSM-LES, GABLS3 LES and measurements.

Profiles of momentum flux and potential temperature flux are shown in Figures 4.21, 4.22, 4.23 and 4.24, respectively. The fluxes at the surface are proportional to those in Figures 4.2 and 4.7 and therefore, follow the same temporal trend. After 0450 hours, the CBL exhibits a linear potential temperature flux with height and an overshoot region near the top of the BL due to entrainment of the mixed layer. Each of these features are commonly observed in the convective BL (e.g. [11, 71]). As the CBL grows the SGS component of both the momentum flux and temperature flux becomes a smaller contribution to the total flux, due to a larger portion of the energy being resolved in the positively buoyant motions. The SGS flux component is much more significant during the stably stratified period before 0530 hours.

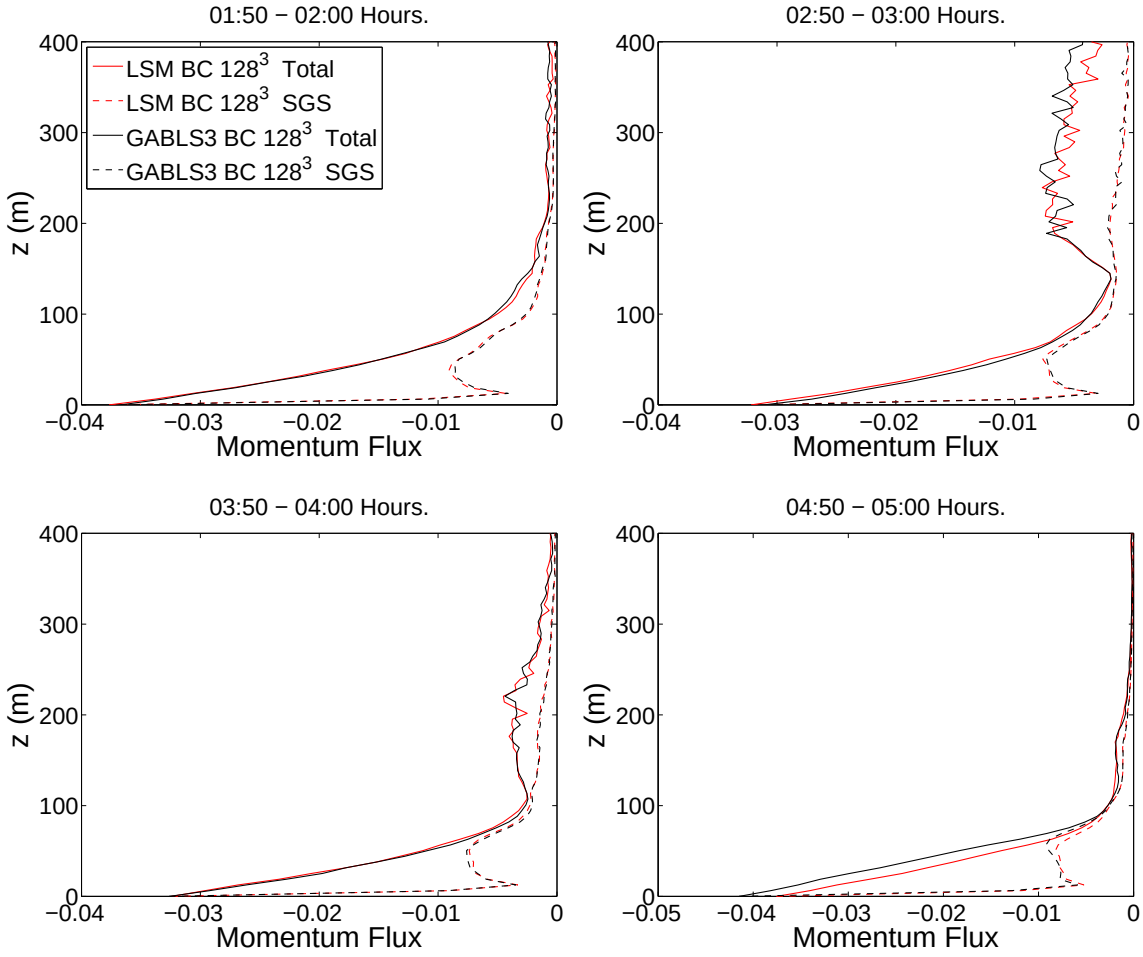

Figure 4.21. Profiles of SGS and total momentum stress averaged over the last 10 minutes of each hour from 0100-0500 hours, for the LSM-LES and GABLS3 LES results.

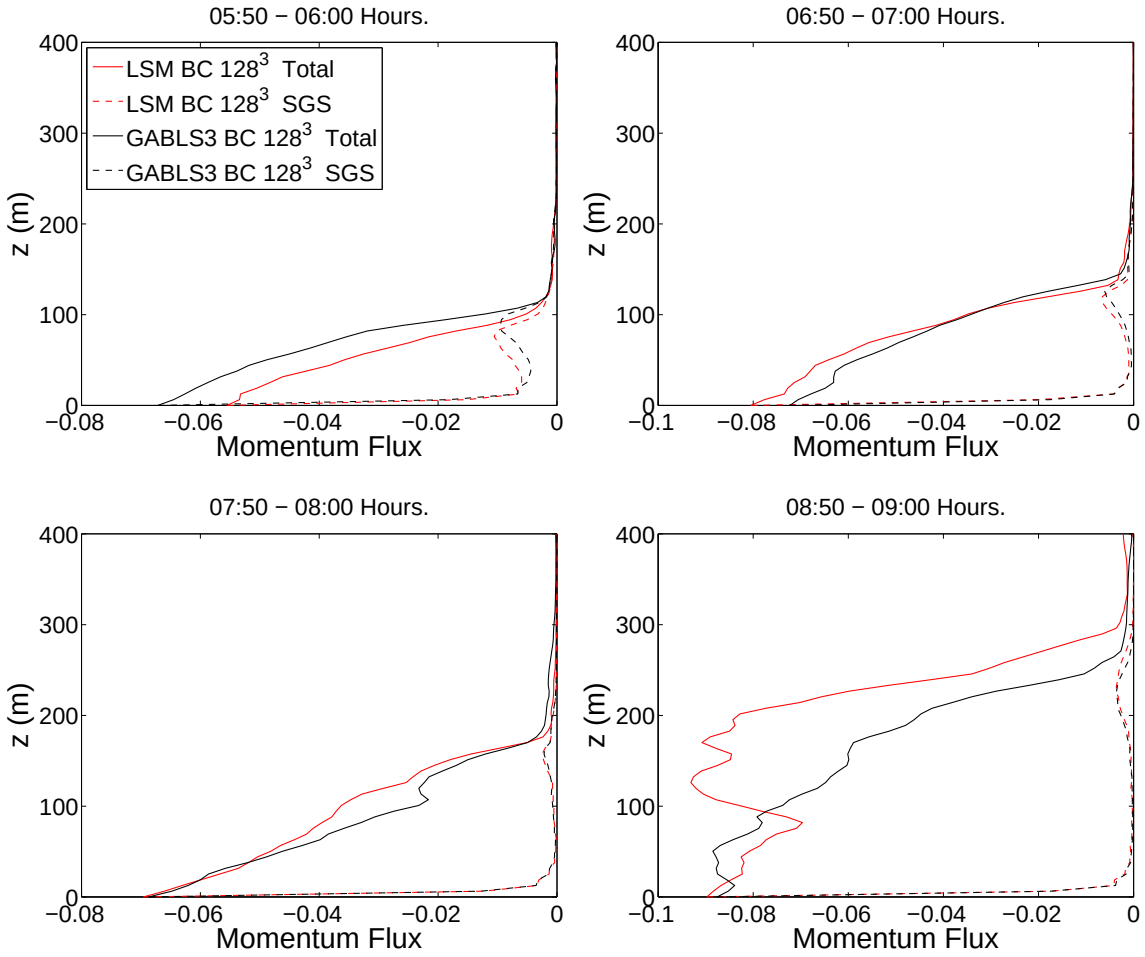

Figure 4.22. Profiles of SGS and total momentum stress averaged over the last 10 minutes of each hour from 0500-0900 hours, for the LSM-LES and GABLS3 LES results.

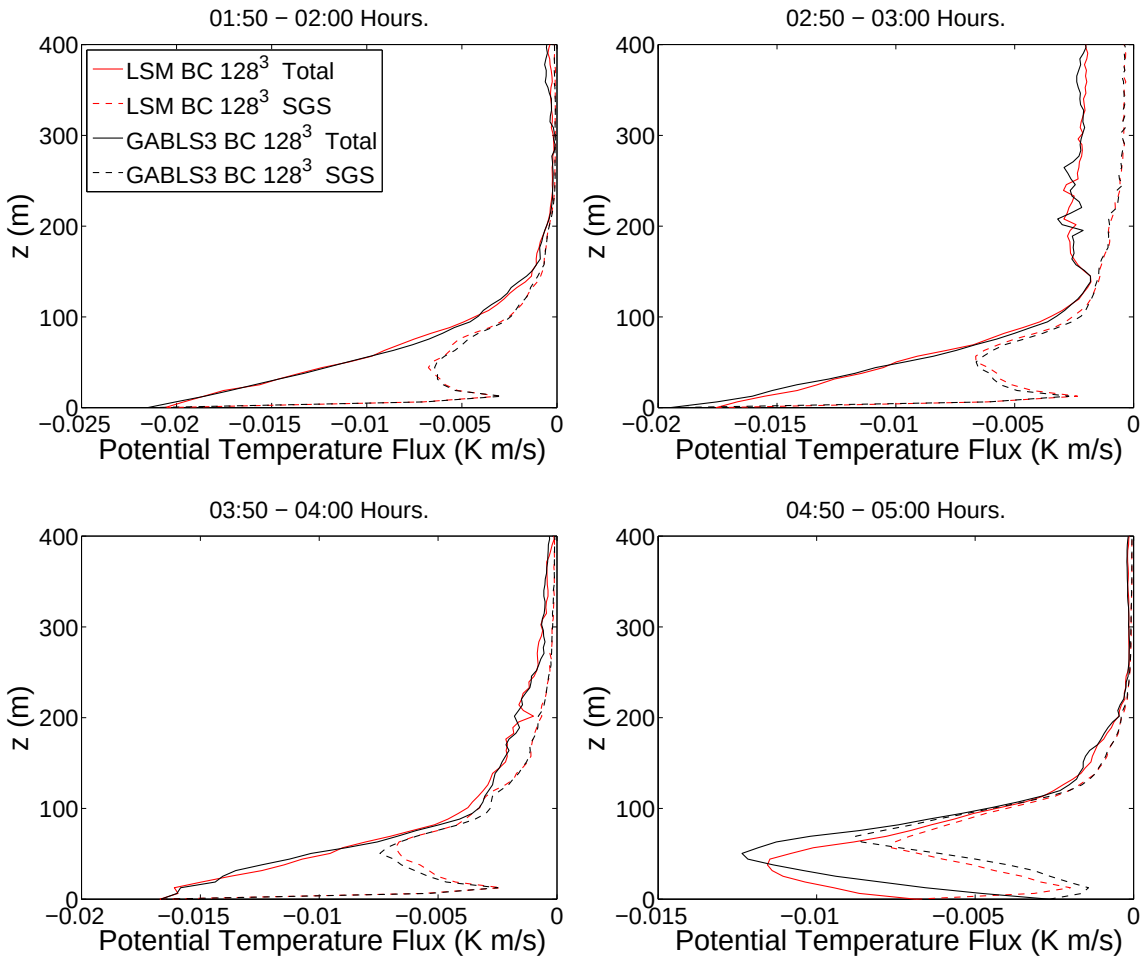

Figure 4.23. Potential temperature flux averaged over last 10 minutes of each hour from 0100-0500 hours, showing the LSM-LES and GABLS3 LES results.

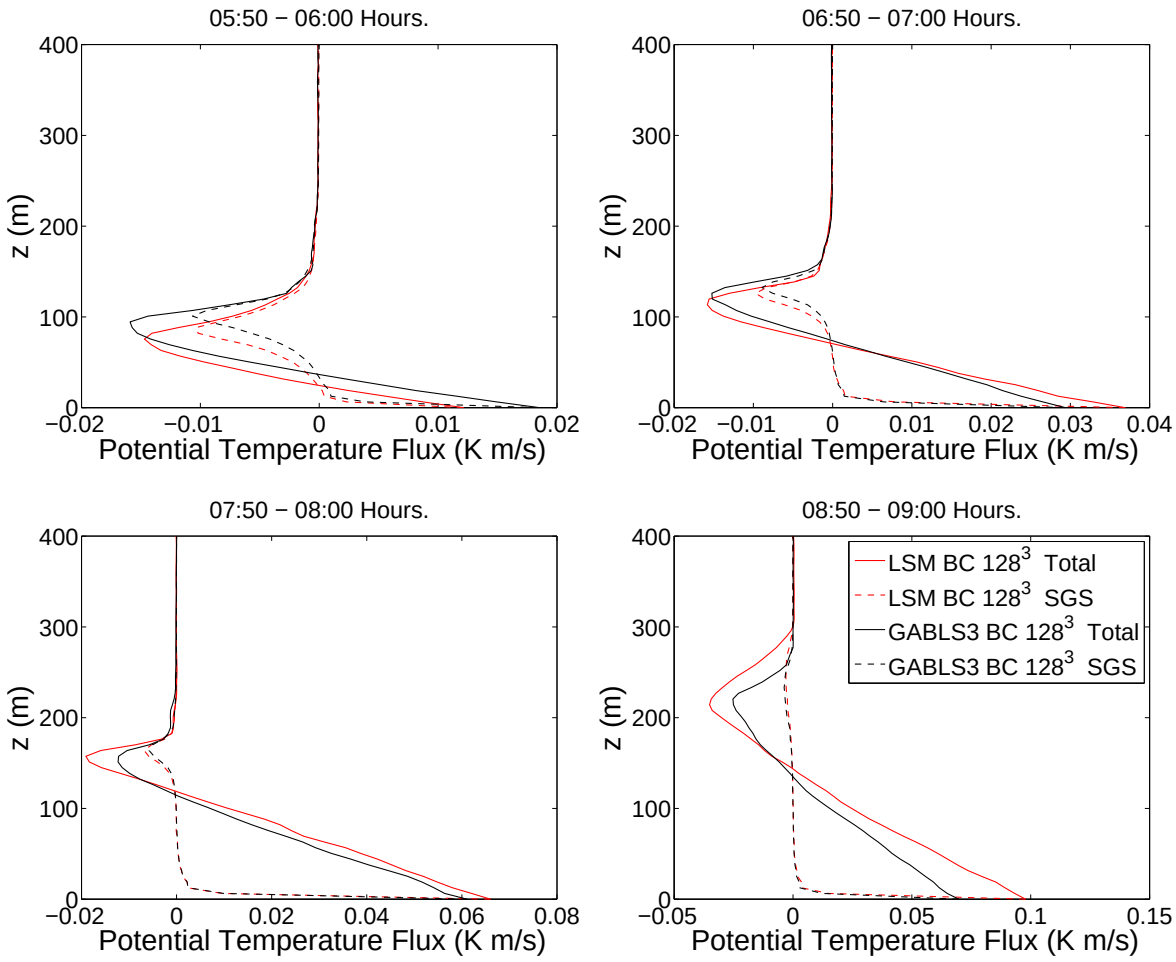

Figure 4.24. Potential temperature flux averaged over last 10 minutes of each hour from 0500-0900 hours, showing the LSM-LES and GABLS3 LES results.

By assuming a stationary, 1-dimensional SBL, Nieuwstadt [69] derived a linear form for the potential temperature flux profile when normalized by its surface value, as (1 - z/δ). Similarly, the normalized stress was derived to take the form (1 - $z/\delta)^{3/2}$. Profiles of the normalized momentum flux and potential temperature flux are displayed in Figures 4.25 and 4.26, respectively. Beare et al. [12], Basu and Porté-Agel [10], and Stoll and Porté-Agel [88] all produced LES results that matched the theory well for stationary simulations. The current non-stationary LES results compare well with the theory of Nieuwstadt, agreeing with the non-stationary results of Basu et al. [11] that local scaling may be applicable beyond the idealized stationary SBL. The deviation of temperature flux from theory near $z/\delta = 1$ can be attributed to the definition of δ based on the momentum flux rather than the temperature flux [88, 9]. The LSM-LES normalized momentum flux compares better to theory than the GABLS3 LES results.

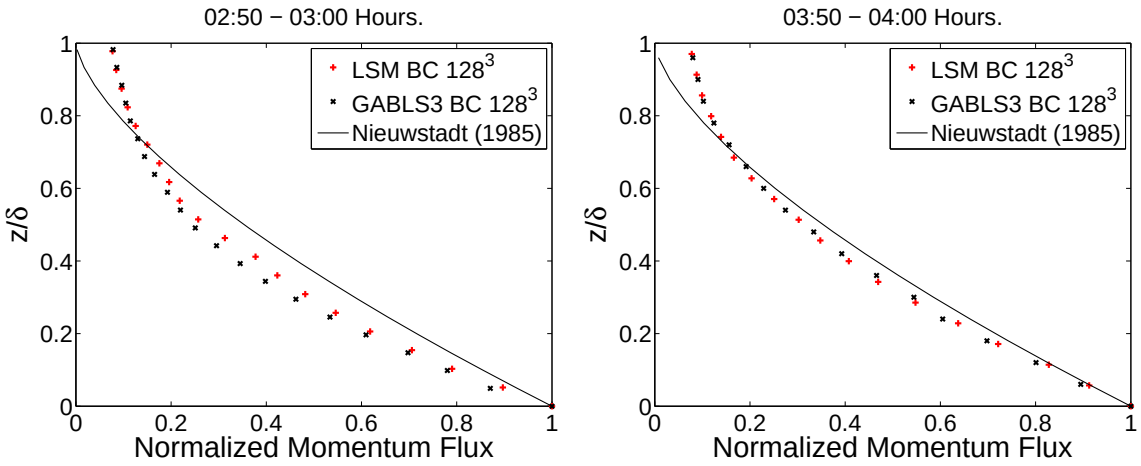

Figure 4.25. Normalized momentum flux profiles from the last 10 min of two stable periods for the LSM-LES and GABLS3 LES results.

The BC and land-atmosphere coupling is expected to have the most direct impact on the surface layer. In SBL simulations, it is common [9, 88, 51] to evaluate surface layer results by comparing the nondimensional shear, given by

$$\Phi_M = \left(\frac{\kappa z}{u_*}\right)\sqrt{\left(\frac{\partial u}{\partial z}\right)^2 + \left(\frac{\partial v}{\partial z}\right)^2} \tag{4.1}$$

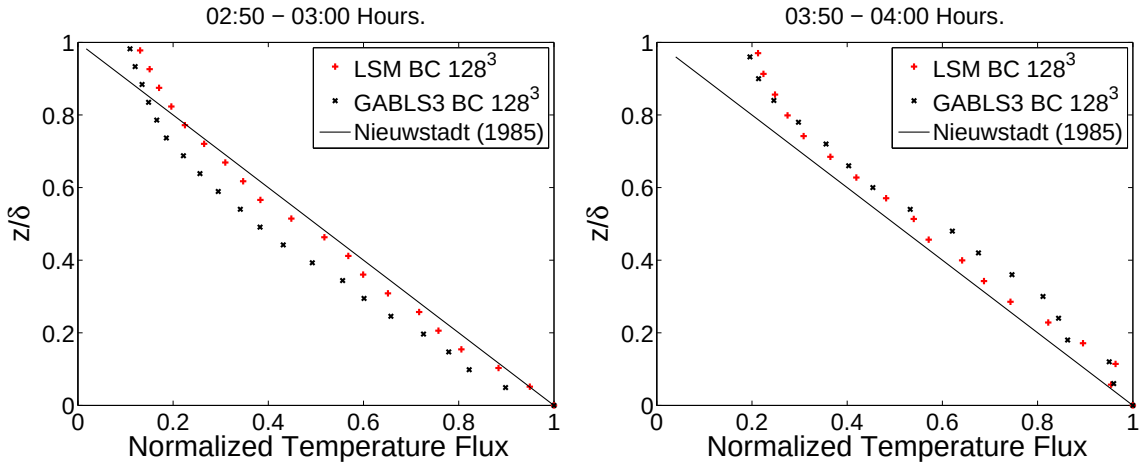

Figure 4.26. Normalized temperature flux profiles from the last 10 min of two stable periods for the LSM-LES and GABLS3 LES results.

and the nondimensional potential temperature gradient

$$\Phi_H = \left(\frac{\kappa z}{\theta_*}\right)\frac{\partial \theta}{\partial z} \tag{4.2}$$

to empirical formulations. From experimental data within the SBL surface layer Businger et al. [27] fit coefficients to a theoretical linear function of z/L as:

$$\Phi_M = 1 + 4.7\frac{z}{L} \tag{4.3}$$

and

$$\Phi_H = 0.74 + 4.7\frac{z}{L}. \tag{4.4}$$

Alternatively, Beljaars and Holtslag [14] developed a nonlinear formulation for the normalized shear and temperature gradients based on data from the Cabauw site given by

$$\Phi_M = 1 + \frac{z}{L}\left[a + be^{-d\frac{z}{L}}\left(1 + c - d\frac{z}{L}\right)\right] \tag{4.5}$$

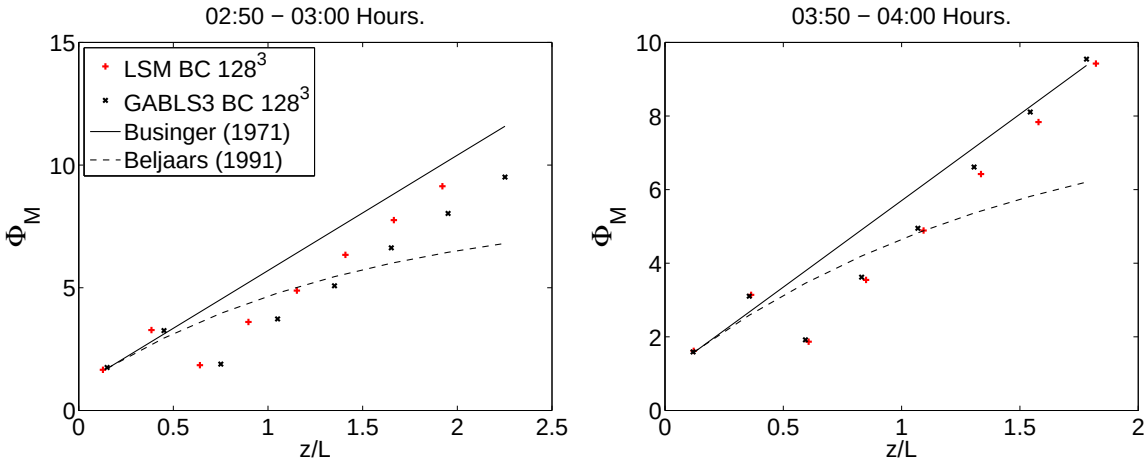

Figure 4.27. Nondimensional shear as a function of z/L in the lowest 50 m of the domain for two stable periods and compared to theory [27, 14].

and

$$\Phi_H = 1 + \frac{z}{L}\left[a\left(1 + \frac{3}{2}\frac{az}{L}\right)^{1/2} + be^{-d\frac{z}{L}}\left(1 + c - d\frac{z}{L}\right)\right], \tag{4.6}$$

where $a = 1$, $b = 2/3$, $c = 5$, and $d = 0.35$. The lowest 50 m of LES results at 0300 and 0400 hours, along with the two empirical formulations of Φ_M and Φ_H are plotted in Figures 4.27 and 4.28, respectively. Besides the first two levels, the slopes at 0300 hours agree well with the Businger et al. formulation, although there is an offset in the surface intersection. Stoll and Porté-Agel [88] also found a deviation in the trend above the lowest levels. The lowest level is forced to fit the empirical formulation by the similarity theory BC (equation 2.3 and 2.5). The nondimensional shear and temperature gradients at 0400 hours results in larger slopes than the empirical formulation. The LES results of Basu and Porté-Agel [9] showed similar trends that disagreed with the empirical slope. The important aspect of the nondimensional shear and temperature gradients is that the linear trend agrees with the empirical formulation.

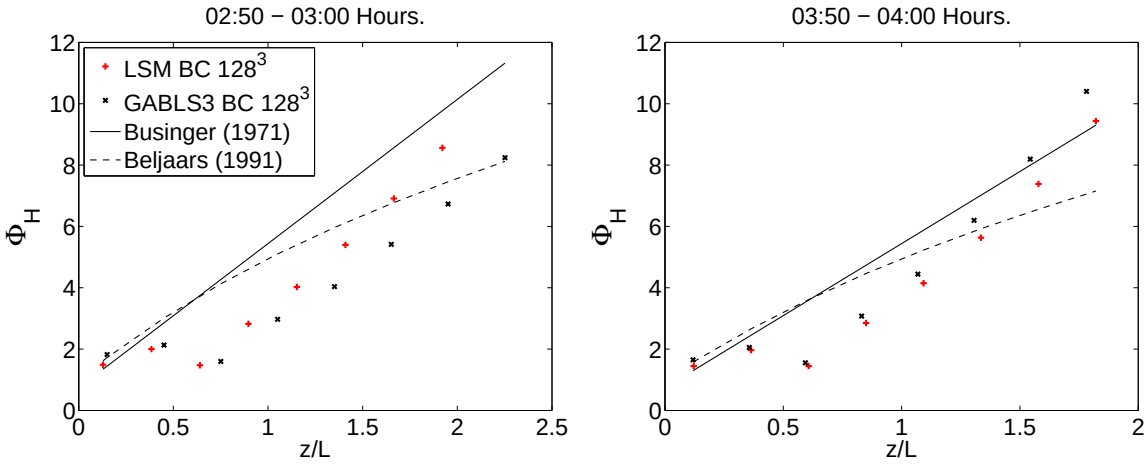

Figure 4.28. Nondimensional temperature gradient as a function of z/L in the lowest 50 m of the domain for two stable periods and compared to theory [27, 14].

4.3 Variance Statistics

Turbulence is suppressed during periods of atmospheric stability which can lead to gravity waves dominating the unsteady motions. However, for gravity waves to occur there frequency must be less than the Brunt-V*äisälä* frequency, N_{BV}, for a given height [90], where

$$N_{BV}^2 = \frac{g}{\theta_v}\frac{\partial \overline{\theta_v}}{\partial z}. \tag{4.7}$$

The maximum Brunt-V*äisälä* frequency throughout the simulation is 0.025 s^{-1}. This translates to a wave period of 1750 m, which would not be resolved within the simulation domain of 800 m. Since this LES case cannot resolve the possible gravity waves, all of the resolved variance must be due to turbulence.

Figures 4.29 and 4.30 show the u and v resolved variance, respectively, as a function of height and time. The resolved variance of the potential temperature as a function of time and height from the LSM-LES case is shown in Figure 4.31. For a given height within the BL, the variance of each variable decreases as the simulation progresses during the stable period (0000-0500 hours). This is a result of the suppression of turbulent motions by negative buoyancy. The evolution of the BL top

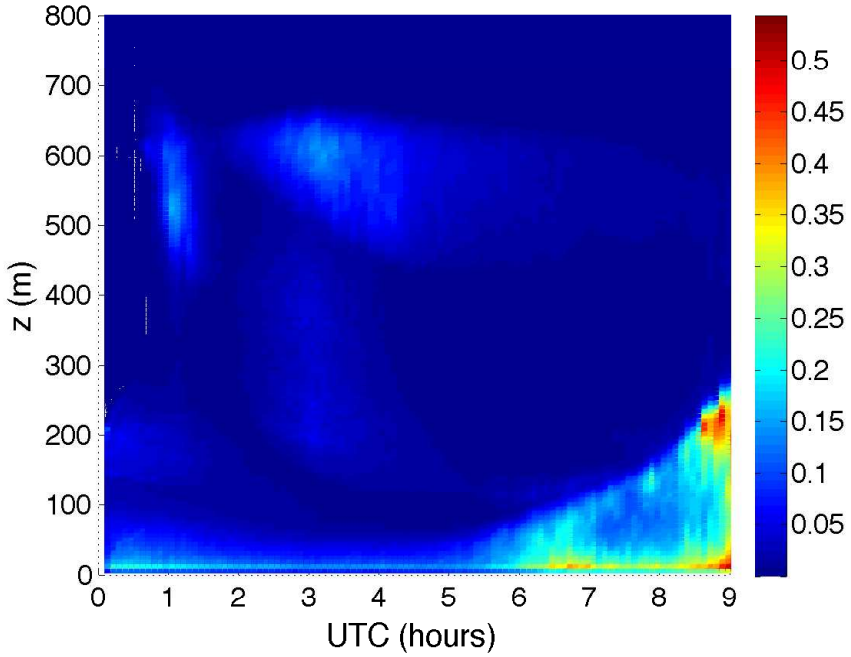

Figure 4.29. Horizontally averaged resolved $\tilde{u}$ variance, $\sigma^2_{\tilde{u}}$ (m^2/s^2), as a function of time and height from the LSM-LES results.

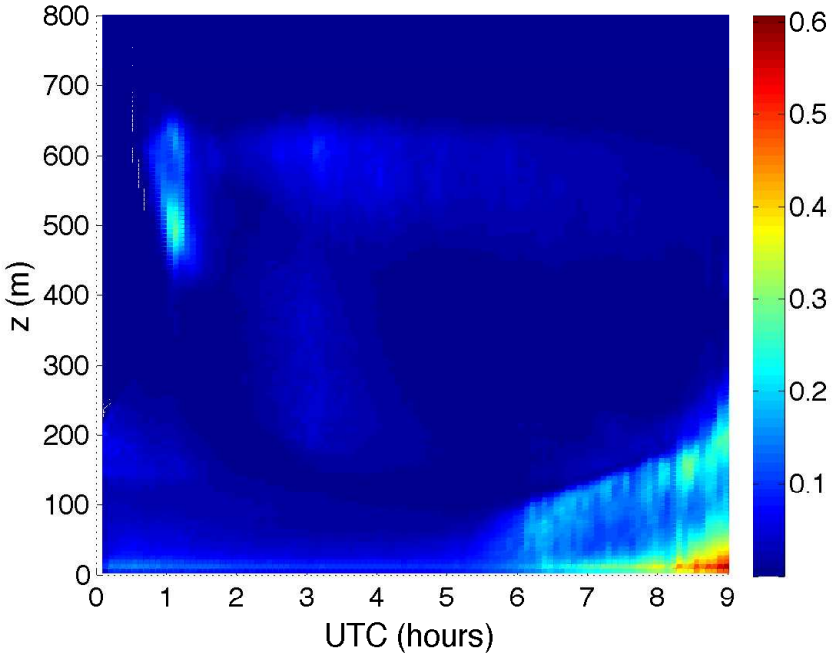

Figure 4.30. Horizontally averaged resolved $\tilde{v}$ variance, $\sigma^2_{\tilde{v}}$ (m^2/s^2), as a function of time and height from the LSM-LES results.

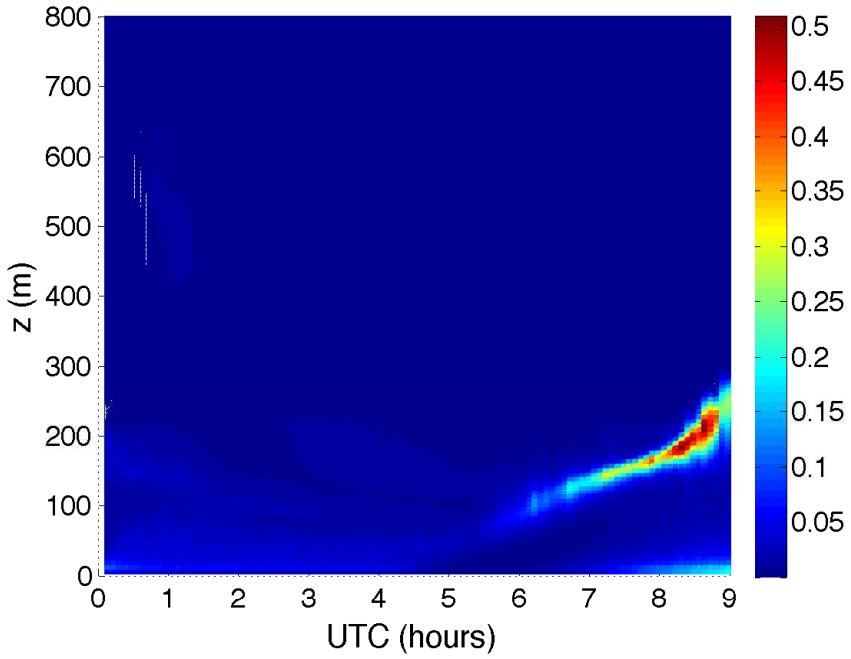

Figure 4.31. Horizontally averaged resolved potential temperature variance, $\sigma^2_{\tilde{\theta}}$ (K^2), as a function of time and height from the LSM-LES results.

can be seen by the sharp drop in turbulence as the height increases away from the surface. After 0500 hours the sensible heat flux becomes increasingly positive with time, causing the turbulence near the surface to increase from positively buoyant fluid parcels rising away from the surface. As the surface temperature continuously increases the parcels of air near the surface store more potential energy, enabling a parcel to rise to new heights. The parcel breaks through the previous CBL cap, entraining warmer air from the residual layer and increasing the BL height. The BL growth is depicted in the region of high velocity variance increasing in height from 0500-0900 hours.

Profiles of the average resolved variance of the u velocity, v velocity and potential temperature are shown in Figures 4.32, 4.33, 4.34, 4.35, 4.36 and 4.37, respectively. The variance profiles are very similar for the two simulations with differing BC treatment. This agrees with the close comparison between the average profiles and surface fluxes. The largest difference in the variance between the two BC occurs the last hour for all variables. The LSM predicts a higher variance as a result of

the higher sensible heat flux. The u and v variance from the simulations compare well with observations, although the magnitude is under predicted at most times and heights. This is partially due to the SGS variance that is not included in the simulations variance plots. The largest difference between observations and simulation resolved variance occurs shortly after the transition begins, at 0600 hours and 0700 hours. Comparison of the near surface potential temperature variance with the magnitude of the sensible heat flux indicates a positive correlation. However, the velocity variance is correlated with the positivity of the sensible heat flux.

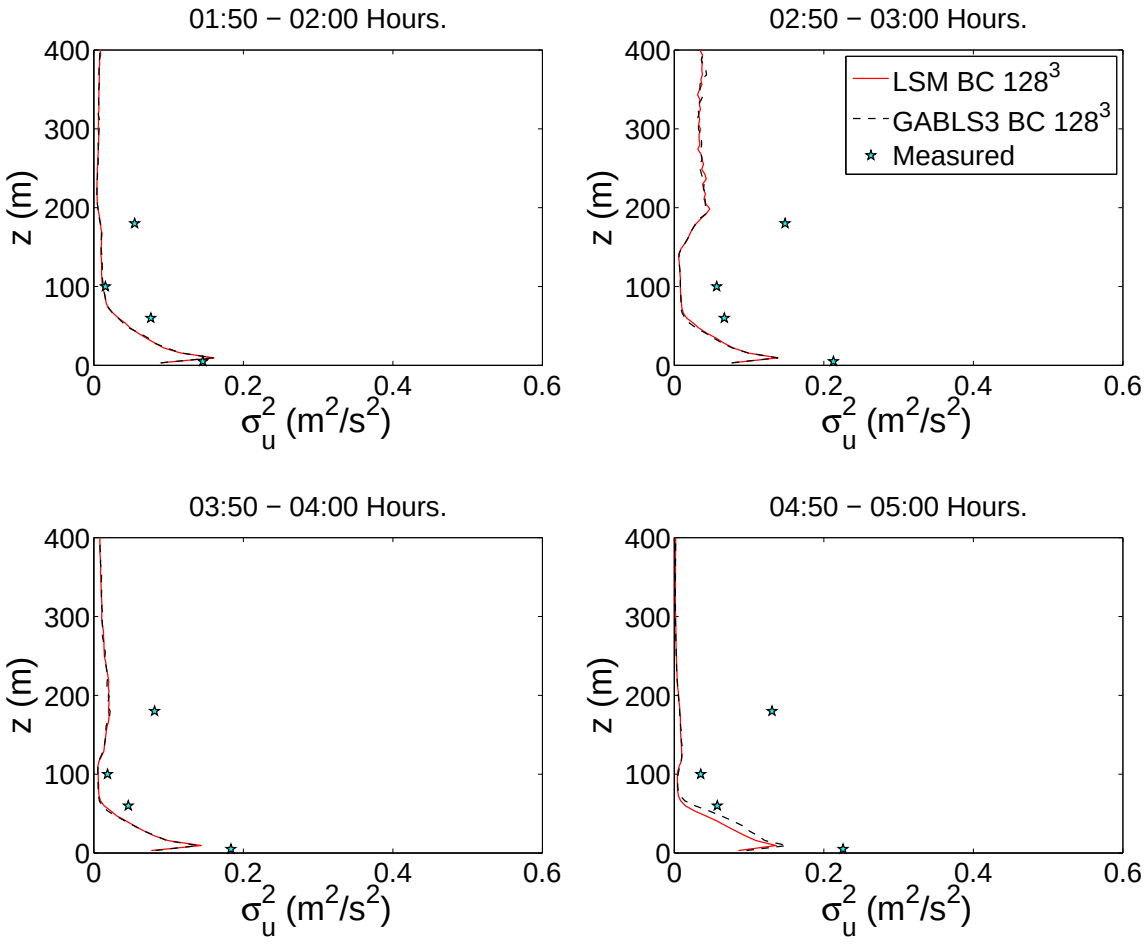

Figure 4.32. Profiles of $\sigma_{\tilde{u}}^2$ averaged over last 10 minutes of each hour from 0100-0500 hours, showing LSM-LES and GABLS3 LES results.

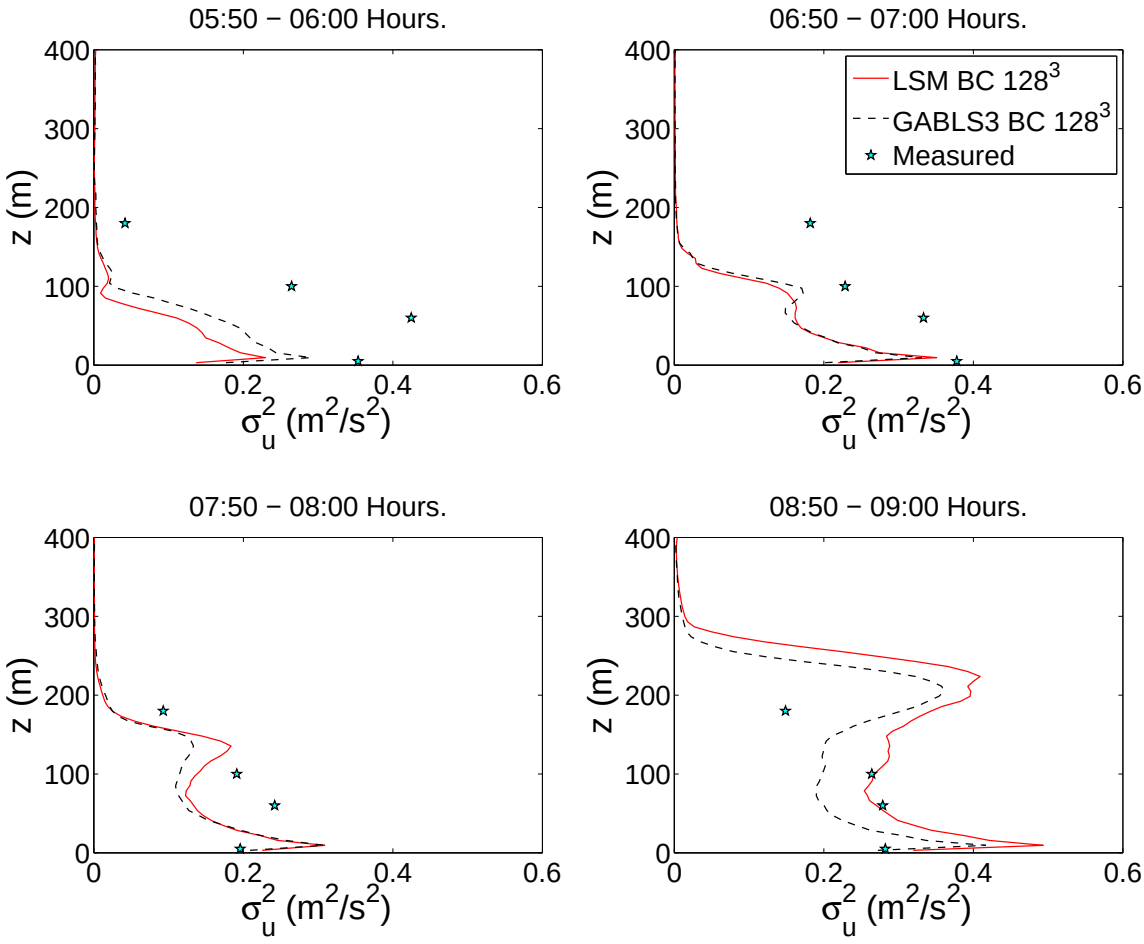

Figure 4.33. Profiles of $\sigma_{\tilde{u}}^2$ averaged over last 10 minutes of each hour from 0500-0900 hours, showing LSM-LES and GABLS3 LES results.

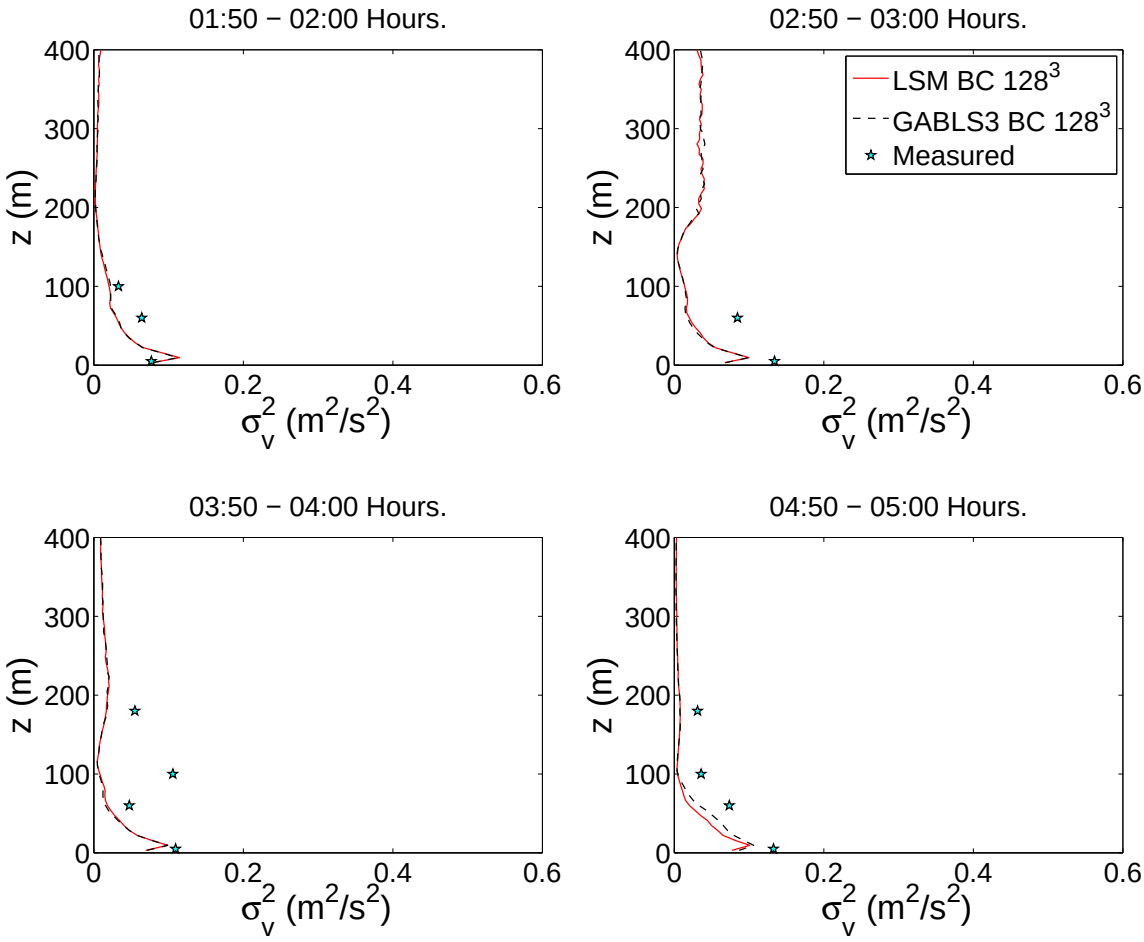

Figure 4.34. Profiles of $\sigma_{\tilde{v}}^2$ averaged over last 10 minutes of each hour from 0100-0500 hours, showing LSM-LES and GABLS3 LES results.

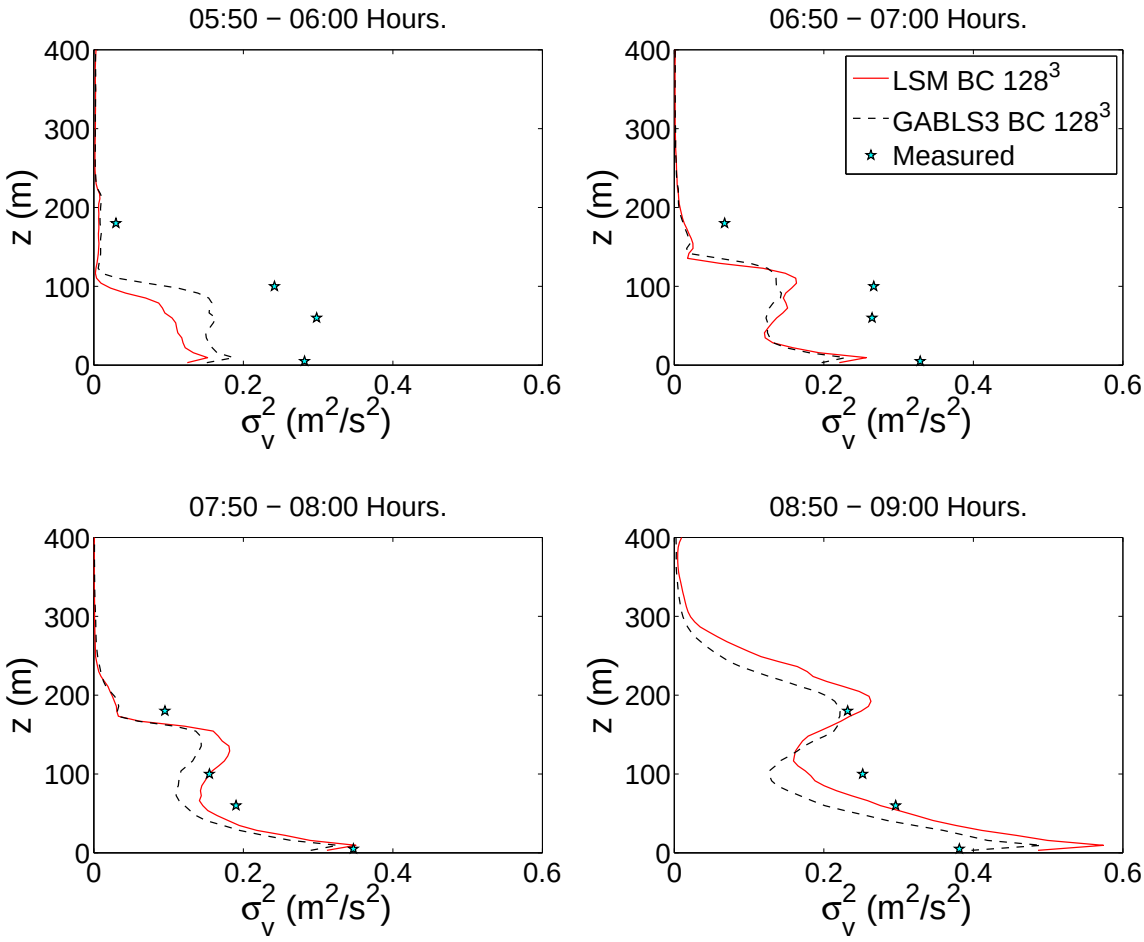

Figure 4.35. Profiles of $\sigma_{\tilde{v}}^2$ averaged over last 10 minutes of each hour from 0500-0900 hours, showing LSM-LES and GABLS3 LES results.

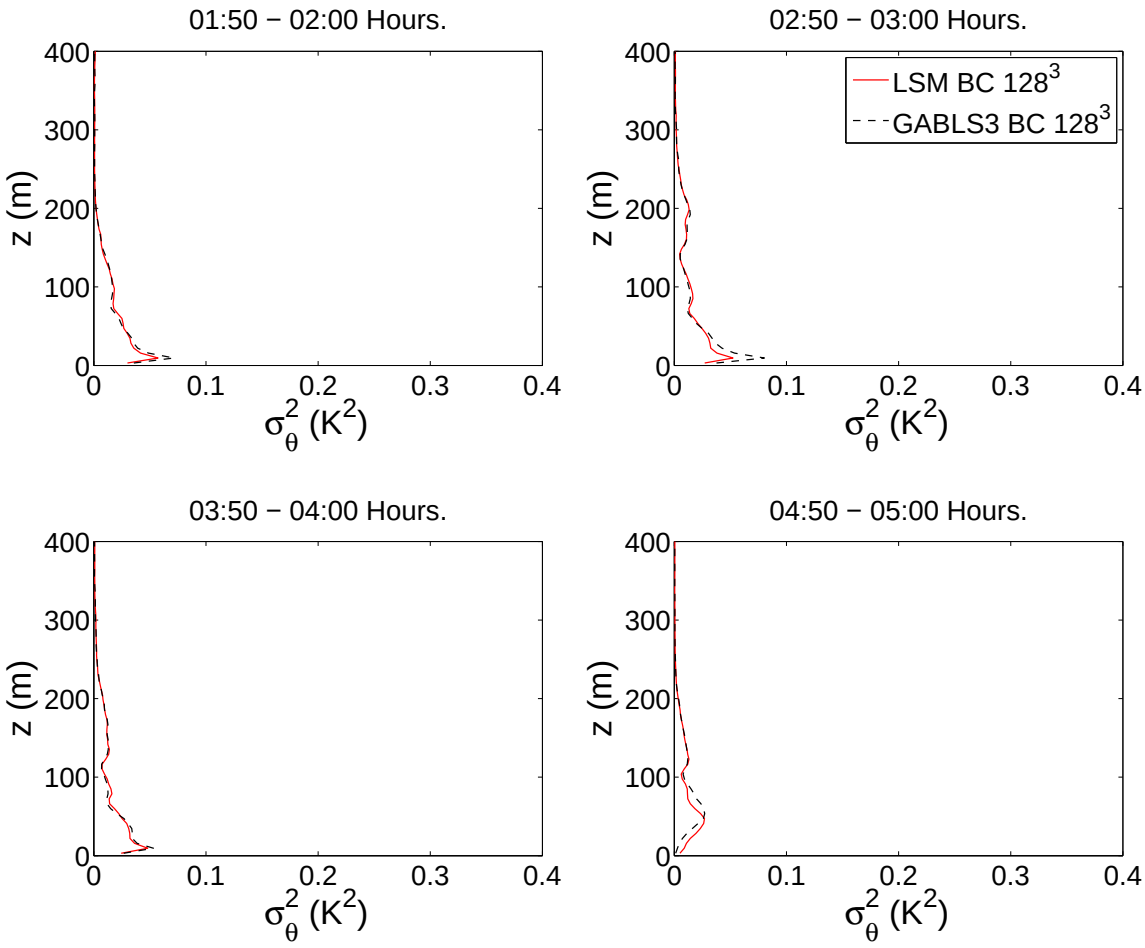

Figure 4.36. Profiles of $\sigma_{\tilde{\theta}}^2$ averaged over last 10 minutes of each hour from 0100-0500 hours, showing LSM-LES and GABLS3 LES results.

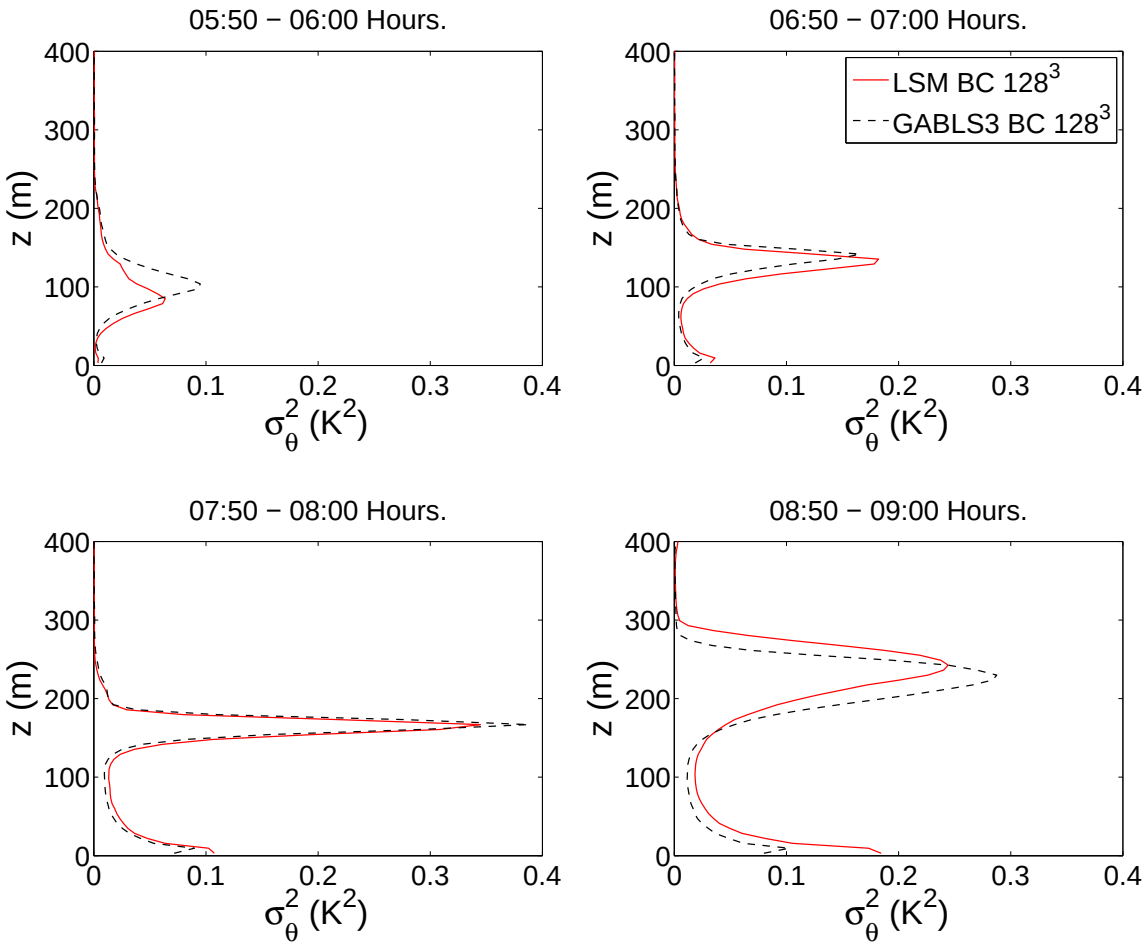

Figure 4.37. Profiles of $\sigma_{\tilde{\theta}}^2$ averaged over last 10 minutes of each hour from 0500-0900 hours, showing LSM-LES and GABLS3 LES results.

4.3.1 Spectral Characteristics

Insight into the ability of the SGS model to dissipate energy at the proper rate can be gained by analysis of the resolved velocity variance as a function of scale. Turbulent spectra can also show whether the LES realistically represents turbulence throughout the ABL. Figure 4.38 shows the horizontally averaged streamwise velocity spectra at 0300 and 0400 hours, respectively. Local scaling from Sorbjan [85] is used to nondimensionalize the spectra, where $\Phi_\epsilon = \kappa z \epsilon u_{*l}^{-3}$ is the normalized dissipation rate. This assumes that, locally, the dissipation rate ϵ is balanced by energy production from shear and destruction by buoyancy [69]. The spectrum for every odd vertical level below 100 m is depicted. As the height increases there is a decrease in spectral energy and the inertial sub-range shifts to larger nondimensional wavenumbers $k_1 z$. The spectra all collapse to a constant slope of approximately -5/3 for nondimensional wavenumbers $k_1 z > 1$. This agrees with Kolmogorov's theory for the dissipation rate of isotropic turbulence that occurs locally, at the small scales [50]. The spectrum from the first level decays too quickly and at small scales unrealistically drops below the energy of higher levels. The small scale energy at the first level depends on the surface BC as well as the SGS model. Generally, the log-linear surface BC is overly dissipative for momentum with the

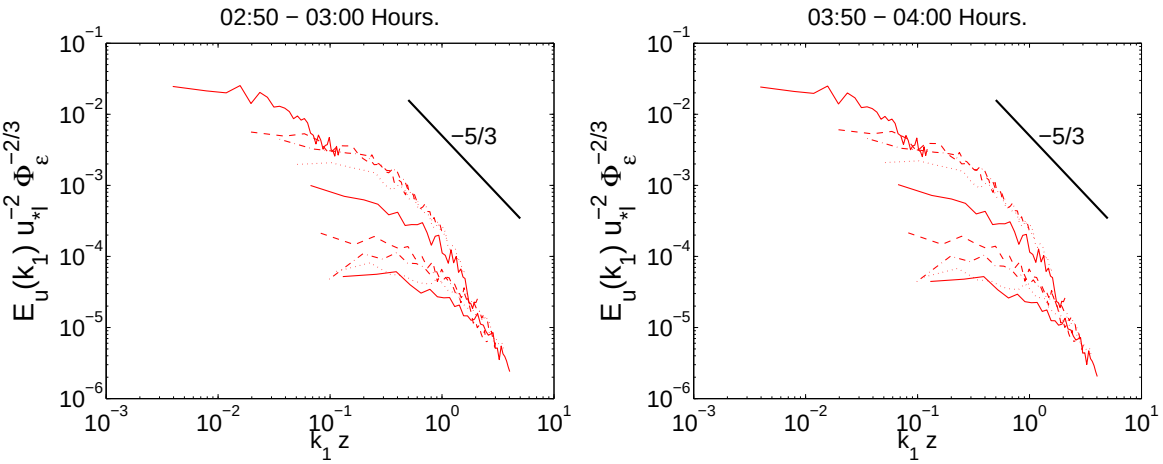

Figure 4.38. Normalized resolved $\tilde{u}$ velocity spectra at two stable time periods from the LSM-LES with the theoretical isotropic sub-range slope of -5/3.

degree of dissipation depending on the momentum roughness and the SGS model as discussed in detail by Stoll and Porté-Agel [87].

4.4 Resolution Dependence

This section compares important features of the LES as they depend on resolution, based on simulations at 128^3, 192^3 and 256^3 (equivalent to grid spacing of 6.25 m, 4.17 m, and 3.125 m) with the GABLS3 BC. The spatially averaged time series of the surface heat fluxes are shown in Figure 4.39. In general, each of the surface fluxes increases in magnitude with decreasing resolution. Although, there is an exception to this trend near the transition at 0500 hours. During the stable period the magnitude of the evaporation changes very little with resolution. The change in sensible heat flux shows more sensitivity to resolution than to the BC treatment as seen by comparing the stable period of Figure 4.39 with that of Figure 4.2. The same is true for the friction velocity shown in Figure 4.40. The change in magnitude of each of the surface fluxes follows the same trend showing there

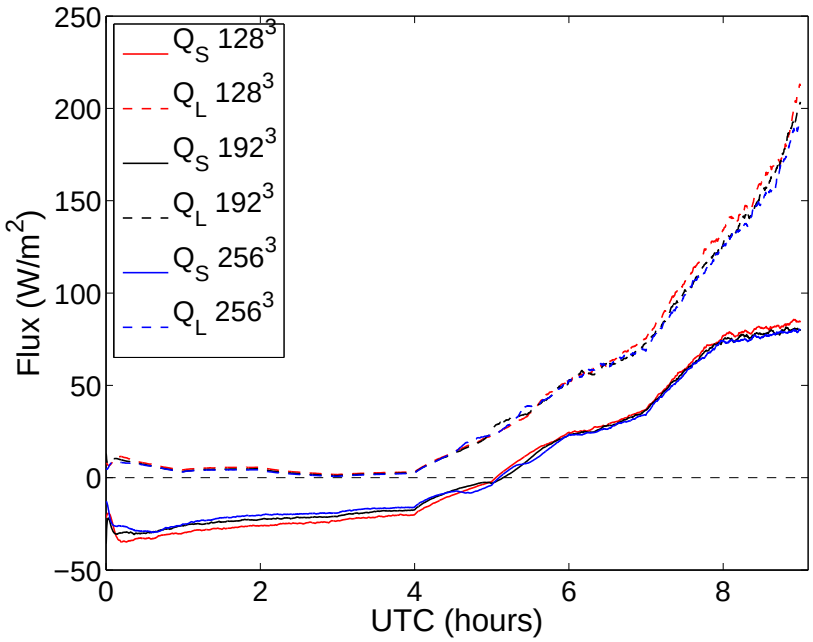

Figure 4.39. Sensible and latent heat flux (horizontally averaged) time series for resolutions of 128^3, 192^3, and 256^3.

functional relationship.

LES sensitivity to resolution is greatest when the SGS model accounts for more of the turbulent kinetic energy in the flow, for this reason features of the SBL at 0300 and 0400 hours are inspected. Table 4.1 contains the BL height (δ) and Obukhov length (L) at each time and for each resolution. The BL height shows very little resolution sensitivity, but does decrease slightly with increasing resolution. The Obukhov length shows no resolution sensitivity. Figure 4.41 depicts the average wind speed profiles, which show that the magnitude of the low-level jet increases with increasing resolution and the jet shifts downward. Profiles of potential temperature are shown for each resolution in Figure 4.42, indicating that the curvature of the temperature profile within the BL increases with resolution. LES results are effected by resolution through two modes, enhanced representation of gradients with increased resolution and inaccuracies due to the SGS model that becomes less significant with increasing resolution. Enhanced representation of gradients is implicit in LES methods, but significant effects from the SGS model is undesirable. The resolution effects observed in the mean profiles in conjunction with the BL height indicate that the results are mostly due to enhanced representation of gradients and the scale-dependent Lagrangian dynamic SGS model has little resolution sensitivity at the grid lengths considered.

Table 4.1. Boundary layer height, δ, and Obukhov length, L, at 0250-0300 and 0350-0400 hours for resolutions of 128^3, 192^3, and 256^3.

Grid size	0250-0300 UTC		0350-0400 UTC	
	δ (m)	L (m)	δ (m)	L (m)
128^3	128	21	105	27
192^3	118	21	94	27
256^3	108	21	89	28

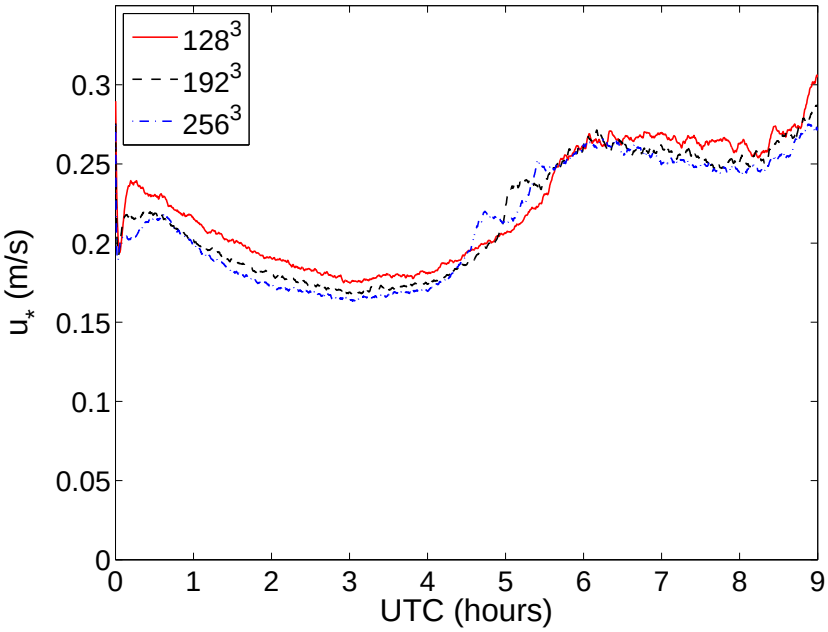

Figure 4.40. Friction velocity (horizontally averaged) time series for resolutions of 128^3, 192^3, and 256^3.

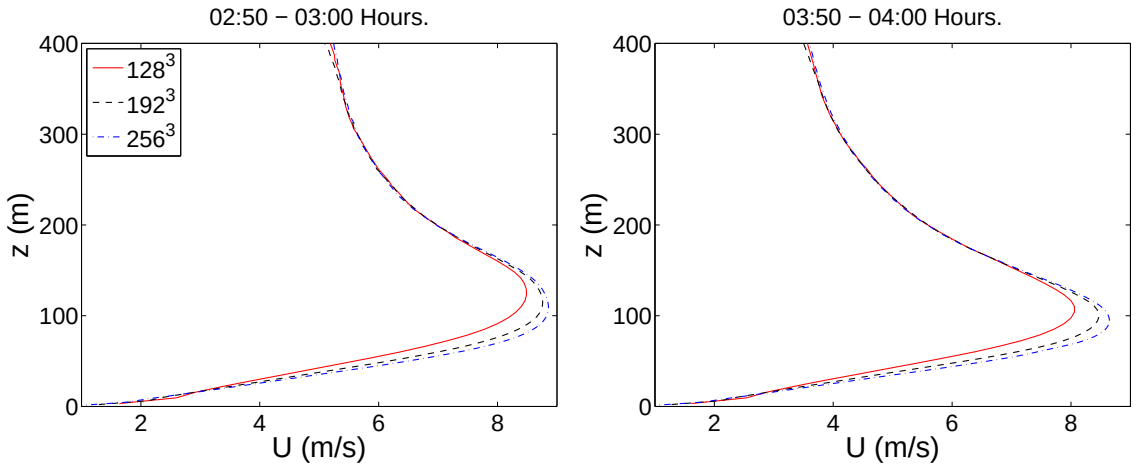

Figure 4.41. Wind speed profiles averaged over 10 minutes at two stable times for resolutions of 128^3, 192^3, and 256^3.

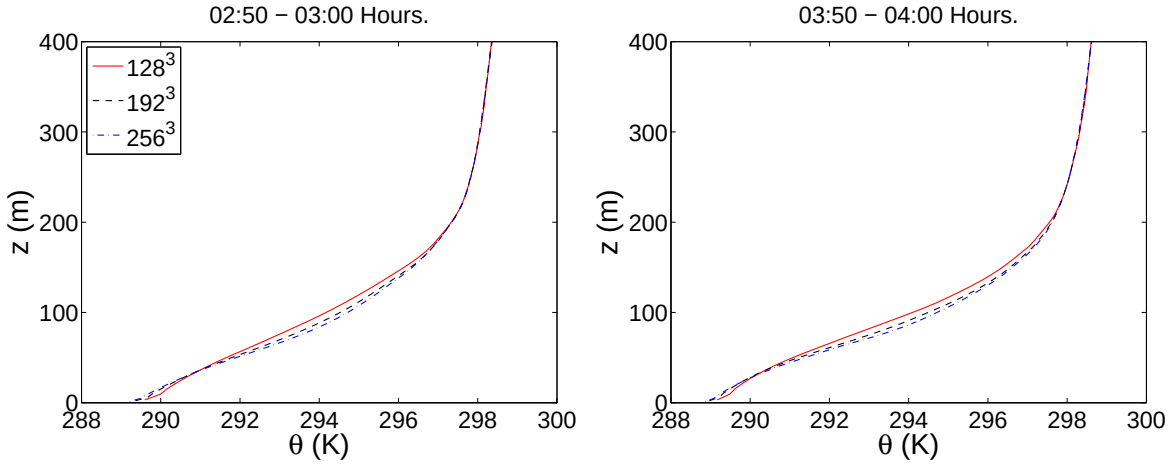

Figure 4.42. Potential temperature profiles averaged over 10 minutes at two stable times for resolutions of 128^3, 192^3, and 256^3.

CHAPTER 5

CONCLUSIONS

The purpose of this research was to implement a LSM within LES and test the coupled model on the diurnal SBL. This is the first time a coupled LSM-LES has been applied to the SBL and many interesting results have been observed. The LSM and GABLS3 BC both provide average surface turbulent heat fluxes that compare well with measurements for this LES case. This implies that both BCs are viable methods, each with different advantages. In general, the near surface state information required to drive GABLS3 type BCs are not available. Additionally, the GABLS3 method would not be possible for a heterogeneous surface since the state is based on measurements within the ABL. Alternatively, the LSM needs detailed soil type, temperature and moisture information that is also rarely available. Although soil measurements may not be available, the soil type can be approximated based on USDA soil type maps and the soil state can be approximated based on knowledge of the region (i.e. dry desert, irrigated crops, etc.) so that a reasonably accurate diurnal evolution can be achieved with the LSM. The LSM also provides two-way land-atmosphere coupling and predictions of surface states. Although the LSM provides accurate turbulent heat fluxes, the soil heat flux and the time rate of change in the soil temperature was over predicted by the LSM. This is largely attributed to the lack of a vegetation model that effectively adds an insulating layer above the soil.

An important result of this LES study is the temporal evolution of the ABL, which is strongly driven by the predicted surface fluxes. Many features of the ABL are correlated with the surface sensible heat flux including the boundary layer height, the stability and the turbulence intensity. During the night, negative sensible heat flux causes a moderately SBL that decreases in height and decreases

in turbulent kinetic energy as the simulation progresses. After sunrise the surface temperature begins to increase, causing the sensible heat flux to become positive. As the sensible heat flux increases a CBL develops and becomes increasingly unstable and more turbulent.

Mean profiles of velocity, potential temperature and specific humidity compare well to measurements and properly evolve during the stable period. However, the v velocity component develops an offset from observations during the morning transition. All first moment statistics are poorly predicted the last hour probably due to an incorrect large-scale advection term as indicated by Basu [6]. The SBL normalized spectra collapse to a constant -5/3 slope at small scales agreeing with Kolmogorov's theory for isotropic turbulence, which demonstrates the proper energy dissipation rate by the SGS model and realistic turbulence structure of the resolved fields. The simulations are able to produce important features of the ABL, including the nocturnal low-level jet. For the grid lengths tested, the simulations showed very little sensitivity to resolution. Overall, the LSM-LES coupled model produced good results in the SBL case considered.

5.1 Future Work

The LSM that has been implemented for this research produces fluxes that compare well to the GABLS3 LES case. To get a better understanding of how the LSM performs, more LES comparisons should be conducted with a variation of conditions between extremes. For instance, the GABLS3 case was moderately humid and the soil moisture content was mid-range between dry and saturated. The LSM should be tested in an environment that induces saturation and permanent wilting moisture content at the soil surface. Once the LSM proves to perform satisfactory under all conditions, it can be utilized to study the effect of different parameters and initial conditions on the results.

Although the use of the current LSM greatly improves the BC for LES, the model should be expanded to encompass more complex environments. The two additions that should be added first are a vegetation model and a longwave atmospheric radiation divergence model. As previously mentioned, the latter greatly

increases the computational expense and would not be desired for all simulations, but is important in capturing the evening transition development of a SBL. Radiation divergence may also be important in SBL regions with high temperature profile curvature and low turbulence [39].

The LSM in its current state can be used to study a variety of interesting phenomena. Heterogeneity of the surface can be studied by specifying the state of the soil and evolving the simulation in time. Within the SBL, heterogeneity has yet to be studied in this realistic manner.

APPENDIX

TYPICAL SURFACE PARAMETERS FOR NATURAL SURFACES

A.1 Radiative Properties

Table A.1. Representative values of shortwave albedo and longwave emissivity for a range of natural surface types (reproduced from Garratt [38] and [90]).

Surface Type	**Comments**	**Albedo**, α	**Emissivity**, ϵ
ocean	high sun	0.05	0.95
	low sun	0.1-0.5	0.95
desert		0.25	0.85
urban land	0.18	0.88	
forest	tropical	0.07-0.15	0.98
	coniferous	0.1-0.19	0.98
	deciduous	0.14-0.2	0.96
crops		0.15-0.25	0.96
grasses		0.15-0.30	0.96
soils	dark, wet	0.1	
	wet sandy	0.1-0.25	0.98
	wet clay	0.1-0.2	0.97
	dry sandy	0.2-0.4	0.9-0.95
	dry clay	0.2-0.35	0.95
snow	fresh	0.65-0.95	0.95
	old	0.45-0.65	0.9

APPENDIX

LES INPUTS

B.1 GABLS3 Boundary Conditions

Table B.1. GABLS3 lower boundary condition pressure, temperature and humidity time series at 0.25 m (reproduced from [7]).

Time (UTC)	**Pressure,** $P_{0.25}$ **(hPa)**	**Potential Temp. ,** $\Theta_{0.25}$ **(K)**	**Humidity,** $Q_{0.25}$ **(Kg/Kg)**
0	1022.1	291.28	0.0100
1	1022.0	290.34	0.0099
2	1022.0	289.45	0.0100
3	1021.8	288.62	0.0099
4	1021.9	288.43	0.0099
5	1022.1	289.95	0.0104
6	1022.3	292.38	0.0109
7	1022.3	294.16	0.0113
8	1022.3	296.55	0.0121
9	1022.2	298.45	0.0129

B.2 Initial Atmospheric Conditions (0000 hours UTC 2 July 2006)

Table B.2. Initial velocity profile (reproduced from [7]).

Z (m)	U $\left(\frac{m}{s}\right)$	V $\left(\frac{m}{s}\right)$
10	-3.35	0.04
20	-4.31	0.08
40	-6.13	0.32
80	-9.00	0.90
140	-11.48	3.50
200	-10.16	5.58
203	-10.08	5.57
257	-9.15	5.47
308	-8.75	5.54
363	-8.57	5.64
408	-8.46	5.64
426	-8.41	5.61
465	-8.23	5.47
520	-7.82	5.10
541	-7.60	4.90
575	-7.17	4.53
635	-6.22	3.76
657	-5.82	3.47
694	-5.14	3.00
715	-4.77	2.76
749	-4.19	2.46
772	-3.86	2.34
801	-3.54	2.31
830	-3.37	2.46

Table B.3. Initial pressure, potential temperature and specific humidity profiles (reproduced from [7]).

Time (UTC)	**Pressure, P (hPa)**	**Potential Temp. , Θ (K)**	**Humidity, Q (Kg/Kg)**
10	1020.91	292.72	0.0098
20	1019.73	293.02	0.0097
40	1017.37	293.41	0.0096
80	1012.67	294.30	0.0096
140	1005.67	295.68	0.0092
200	998.74	297.35	0.0089
203	998.50	297.35	0.0089
257	992.40	297.51	0.0089
308	986.60	297.66	0.0089
363	980.40	297.81	0.0089
408	975.40	297.94	0.0089
465	969.00	298.11	0.0089
520	962.80	298.27	0.0088
575	956.70	298.42	0.0088
635	950.20	298.60	0.0088
694	943.70	298.77	0.0088
749	937.80	298.93	0.0088
801	932.10	299.08	0.0088
854	926.40	299.23	0.0087

B.3 Geostrophic Forcing

Table B.4. Surface geostrophic wind (reproduced from [7]).

Time (UTC)	U_{geo} $\left(\frac{m}{s}\right)$	V_{geo} $\left(\frac{m}{s}\right)$
20060701 2300	-6.5	4.5
20060702 0300	-5.0	4.5
20060702 0600	-5.0	4.5
20060702 1200	-6.5	2.5

B.4 Large Scale Advection

Table B.5. Horizontal wind dynamic tendency (200-800 m) (reproduced from [7]).

Time (UTC)	U_{adv} $\left(\frac{m}{s^2}\right)$	V_{adv} $\left(\frac{m}{s^2}\right)$
20060701 2300	5.0×10^{-4}	0.0
20060702 0300	5.0×10^{-4}	0.0
20060702 0300	0.0	0.0
20060702 1200	0.0	0.0

Table B.6. Potential temperature dynamic tendency (200-800 m) (reproduced from [7]).

Time (UTC)	Θ_{adv} $\left(\frac{K}{s}\right)$
20060701 1200	-2.5×10^{-5}
20060702 0100	-2.5×10^{-5}
20060702 0100	7.5×10^{-5}
20060702 0600	7.5×10^{-5}
20060702 0600	0.0
20060702 1200	0.0

Table B.7. Specific humidity dynamic tendency (200-800 m) (reproduced from [7]).

Time (UTC)	Q_{adv} $\left(\frac{kg/kg}{s}\right)$
20060702 0000	0.0
20060702 0200	0.0
20060702 0200	-8.0×10^{-8}
20060702 0500	-8.0×10^{-8}
20060702 0500	0.0
20060702 1200	0.0

APPENDIX

LSM INPUTS

C.1 Initial Soil State

Table C.1. Initial soil temperature and moisture content profiles.

Depth (m)	**Temperature** (K)	**Moisture Content,** η $\left(\frac{m^3}{m^3}\right)$
0.0	292.2952	0.240
0.005	292.3062	0.247
0.01	292.3171	0.269
0.02	292.3390	0.274
0.04	292.9320	0.310
0.06	292.8385	0.330
0.08	292.7451	0.330
0.12	292.8211	0.360
0.20	292.0319	0.450
0.30	291.1353	0.470
0.50	289.2415	0.470
1.00	287.2110	0.570
2.00	283.1500	0.570

REFERENCES

[1] Albertson, J. D. *Large-eddy simulation of land-atmosphere interactions*. PhD dissertation, University of California, 1996.

[2] Albertson, J. D., and Parlange, M. B. Natural integration of scalar fluxes from complex terrain. *Adv. Water Resources 23* (1999), 239–252.

[3] Ancestry.com. http://freepages.genealogy.rootsweb.ancestry.com/ kidmiff/hoekstra.htm.

[4] Arya, S. P. *Introduction to Micrometeorology*, 2nd ed. Academic Press, California, 2001.

[5] Avissar, R., and Pielke, R. A. A parameterization of heterogeneous land surfaces for atmospheric numerical models and its impact on regional meteorology. *Mon. Wea. Rev. 117* (1989), 2113–2136.

[6] Basu, S. Personal communication.

[7] Basu, S. GABLS3 LES Intercomparison case description. Technical note, Texas Tech University, October 2008.

[8] Basu, S. Gewex atmospheric boundary layer study 3 (gabls3) LES intercomparison. http://www.atmo.ttu.edu/basu/GABLS3/index.html, June 2008.

[9] Basu, S., and Porté-Agel, F. Large-eddy simulation of stably stratified atmospheric boundary layer turbulence: a scale-dependent dynamic modeling approach. *Atm and Oceanic Physics* (2005), 1–17.

[10] Basu, S., Porté-Agel, F., Foufoula-Georgiou, E., Vinuesa, J., and Pahlow, M. Revisiting the local scaling hypothesis in stably stratified atmospheric boundary-layer turbulence: An integration of field and laboratory measurements with large-eddy simulations. *Bound Layer Met 119* (2005), 473–500.

[11] Basu, S., Vinuesa, J., and Swift, A. Dynamic les modeling of a diurnal cycle. *J of Applied Met and Clim 47* (2007), 1146–1174.

[12] Beare, R. J., Macvean, M. K., Holtslag, A. A. M., Cuxart, J., Esau, I., Golaz, J., Jimenez, M. A., Khairoutdinov, M., Kosovic, B., Lewellen, D., Lund, T. S., Lundquist, J. K., McCabe, A., Moene, A. F., Noh, Y., Raasch, S., and Sullivan, P. An intercomparison of large-eddy simulations of the stable boundary layer. *Bound Layer Meteor 118* (2006), 247–272.

[13] Beljaars, A. C. M., and Bosveld, F. C. Cabauw data for the validation of land surface parameterization schemes. *J. of Climate 10* (1997), 1172–1193.

[14] Beljaars, A. C. M., and Holtslag, A. A. M. Flux parameterization over land surfaces for atmospheric models. *Amer. Met. Soc. 30* (1991), 327–341.

[15] Betts, A. K., and Ball, J. H. Fife-1987 mean surface time series. *Atmospheric Research* (1992).

[16] Boers, R. Cabauw experimental site for atmospheric research: Access to infrastructure for accent-network of excellence. Tech. rep., July 2004.

[17] Boers, R., Bosveld, F., Knap, W., Baltink, H. K., Donovan, D., de Haan, S., Russchenberg, H., Apituley, A., ten Brink, H., Henzing, B., de Leeuw, G., Uijlenhoet, R., Arbesser-Rastburg, B., and Roeckmann, T. Cabauw experimental site for atmospheric research (cesar) - the netherlands: an initial gruan atmospheric profiling station. Technical note, CESAR, February 2009.

[18] Bosveld, F., de Bruijn, C., and Holtslag, B. Gewex atmospheric boundary layer study 3 (gabls3) SCM intercomparison. http://www.knmi.nl/samenw/gabls/index.html, June 2008.

[19] Bosveld, F., Vermeulen, A., Moors, E., Russchenberg, H., Apituley, A., Uijlenhoet, R., de Leeuw, G., Moene, A., and Werner, C. Atmospheric boundary layer observartions at cabauw the netherlands. Technical note, CESAR.

[20] Bosveld, F. C. Cabauw observational program on landsurface-atmosphere interaction (2000 - today). http://www.knmi.nl/ bosveld/, 2000.

[21] Bosveld, F. C., Kohsiek, W., Kroon, P., Moors, E., and Werner, C. Imbalances in the surface energy budget at the grassland site cabauw, the netherlands. poster, Royal Netherlands Meteorological Institute, September 2005.

[22] Bou-Zeid, E., Meneveau, C., and Parlange, M. Large-eddy simulation of neutral atmospheric boundary layer flow over heterogeneous surfaces: Blending height and effective surface roughness. *Water Res. Research 40* (2004), 1–18.

[23] Braun, F. J., and Schadler, G. Comparison of soil hydraulic parameterizations for mesoscale meteorological models. *J. of Applied Met 44* (2005), 1116–1132.

[24] Brown, A. R., Cederwall, R. T., Chlond, A., Duynkerke, P. G., Golaz, J. C., Khairoutdinov, M., Lewellen, D. C., Lock, A. P., Macvean, M. K., Moeng, C. H., Neggers, R. A. J., Siebesma, A. P., and Stevens, B. Large-eddy simulation of the diurnal cycle of shallow cumulus convection over land. *Quart. J. Roy. Meteor. Soc. 128* (2002), 1075–1093.

[25] Brutsaert, W. *Evaporation into the atmosphere.* Kluwer Academic Publisher, Dordrecht The Netherlands, 1982.

[26] Businger, J. A., and Arya, S. P. S. Height of the mixed layer in the stably stratified planetary boundary layer. *Adv. Geophysics 18A* (1974), 127–158.

[27] Businger, J. A., Wyngaard, J. C., Izumi, Y., and Bradley, E. F. Flux-profile relationships in the atmospheric surface layer. *J. Atm. Sci 28* (1971), 181–189.

[28] Chang, S., Hahn, D., Yang, C., and Norquist, D. Validation study of the caps model land surface scheme using the 1987 cabauw/PILPS data set. *J. of applied Met. 38* (1999), 405–422.

[29] Chapra, S. C., and Canale, R. P. *Numerical Methods for Engineers*, 4th ed. McGraw-Hill, New York, 2002.

[30] Chen, T. H., and et. al. Cabauw experimental results from the project for intercomparison of land-surface parameterization schemes. *J. of Climate 10* (1997), 1194–1215.

[31] Chou, M. Broadband water vapor transmission functions for atmospheric IR flux computations. *J. of Atm Sci 41* (1984), 1775–1778.

[32] Clapp, R. B., and Hornberger, G. Empirical equations for some soil hydraulic properties. *Water Resources Res. 14* (1978), 601–604.

[33] Clarke, R. H., Dyer, A. J., Brook, R. R., Reid, D. G., and Troup, A. J. The wangara experiment: Boundary layer data. Tech. rep., 1971.

[34] Collins, W. D., Rasch, P. J., Boville, B. A., Hack, J. J., McCaa, J. R., Williamson, D. L., Kiehl, J. T., Briegleb, B., Bitz, C., Lin, S.-J., Zhang, M., and Dai, Y. Description of the NCAR Community Atmosphere Model (CAM 3.0). Technical note, NCAR, 2004.

[35] Deardorff, J. W. Efficient prediction of ground surface temperature and moisture with inclusion of a layer of vegetation. *J. Geophys. Res. 83* (1978), 1889–1903.

[36] Duynkerke, P. G., de Roode, S. R., van Zanten, M. C., Calvo, J., Cuxart, J., Cheinet, S., Chlond, A., Grenier, H., Jonker, P. J., Kohler, M., Lenderink, G., Lewellen, D., Lappen, C., Lock, A. P., Moeng, C., Muller, F., Olmeda, D., Piriou, J., Sanchez, E., and Sednev, I. Observations and numerical simulations of the diurnal cycle of the EUROCS stratocumulus case. *Quart. J. Roy. Meteor. Soc. 130* (2004), 3269–3296.

[37] Friedl, M. A. Modeling land surface fluxes using a sparse canopy model and radiometric surface temperature measurements. *J of Geophys. Res. 100* (1995), 25435–25446.

[38] Garratt, J. R. *The atmospheric boundary layer.* Cambridge University Press, New York, 1992.

[39] Garratt, J. R., and Brost, R. A. Radiative cooling effects within and above the nocturnal boundary layer. *J. of Atm. Sci. 38* (1981), 2730–2746.

[40] Garrett, A. J. *Numerical simulations of atmospheric convection over the southeastern U.S. in undisturbed conditions.* PhD thesis, Texas Univ., Austin., May 1978.

[41] Garrett, A. J. A parameter study of interactions between convective clouds, the convective boundary-layer, and forested surface. *Mon. Wea. Rev. 110* (1982), 1041–1059.

[42] Germano, M., Piomelli, U., Moin, P., and Cabot, W. H. A dynamic sub-grid-scale eddy viscosity model. *Phys. Fluids 3* (1991), 1760–1765.

[43] Holtslag, A. A. M., and Nieuwstadt, F. T. M. Scaling the atmospheric boundary layer. *BLM 36* (1986), 201–209.

[44] Huang, H., and Margulis, S. A. Evaluation of a fully coupled les-lsm model and its diagnosis of land-atmosphere feedback. *Water Res Research* (2009).

[45] Idso, S., Jackson, R., Kimball, B., and Nakayama, R. The dependence of bare soil albedo on soil water content. *J. Appl. Meteorol. 14* (1975), 109–113.

[46] Jackson, T. J. Southern great plains 1997 (sgp97) hydrology experiment plan. Tech. rep., 1997.

[47] Jacquemin, B., and Noilhan, J. Sensitivity study and validation of a land surface parameterization using the HAPEX-MOBILHY data set. *BLM 52* (1990), 93–134.

[48] Kanda, M., Inagaki, A., Letzel, M., Raasch, S., and Watanabe, T. Les study of the energy imbalance problem with eddy covariance fluxes. *BLM 110* (2004), 381–404.

[49] Kleissl, J., Kumar, V., Meneveau, C., and Parlange, M. B. Numerical study of dynamic smagorinsky models in large-eddy simulation of the atmospheric boundary layer: Validation in stable and unstable conditions. *Water Res Research 42* (2006), 1–12.

[50] Kolvogorov, A. N. The local structure of turbulence in incompressible viscous fluid for very large reynolds number. *Dokl. Adad. Nauk S.S.S.R. 30* (1941), 299–303.

[51] Kosovic, B., and Curry, J. A large-eddy simulation study of a quasi-steady, stably stratified atmospheric boundary layer. *J of Atm Sci 57* (2000), 1052–1068.

[52] Kraus, H., Malcher, J., and Schaller, E. Noctunal low-level jet during PUKK. *Bound. Layer Meteor. 31* (1985), 1–20.

[53] Kumar, V., Kleissl, J., Meneveau, C., and Parlange, M. B. Large-eddy simulation of a diurnal cycle in the turbulent atmospheric boundary layer: Atmospheric stability and scaling issues. *Water Res Research 42* (2006).

[54] Kustas, W. P., Hatfield, J. L., and Prueger, J. H. The soil moisture-atmosphere coupling experiment (smacex): Background, hydrometeorological conditions, and preliminary findings. *J. Hydrometeorol. 6* (2005), 791–804.

[55] Lettau, H. H., and Davidson, B. *Exploring the atmosphere's first mile*, vol i ed. Pergamon Press, 1957.

[56] Lilly, D. K. The representation of small scale turbulence in numerical simulation experiments. *Proc. IBM Sci. Computing Symp. on Env. Sci IBM Form No. 320-1951* (1967), 195–209.

[57] Lin, C., and Glendening, J. W. Large-eddy simulation of an inhomogeneous atmospheric boundary layer under neutral conditions. *J. of Atm. Sci. 59* (2002), 2479–2497.

[58] Mahrer, Y., and Pielke, R. A. The effects of topography on sea and land breezes in a two-dimensional numerical model. *Mon. Wea. Rev. 105* (1977), 1151–1162.

[59] Mahrer, Y., and Pielke, R. A. A numerical study of the airflow over irregular terrain. *Conrib. Atmos. Phys. 50* (1977), 98–113.

[60] Mahrt, L., and Pan, H. L. A two-layer model of soil hydrology. *Bound. Layer Meteor. 29* (1984), 1–20.

[61] Mason, P. J., and Callen, N. S. On the magnitude of the sub-grid scale eddy coefficient in large-eddy simulations of turbulent channel flow. *J. Fluid Mech 162* (1986), 439–462.

[62] McCumber, M. C. *A numerical simulation of the influence of heat and moisture fluxes upon mesoscale circulations.* PhD dissertation, University of Virginia, University Microfilms International, P.O. Box 1346, Ann Arbor, MI 48106-1346, 1980.

[63] McCumber, M. C., and Pielke, R. A. Simulation of the effects of surface fluxes of heat and moisture in a mesoscale numerical model. *J. Geophys. Res. 86* (1981), 9929–9938.

[64] Milly, P. C. D. Potential evaporation and soil moisture in general circulation models. *J of Climate 5* (1991), 209–226.

[65] Mlawer, E. J., Taubman, S. J., Brown, P. D., and Iacono, M. J. Radiative transfer for inhomogeneous atmospheres: Rrtm, a validated correlated-k model for the longwave. *J. Geophys. Res. 102* (1997), 16663–16682.

[66] Moeng, C. A large-eddy simulation model for the study of planetary boundary layer turbulence. *J. of Atm. Sci. 41* (1984), 2052–2062.

[67] Moore, G. E. Cramming more components onto integrated circuits. *Electronica 38* (1965).

[68] Nakshabandi, J. A., and Kohnke, H. Thermal conductivity and diffusivity of soils as related to moisture tension and other physical properties. *Agric. Meteorol. 2* (1965), 271–279.

[69] Nieuwstadt, F. T. M. A model for the stationary, stable boundary layer. In *Proceedings of IMA conference turbulence and diffusion in stable environments.* (1984), Cambridge, Ed., pp. 271–279.

[70] Noilhan, J., and Planton, S. A simple parameterization of land-surface processes for meteorological models. *Monthly Wea Rev 117* (1988), 536–549.

[71] Patton, E. G., Sullivan, P. P., and Moeng, C. The influence of idealized heterogeneity on wet and dry planetary boundary layers coupled to the land surface. *J Atmos Sci 62* (2005), 2078–2097.

[72] Philip, J. R., and de Vries, D. A. Moisture movement in porous materials under temperature gradients. *Trans. Amer. Geophys. Union 38* (1957), 222–232.

[73] Pielke, R. A. *Mesoscale Meteorological Modeling*, 2nd ed. Academic Press, California, 2002.

[74] Pope, S. B. *Turbulent Flows*. Cambridge University Press, Cambridge, 2001.

[75] Porté-Agel, F. A scale-dependent dynamic model for scalar transport in large-eddy simulations of the atmospheric boundary layer. *Boundary Layer Met 112* (2004), 81–105.

[76] Richards, L. A. Capillary conduction of liquids through porous mediums. *Physics 1* (1931), 318–333.

[77] Russchenberg, H., Bosveld, F., Swart, D., ten Brink, H., Herben, M., de Leeuw, G., Stricker, H., Arbesser-Rastburg, B., and van der Marel, H. Cesar: Cabauw experimental site for atmospheric research. Technical note, CESAR.

[78] Sagaut, P. *Large eddy simulation for incompressible flows*, 2nd ed. Springer, Berlin, 2002.

[79] Saiki, E., Moeng, C., and Sullivan, P. Large-eddy simulation of the stably stratified planetary boundary layer. *Bound Layer Met 95* (2000), 1–30.

[80] Sellers, P. J., Mintz, Y., Sud, Y., and Dalcher, A. A simple biosphere model (sib) for use within general circulation models. *J. of Atm. Sci. 43* (1996), 505–531.

[81] Skyllingstad, E. D., Samelson, M. R., Mahrt, L., and Barbour, P. A numerical modeling study of warm offshore flow over cool water. *Mon Wea Rev 133* (2005), 345–361.

[82] Skyllingstad, E. D., Vickers, D., Mahrt, L., and Samelson, R. Effects of mesoscale sea-surface temperature fronts on the marine atmospheric boundary layer. *Bound Layer Meteor 123* (2007), 219–237.

[83] Smagorinsky, J. General circulation experiments with the primitive equations, part 1: the basic experiment. *Mon Wea Rev 91* (1963), 99–164.

[84] Smirnova, T. G., Brown, J. M., and Benjamin, S. G. Performance of different soil model configurations in simulating ground surface temperature and surface fluxes. *Mon Wea Rev 125* (1997), 1870–1884.

[85] Sorbjan, Z. Local similarity of spectral and cospectral characteristics in the stable-continuous boundary layer. *Bound. Layer Meteor. 35* (1986), 257–275.

[86] Stoll, R., and Porté-Agel, F. Dynamic subgrid-scale models for momentum and scalar fluxes in large-eddy simulations of neutrally stratified atmospheric boundary layers over heterogeneous terrain. *Water Resources Res. 42* (2006), W01409.

[87] Stoll, R., and Porté-Agel, F. Effect of roughness on surface boundary conditions for large-eddy simulation. *Bound. Layer Meteor. 118* (2006), 169–187.

[88] Stoll, R., and Porté-Agel, F. Large-eddy simulation of the stable atmospheric boundary layer using dynamic models with different averaging schemes. *Bound. Layer Meteor. 126* (2008), 1–28.

[89] Stoll, R., and Porté-Agel, F. Surface heterogeneity effects on regional-scale fluxes in stable boundary layers: surface temperature transitions. *J. Atmos. Sci.* (2008).

[90] Stull, R. B. *An introduction to boundary layer meteorology.* Kluwer Academic Publishers, The Netherlands, 1988.

[91] Sun, J., Burns, S., Delany, A., Horst, T., Oncley, S., and Lenschow, D. Heat balance in nocturnal boundary layer during cases-99. *J. Appl. Meteorol. 42* (2003), 1649–1666.

[92] Tjemkes, S., and Duynkerke, P. The nocturnal boundary layer: Model calculations compared with observation. *J Appl Meteorol 28* (1989), 161–175.

[93] University Corporation for Atmospheric Research (UCAR). Cabauw reference site. http://www.eol.ucar.edu/projects/ceop/dm/insitu/sites/baltex/cabauw/cabauw/.

[94] Voller, V. R., and Porté-Agel, F. Moore's law and numerical modeling. *Journal of Computational Physics 179* (2002), 698–703.

[95] Wikipedia.com. http://en.wikipedia.org/wiki/Netherlands.